Polarization transfer in ion-surface scattering

OMSLAG: *Photograph of a water reflection. All reflections from objects above water are partially polarized.*

This work is sponsored by the 'Stichting voor Fundamenteel Onderzoek der Materie' (FOM) which is financially supported by the 'Nederlandse organisatie voor Wetenschappelijk Onderzoek' (NWO).

DRUK: *Drukkerij Van Denderen, Groningen, april 2004.*

RIJKSUNIVERSITEIT GRONINGEN

Polarization transfer in ion-surface scattering

Proefschrift

ter verkrijging van het doctoraat in de
Wiskunde en Natuurwetenschappen
aan de Rijksuniversiteit Groningen
op gezag van de
Rector Magnificus, dr. F. Zwarts,
in het openbaar te verdedigen op
vrijdag 7 mei 2004 om
16.15 uur

door

Danyal Ferdinant Alexander Winters

geboren op 25 maart 1973
te Meppel

Promotores:	Prof. dr. R. Morgenstern
	Prof. dr. ir. R. Hoekstra
Beoordelingscommissie:	Prof. dr. W. Heiland
	Prof. dr. R.G.E. Timmermans
	Prof. dr. L. Niesen

Contents

Chapter 1

General introduction

1.1 Introduction

When ions are scattered off surfaces at small incidence angles and at low energies of typically several hundred eV or a few keV, they interact exclusively with the uppermost surface layer. If one understands these dynamic interaction processes, one can gain detailed information on the surface properties. In general, ion-surface collisions are known to be sensitive to the geometrical and electronic properties of the surface structure. In particular, electron capture processes are expected to be sensitive to the spin ordering of the surface electrons. Electron capture processes should therefore result in polarized electronic states of the scattered projectiles. An analysis of these states would then provide valuable information on the surface electronic structure and even on the magnetic ordering. From a fundamental point of view, the magnetic properties of the surface are of interest since they often differ from those of the bulk, see *e.g.* Refs. [1] to [4]. With decreasing dimensions of electronic structures in devices, the relative importance of (magnetic) surfaces is also increasing from a practical point of view. For example, magnetic structures in recording media have already reached the sub-micron regime and there surface properties become of increasing relevance.

The general mechanisms of electron transfer during collisions of highly charged ions on surfaces have been clarified earlier, see *e.g.* Refs. [5] to [10]. In order to understand how ion-surface collisions can be exploited to gain information on surface magnetism, knowledge of these mechanisms is crucial. Therefore first a brief overview of the formation and decay of multiply excited atoms, resulting from the interaction of highly charged ions with a surface is given.

1.2 Ion-surface interaction

Far above the surface, when the projectile is still in its ionic state, image charge effects occur and the Highly Charged Ion (HCI) is accelerated towards the surface, see *e.g.* [11]. Somewhat closer to the surface, charge transfer of electrons between energetically resonant target and projectile states takes place. This charge transfer generally occurs when the potential barrier between ion and surface is lowered to the Fermi level of the target. In this classical picture, charge transfer proceeds predominantly over-the-barrier into excited projectile states and a so-called 'hollow atom' is formed, see *e.g.* [12]. The energy stored in these highly population-inverted projectiles is released via radiative decay and Auger transitions, see *e.g.* [13, 14]. Especially for slow projectiles incident at small angles, the formation and decay of the excited states takes place above the surface.

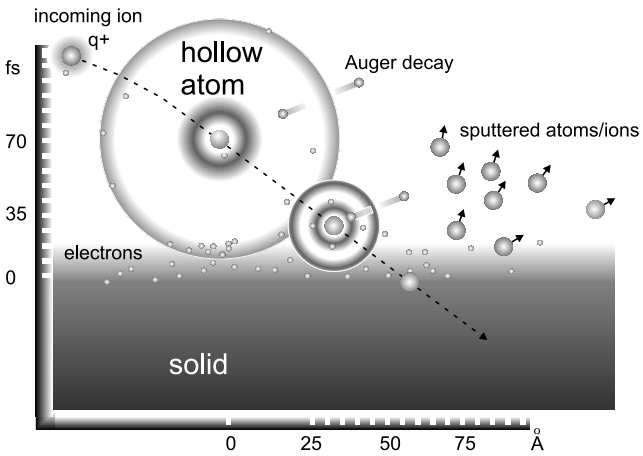

Figure 1.1: Artistic view of the neutralization of a HCI approaching a surface, and the formation and decay of the 'hollow atom' by Auger electron emission.

Multiply excited states, resulting from neutralization of light projectiles, predominantly decay via KLL Auger transitions. In such a two-electron process, one of the L-shell electrons fills the initial K-shell vacancy while the other one (the Auger electron) is emitted into the vacuum. Generally, radiative decay rates become more pronounced with increasing projectile mass. On the other hand, states comprising only one (captured) excited electron (singly excited states) rather decay via radiative transitions. This process only requires an initial K-shell vacancy.

Depending on the scattering conditions, the projectile is either reflected

from the surface or penetrates into it, thereby (possibly) sputtering particles from the surface. Figure 1.1 shows an artistic view of a HCI approaching a solid state surface.

In order to probe (changes in) the surface electronic structure, like *e.g.* spin ordering effects of only the topmost surface layer, extremely surface sensitive methods are required. Furthermore, due to the small dimensions of *e.g.* magnetic domains, these methods should be able to distinguish between long- and short-range magnetic ordering of surface electron spins. In this thesis, results obtained with two such techniques are presented.

Electron Capture Spectroscopy (ECS)

This method exploits the fact that the electron spin is conserved during the electron capture process. The electron spin then couples to the orbital angular and/or nuclear spin momentum. By using fast (150 keV) D^+ beams, Rau *et al.* [15, 16] exploited the hyperfine interaction to investigate surface magnetism. A problem with the use of such fast beams is that extremely small angles of incidence are necessary, rendering the method very sensitive to surface imperfections. Also the detection method, which is based on the angular distribution of alpha particles produced in collisions of the deuterons on tritium, is rather complex.

Instead, when slow ($\sim$ 10 keV) ion beams at small incidence angles are used, neutralization partly takes place into excited projectile states which decay via photon emission. Via spin-orbit coupling the spin polarization is partly transferred into the M_L components of the orbital angular momentum L, which in turn is reflected in the polarization of fluorescence photons. Therefore photons emitted subsequently in the decay of the projectiles will reflect the magnetic surface properties. Using low energy singly charged ions, this method has been shown to be sensitive to the topmost surface layer [17, 18]. The circular polarization of the fluorescence light has already been exploited to probe surface magnetism, see *e.g.* [19, 20, 21]. Information on the analysis of the polarization of the emitted light can be found in chapter 3. The transfer of the polarization of surface electrons into spin-polarized projectile states is discussed in chapter 5, where our experimental results are presented.

Auger Electron Spectroscopy (AES)

This method is based on the capture of surface electrons into discrete and distinguishable excited projectile states. The energy of the subsequently emitted Auger electrons is characteristic for the initial state. Spectroscopy of the Auger electrons emitted from the excited projectiles might thus provide information on the population of the initial states, which in turn reflects the spin polarization of the surface electrons. For a non-magnetic target, the electron

spins are randomly directed. Therefore on average low-spin states (singlet) will be populated. If the surface is magnetized, most of the spins are aligned and higher spin states (triplet) will be populated. The ratio of Auger electron emission from low- and high-spin states within the projectile can therefore be expected to be sensitive to surface magnetism. Without resolving the different spin states, Pfandzelter *et al.* [22] showed, by using a SPLEED detector [23] for polarization analysis, that the KLL Auger electrons emitted from the excited projectiles are indeed polarized.

Realizing that the neutralization starts far in front of the surface, the projectile can be used to detect the short-range magnetic ordering of the surface. Because if the ions are incident normal to the surface, the electrons are extracted from an area of a few $Å^2$. On the other hand, if they are grazingly incident they extract electrons from an area of several tens of $Å^2$.

So by measuring electron spectra for different incidence angles, hollow atoms might be a unique tool to sample the short-range ordering of the topmost atomic layer of the surface. In addition to the possibility of probing local magnetic ordering, advantages of AES are the relatively high efficiency (almost all particles decay via autoionization) and the fact that measurements can be taken at all temperatures (the black-body radiation at high target temperatures does not interfere as is the case with ECS).

The main advantage of slow (highly charged) ions, as compared to the other methods, is their extreme surface sensitivity. Ion beams incident on the surface at suitable energies and angles do not penetrate into the target and interact only with the upper surface layer [24, 25, 26]. Due to the absence of hard collisions between projectile and target atoms, and the corresponding energy deposition into the surface, the interaction is predominantly of electronic nature (Coulomb force). In modern ion sources (see chapter 3) high charge states can be reached, which allows for a tuning of the electronic interaction.

1.3 Alternative techniques

In the past various other methods have been used to investigate surface electronic structures, and in particular surface magnetism. The most important ones are briefly discussed below, including their advantages and their disadvantages. For clarity, a distinction is made between methods based on photons and electrons.

Photons

An often used technique is the Magneto-Optical Kerr Effect (MOKE), which makes use of the rotation of polarization when light is reflected from a magnetized surface [27]. Since typical wavelengths of the light are large as compared

to the thickness of a monolayer, the depth resolution of this method is rather low and it is difficult to separate the influence of the surface from that of the bulk. The sensitivity can be drastically enhanced by using the non-linear Kerr effect, i.e. by measuring the polarization rotation in the second harmonic of pulsed laser light [28]. Second harmonic generation occurs only at the surface where the inversion symmetry of center-symmetric crystal structures is broken. Also the variation of light absorption or reflection can be used when linearly or circularly polarized light is shined on a magnetized surface and the sample magnetization is reversed. Magnetic Circular Dichroism (MCD) exploits light induced transitions from core levels to magnetic valence states just above the Fermi level near the absorption edge [29]. In X-ray Resonant Magnetic Scattering (XRMS) the magnetization dependent reflection or diffraction of synchrotron light is exploited [30, 31]. A strength of these methods is their element selectivity. Spatial resolution of magnetic structures can be obtained when MCD is used in Photo-Emission Electron Microscopy (PEEM) [32, 33]. In this case impressive direct images of element selective magnetic structures with μ-meter resolution are obtained. However the surface sensitivity of all these methods is limited by the penetration depth of the light. Although the surface sensitivity can be improved by using light at grazing angles of incidence [30, 31], it is practically impossible to limit the probing depth to just one atomic layer.

Electrons

Similarly, electron based microscopy techniques have a limited surface sensitivity related to the penetration- and escape depth of the electrons. This is for example true for Scanning Electron Microscopy with Polarization Analysis (SEMPA), which measures the spin polarization of secondary electrons from a magnetized target [34]. Surface sensitivity in combination with excellent spatial resolution is achieved by Scanning Tunneling Microscopy (STM). However, it is difficult to obtain spin contrast in STM on a routine basis. As pointed out by Himpsel *et al.* [1], this might be caused by the localized nature of the spin-polarized d- and f-electrons which prevents overlap between the magnetic states on tip and sample, such that the tunnel current is mainly carried by the de-localized s- and p-electrons. Smaller tip-surface distances should then result in a higher spin-polarized transfer through $3d$-states.

1.4 This thesis

In chapter 2 the relevant ion-surface fundamentals are discussed, so as to provide a conceptual basis for the results presented in this work. The most important neutralization and deexcitation mechanisms are treated, without going

into too much (theoretical) detail.

Chapter 3 deals with the experiment, *i.e.* the ion source and the experimental setup are described. The experiments in chapter 4 and section 5.2 were performed with the $Sir\phi$ setup, which is described elsewhere [35, 36]. The experiments in section 5.3, 5.4 and chapter 6 were obtained with the completely upgraded version $Sir\phi^{++}$.

In chapter 4, results are presented from collisions of different highly charged ions with a carbon surface (HOPG). A surprisingly high yield of emitted target Auger electrons was observed, which is attributed to KLL Auger decay from (sputtered) hollow carbon atoms from the surface of the target.

Chapter 5 contains our latest results on spin-polarized surfaces. Both spectroscopic methods (ECS and AES) are applied to study differently prepared spin-polarized surfaces. Firstly, AES is used to probe a GaAs surface, spin-polarized by optical pumping. Secondly, AES was applied to a ferromagnetic Ni target to study changes in the spin ordering at the surface, induced by heating the sample below and above the Curie temperature. Thirdly, ECS was applied to probe magnetically induced changes in the surface spin ordering of the Ni target.

In chapter 6 we present a relatively simple model, which can describe the deexcitation of doubly excited helium projectiles above different surfaces. The model results are discussed and compared to experimental data obtained for various surfaces and scattering conditions. Also an attempt is made to correlate the observed changes in the Auger spectra to the spin polarization of the magnetic target.

Finally in chapter 7, the main conclusions of the research presented in this thesis are summarized and an outlook is given.

Chapter 2

Ion-surface fundamentals

2.1 Introduction

The main purpose of this chapter is to give an overview of the ion-surface processes of relevance for the experiments presented in this thesis. The reason for this approach is that the ion-surface interaction is a very complex, dynamical many-body problem. This is in particular true for Multiply Charged Ions (MCI's) impinging on surfaces. A rigorous theoretical description of the ion-surface interaction is beyond the scope of this thesis. The discussion is also limited to surfaces of conducting targets.

The ion-surface interaction is mostly treated in terms of a combination of classical and quantum mechanics. The projectile trajectory is treated classically and is described by trajectory-changing binary projectile-target atom collisions using Monte Carlo techniques. A well-known and often used code is MARLOWE [37, 38]. Electronic interactions between ion and surface are mostly treated quantum mechanically. The target electrons are usually described as a non-interacting free Fermi gas. Projectile electron orbitals are described by hydrogenic wave functions. The electronic exchange interaction between ion and surface is treated in terms of overlap between the target states and the projectile states.

In the early fifties, Hagstrum [39] performed experiments on Auger ejection of electrons from metals by ions. After his pioneering work the field has grown strongly. Many types of experiments, covering a wide range of ion-surface combinations, have been performed. For an overview see *e.g.* Arnau *et al* [13] and Winter [14]. However, because of the above mentioned complexity, there are still many questions that remain to be answered, especially concerning the dynamic neutralization of MCI's in front of a surface (this thesis).

In section 2.2, the most widely used neutralization model, the Classical Over

the Barrier (COB) model, will be outlined. The over-the-barrier approach was originally developed for describing electron capture by MCI's colliding on atoms [40, 41, 42]. Later, the COB model was modified to describe the neutralization of MCI's in front of metal surfaces [43, 44].

Section 2.3 deals with reaction processes which can occur due to the ion-surface interaction. Autoionization (section 2.3.5) and radiative decay (section 2.3.6) are throughout this thesis the most important processes.

Atomic units (a.u.), $\hbar = 1$, $e = 1$ and $m_e = 1$, will be used throughout this thesis. See Appendix 1 for an overview of the values of the atomic units.

2.2 Classical over the barrier model

Conceptually, the COB model for neutralization of an ion (projectile) in front of a conducting surface (target) is very simple: an electron will be exchanged between target and projectile when the 'classical' electrostatic potential between them is low enough to allow for resonant transfer of the electron 'over the barrier'. According to the COB model, on the way towards the surface the ion is neutralized *stepwise* by successive electron capture. The potential barrier between ion and surface, experienced by an electron $-e$, is formed by the combined potential of the ion with charge state $+q$ and the potentials of the *image charges* of the ion $-q$ and the electron $+e$. This is illustrated in figure 2.1.

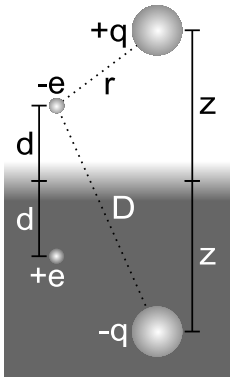

Figure 2.1: Illustration of the image charges.

These image charges are deduced from the following: When an ion approaches the surface, free electrons in the target are attracted by the electrostatic force (between projectile and target) towards the surface. The attracted electrons bundle into an electron cloud that 'screens' the surface from the incoming charge. In the adiabatic limit, *i.e.* when the projectile velocity v_i is

much smaller than the Fermi velocity v_F of the target electrons, the screening effect of the electron cloud can be described in terms of a classical electrostatic image potential V_t.

The description in terms of images requires the existence of an image plane close to the surface. The surface is usually defined as the point where the target electron density has dropped to half of its original value, *i.e.* the 'jellium edge'. The jellium edge is usually situated about half an atomic layer above the topmost atomic layer. The image plane does not exactly coincide with the jellium edge ($z = 0$) but lies (mostly) just slightly outside the jellium surface ($z > 0$) [45]. For our purposes the difference is negligible and therefore we take $z = 0$ as the position of the image plane (surface).

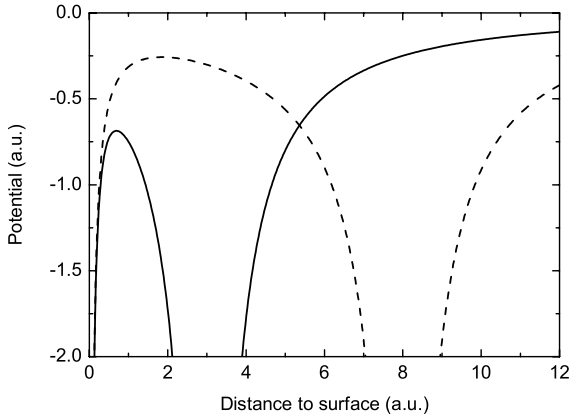

Figure 2.2: The electron potential V_t versus distance d above the surface for a doubly charged ion at 3 and 8 a.u. distance from the surface.

The total potential V_t experienced by the electron at position d in front of the surface is the sum of the ion potential (at $+z$), the ion image potential (at $-z$) and the self-image potential of the electron (at $-d$). Assuming the electron to be positioned on the ion-surface axis and using the substitutions $r = z - d$ and $D = z + d$, one obtains for the 1D potential

$$V_t = -\frac{q}{z-d} + \frac{q}{z+d} - \frac{1}{4d} \tag{2.1}$$

Figure 2.2 shows the total potential V_t, for a projectile in charge state $q = 2$, when the ion is located at $z = 8$ a.u. (dashed line) and at $z = 3$ a.u. (solid line) in front of the surface. Negative distances correspond to penetration into the target. From fig. 2.2 it can be seen that the potential barrier is lowered as the ion comes closer to the surface.

The critical distance z_0 at which the COB neutralization sequence starts can be estimated as follows. Classically, the position z_0 is reached when the saddle point V_s of the total potential V_t (located between the projectile and target) is lowered and becomes equal to the work function ϕ of the surface. Then surface electrons at the Fermi level, *i.e.* the least bound electrons, can resonantly transit over-the-barrier.

The position of the saddle point is found by equating the partial derivative of the potential to zero, *i.e.* $\partial V_t/\partial d = 0$. To a very good approximation, the position of the saddle point is then given by [43]

$$d_s = \frac{z}{\sqrt{8q+2}} \approx \frac{z}{\sqrt{8q}} \tag{2.2}$$

Note that the position of the saddle point only depends on the position z and the charge state q of the incoming projectile. Inserting d_s into equation (2.1), one finds for the saddle point potential

$$V_s = -\frac{\sqrt{8q+2}(16q+1)}{4z(8q+1)} \approx -\frac{\sqrt{2q}}{z} \tag{2.3}$$

Equating V_s to the work function ϕ of the surface, gives the neutralization distance z_0 for COB neutralization [43]

$$z_0 = \frac{\sqrt{8q+2}}{2\phi} \approx \frac{\sqrt{2q}}{\phi} \tag{2.4}$$

The principal quantum number n of the state into which first neutralization takes place, can be calculated in a hydrogenic approximation and is found to be [13]

$$n = \frac{q}{\sqrt{2\phi}}\left(1+\frac{q-1/2}{\sqrt{8q}}\right)^{-1/2} \approx \frac{q}{2\sqrt{\phi}} \tag{2.5}$$

One of the prominent effects of the image interaction - especially for MCI's - is the acceleration of the ion towards the surface. This yields an upper bound on the time the ion can spend in front of the surface. The classical image force experienced by an ion with charge state $+q$ at a distance z above the surface is given by $F_{im} = -q^2/(4z^2)$. Assuming stepwise charge transfer each time the ion reaches a z_0 for which the next electron capture is classically allowed, and assuming that the captured electron completely screens one unit of charge of the incoming ion, the total image energy E_{im} gained by the projectile until complete neutralization, is to a fair approximation given by [13]

$$E_{im} = \frac{q^{3/2}}{3}\frac{\phi}{\sqrt{2}} \tag{2.6}$$

Due to the image charges, the projectile states are also modified as the projectile approaches the surface. The binding energy of a projectile valence electron will decrease due to the Coulomb interaction with the image charge of its ionic core. For a valence electron, the additional charges of the self-image and the projectile image result in first order perturbation to a shift ΔE_B of the 'free atom' binding energy E_B [46]

$$\Delta E_B = \frac{2q+1}{4z} \tag{2.7}$$

As the projectile approaches the surface, Resonant Transitions (RT's) between projectile and target states can occur, see section 2.3.1, leading to the formation of an excited projectile state. The excited projectile state has a natural lifetime τ and a natural decay rate $\gamma = 1/2\tau$ [47]. The natural line width Δ_B of the excited projectile state is the FWHM of its Lorentzian intensity distribution $I(E'_B)$

$$I(E'_B) \sim \frac{1}{(E_B - E'_B)^2 + \gamma^2} \tag{2.8}$$

Where E_B and E'_B are the initial and final projectile states, respectively. From equation 2.8 it can be seen that the FWHM is 2γ, which means that the natural line width is $\Delta_B = 2\gamma = 1/\tau$. The RT's increase the decay possibilities of the excited state, *i.e.* γ is increased and the line width is broadened. Resonant transition rates increase exponentially as the projectile approaches the surface and so does the line width.

2.3 Reaction processes

The reaction processes discussed in this section can be divided into two classes: primary and secondary reaction processes. Primary processes involve charge exchange, or electron transfer, between projectile and target. The secondary processes are pure projectile related de-excitation processes. The primary reaction processes are sub-divided into four types: Resonant Transitions (RT), Collective Excitations (CE), Auger Neutralization (AN) and Auger De-excitation (AD). The secondary reaction processes are sub-divided into two types: AutoIonization (AI) and Radiative Decay (RD). The primary reaction processes will be discussed first. Then, the secondary processes will be treated in some more detail.

2.3.1 Resonant transitions

One or more electrons are resonantly exchanged between target and projectile. There is no excess energy and no electrons are emitted. In figure 2.3, a plot of

the binding energy E_B versus the distance to the surface, the RT's schematically indicated. The target (solid) density of states is shown on the left side of the abscissa, the discrete projectile (ion) states on the right. There are two types of over-the-barrier RT's: Resonant Neutralization (RN), in which the projectile is neutralized by target electrons, and Resonant Ionization (RI), in which the projectile is ionized by losing electrons to the target. Also shown is Quasi Resonant Neutralization (QRN), in which the projectile is neutralized by 'quasi resonant' tunneling of target electrons through the potential barrier. Especially for MCI's, the RT's already occur at large distances above the surface because of the low potential barrier for high charge states. Therefore, certainly in the initial stages of the interaction, tunneling processes play only a minor role and can be neglected.

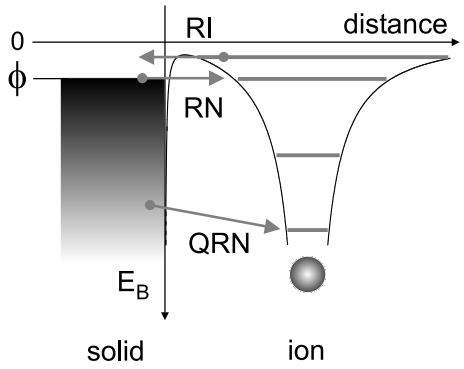

Figure 2.3: Resonant transitions.

The rate Γ_{RT} with which an electron can be exchanged between target and projectile $+q$, located a distance z in front of the surface, is to first order given by Fermi's golden rule (see *e.g.* [39, 35])

$$\Gamma_{RT} = 2\pi \left|H_{fi}\right|^2 \rho_f \tag{2.9}$$

Here, ρ_f is the density of final states and H_{fi} is the coupling between the final (projectile) state $|\psi_f\rangle$ and the initial (target) state $|\psi_i\rangle$. The density of the final projectile states is completely specified, therefore ρ_f is equal to the Density Of States (DOS) of the target at an energy resonant with the projectile energy level. The coupling between the final and initial state is given by the matrix element

$$H_{fi} = \left\langle \psi_f \left| -\frac{q}{r} \right| \psi_i \right\rangle \tag{2.10}$$

The potential centered between the brackets is the attractive Coulomb potential of the projectile nucleus. The electron is located a distance r from the projectile center. Since the final and initial wave functions decay exponentially with

increasing z, so does the matrix element H_{fi}. The rate Γ_{RT} will therefore also decay exponentially for large z, *i.e.*

$$\Gamma_{RT}(z) = \Gamma_{RT}(0)e^{-\alpha_{RT}z} \tag{2.11}$$

The maximum rate $\Gamma_{RT}(0)$ is obtained at $z = 0$. The factor α_{RT} is the inverse decay length of the coupling matrix element H_{fi}. Resonant transition rates $\Gamma_{RT}(0)$ are typically in the range between 0.01 and 0.1 atomic units, which is about $\sim 10^{15}$ Hz (see chapter 6).

2.3.2 Collective excitations

A target electron is captured into a more strongly bound projectile state, the excess energy is stored into the target electronic structure causing an excitation involving many electrons, called a *plasmon* [48]. No electrons are emitted during or after this reaction process. Figure 2.4 schematically shows the Collective Excitation (CE). Collective excitations can be recognized as 'dips' in the energy distribution of target electrons emitted during ion bombardment [49]. Bulk plasmons can be distinguish from surface plasmons by differences in energy, *e.g.* for Al $\hbar\omega_b \sim 15$ eV and $\hbar\omega_s \sim 10$ eV [49].

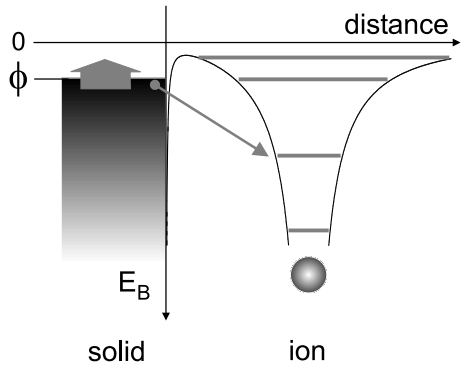

Figure 2.4: Collective excitations.

2.3.3 Auger neutralization

A target electron is captured into a more strongly bound projectile state, the excess energy is used to eject an electron from the target into the vacuum. Figure 2.5 schematically shows the Auger Neutralization (RN) process. The maximum kinetic energy E_k of the Auger electron emitted from the target is $E_k = E_B - 2\phi$. Here, E_B is the binding energy of the projectile level and ϕ is the work function. In this case both electrons originate from the top of the (solid)

valence band, *i.e.* the Fermi level, maximizing the energy difference between target and projectile level. The width ΔE_k is given by the self-convolution of the Surface Density of States (SDOS).

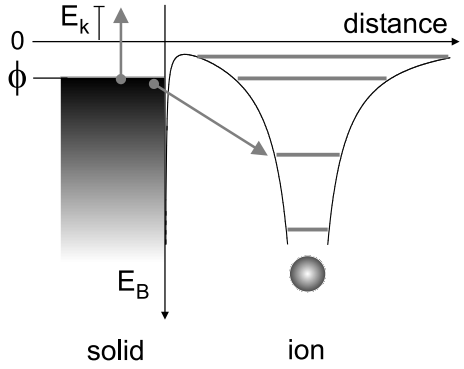

Figure 2.5: Auger neutralization.

The AN rates depend like RT's on the coupling between final (projectile) state $|\psi_f\rangle$ and initial (target) state $|\psi_i\rangle$, but the coupling matrix element H_{fi} is now determined by the repulsive electron-electron interaction. Like in the case of the RT's, at least for large z, the AN rate also decays exponentially with increasing z

$$\Gamma_{AN}(z) = \Gamma_{AN}(0)e^{-\alpha_{AN}z} \tag{2.12}$$

For small z the structure of the wave functions has to be taken into account. The decay rate depends on the inverse decay length α_{AN} and has a maximum value of $\Gamma_{AN}(0)$. Typical AN rates $\Gamma_{AN}(0)$ are in the range between 0.01 and 0.5 a.u. [50].

2.3.4 Auger de-excitation

A surface electron is captured into a more strongly bound projectile state, the excess energy is used to eject a less strongly bound projectile electron into the vacuum. The AD process is depicted in figure 2.6. The maximum energy of the Auger electron emitted from the projectile is $E_k = E_B - \phi - E'_B$, where E_B and E'_B are the binding energies of the more strongly bound and the less strongly bound projectile levels, respectively. Like in the case of AN, the width ΔE_k reflects the SDOS and the final and initial states involve projectile and target, respectively. Therefore the AD process is comparable to the AN process and the rates $\Gamma_{RD}(0)$ range between 0.01 and 0.5 a.u..

The secondary reaction processes, radiative decay and autoionization of excited projectile states, will now be discussed. These processes typically occur

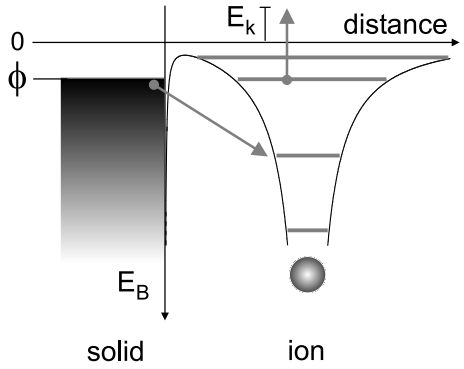

Figure 2.6: Auger de-excitation.

after a primary charge exchange process between target and projectile. Both processes are of importance in the discussion on the spin-polarized surfaces (chapter 5), since two spectroscopic techniques, AES and ECS, based on these processes are employed to study spin ordering effects.

2.3.5 Autoionization

Of all reaction processes discussed so far, for the work presented in this thesis AutoIonization (AI) [51] is one of the most important process, since it will be employed to study spin-polarized surfaces (chapter 5). The AI process is schematically shown in figure 2.7. An excited projectile, *e.g.* a MCI neutralized via RN, decays under the emission of a projectile electron into the vacuum. The kinetic energy of the emitted electron - the Auger electron - is given by $E_k = E_B - E'_B$, *i.e.* the difference in total binding energy between the initial E_B and the final E'_B states.

The AI decay rate Γ_{AI} is given by Fermi's Golden rule. The density of final states ρ_f is now purely atomic and thus well-defined

$$\Gamma_{AI} = 2\pi \left|H_{fi}\right|^2 \rho_f \tag{2.13}$$

The coupling H_{fi} between the final $|\psi_f(1,2)\rangle$ and initial $|\psi_i(1,2)\rangle$ atomic states is given by the matrix element

$$H_{fi} = \left\langle \psi_f(1,2) \left| \frac{1}{|\vec{r}_1 - \vec{r}_2|} \right| \psi_i(1,2) \right\rangle \tag{2.14}$$

The potential centered between the brackets is the repulsive electron-electron potential. Autoionization is an intra-atomic process and therefore Γ_{AI} does not depend on the distance to the surface. In general, AI rates depend only

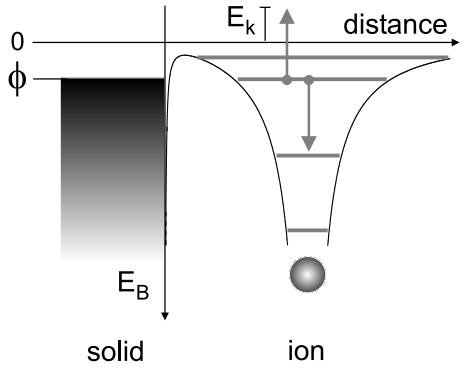

Figure 2.7: Autoionization.

weakly on the nuclear charge Z of the projectile and in light elements this is the dominant decay process. There exists atomic structure software which allows for *ab initio* calculations of AI decay rates [52]. AI transition rates Γ_{AI} are, depending on the states involved, in the range between 0.001 to 0.01 a.u., which is about 10^{14} Hz (see chapter 6 and *e.g.* [43]).

Since the initial and final projectile states are well-defined, so is the energy of the Auger electron. The energy resolution ΔE_k with which the energy distribution $I(E_k)$ of the Auger electrons can be measured is therefore experimentally limited. The spectroscopic technique used to obtain $I(E_k)$ is called Auger Electron Spectroscopy (AES) and the measured distribution is also called an 'Auger spectrum'. High resolution electrostatic analyzers (section 3.3.2) can resolve the fine structure of the projectile states. Hence, it is possible to measure the population of the individual projectile states during the ion-surface interaction. In turn, this can provide important information on the neutralization dynamics and on *e.g.* the spin polarization of the target electrons (chapter 5).

2.3.6 Radiative decay

An excited projectile can decay to a stronger bound state by the emission of a photon. The wavelength of the emitted radiation is given by $\lambda = hc/(E_B - E'_B)$, where E_B and E'_B are the initial and final state binding energies, respectively. The Radiative Decay (RD) process is shown in figure 2.8. Photon emission rates Γ_P increase rapidly with increasing nuclear charge Z, for hydrogen-like wave functions even as fast as Z^4. RD is thus not very likely to occur in light elements but becomes more likely for the heavier elements. Typical rates for hydrogenic ions are given by $\Gamma_P \simeq 4 \cdot 10^{-7} Z^4/n^{4.5}$ [53].

As mentioned above, the RD process is also used to study spin-polarized

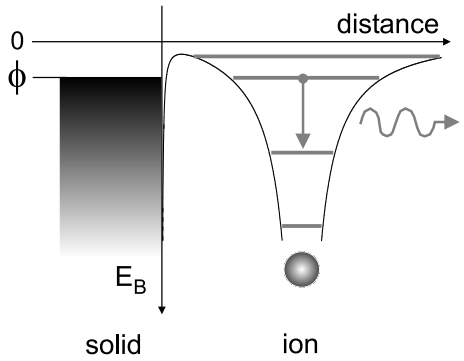

Figure 2.8: Radiative decay.

surfaces. By analysis of the degree of polarization of the fluorescence of the decaying excited projectile states E_B, information on the electron distribution over the available projectile states can be obtained (chapter 5).

Chapter 3

Experiment

3.1 Introduction

The research described in this thesis was done within the Atomic Physics group at the Kernfysisch Versneller Instituut (KVI) in Groningen. The Atomic Physics experiments are located within the KVI main building in a separate experimental hall called 'bronzaal'. The central infrastructure of the bronzaal consists of a Highly Charged Ion (HCI) source, an analysis magnet and a central beam line to which 4 permanent experimental setups are connected. A fifth port is available for guest experiments. Figure 3.1 shows a schematic overview of the bronzaal.

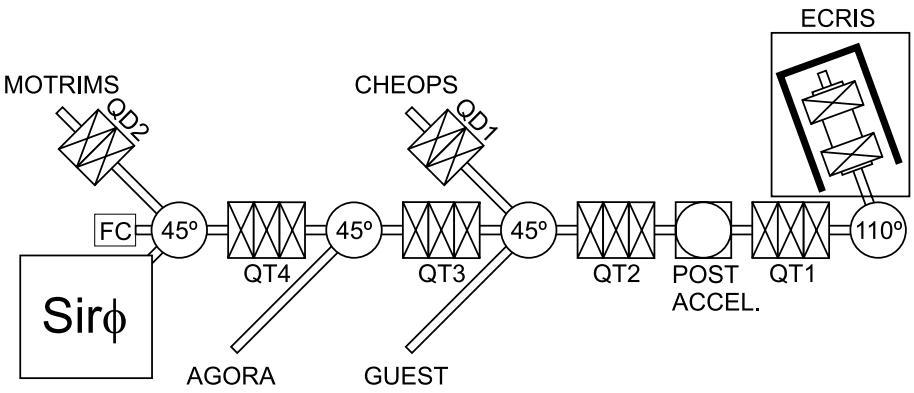

Figure 3.1: The bronzaal. The highly charged ions are produced by the ECRIS and guided through the beam line to the different experiments.

Highly charged ions are produced by an Electron Cyclotron Resonance Ion Source (ECRIS), see section 3.2. The HCI's first pass a 110° analysis magnet and are then guided and focussed through the beam line by sets of Quadrupole Triplets (QT). With the aid of 45° bending magnets the beam is finally guided, sometimes via an additional Quadrupole Doublet (QD), into the different experimental setups. Ion beam energies range from $(2-25)q$ keV, q being the charge state of the ion. The post acceleration stage is used to create accelerated ion bunches of energies up to $140q$ keV.

All Atomic Physics experiments within the bronzaal deal with charge transfer, or with processes induced by charge transfer, in interactions of HCI's with various forms of matter.

MOTRIMS: Here, the HCI's interact with a laser cooled sodium target in a Magneto-Optical Trap (MOT). The low energy recoil ions (Na^{q+}) are extracted towards a position sensitive detector. The position and time of arrival information allows for a determination of the momentum transfer and the impact parameter for each collision. The experiments focus on impact parameter dependent electron capture.

AGORA: HCI's interacting with atoms and small molecules (H_2, CO) in the gas phase lead to light emission in the vacuum ultraviolet and visible spectrum. By means of photon emission spectroscopy, the velocity dependent reaction cross sections are measured. The aims are to provide a basis for plasma diagnostics and to identify interaction processes between the solar wind ions and neutral matter from comets.

CHEOPS: Here, molecules and (atom) clusters are the target gasses for the HCI's. Ionization and fragmentation of these gasses have been studied by coincident time-of-flight mass spectrometry. Now, bio-molecules like uracil, thymine (RNA/DNA base molecules) are studied to achieve deeper knowledge on biological radiation damage on a molecular level.

In a separate room, a fifth experiment, not involving HCI's, is under construction. **ALCATRAZ**: The goal is to detect the extremely rare (natural abundance $\approx 10^{-15}$) ^{41}Ca isotope. Calcium is evaporated from an oven (thermal beam), slowed down and pre-selected by a Zeeman-slower and finally trapped in a MOT where the fluorescence of the isotope is measured. This method can possibly be used in archeological dating back to the pleistocene, because ^{41}Ca has a half-life of 100.000 years.

The work described in this thesis concerns experiments done with the SURface PHYsics setup (**SURPHY** $\rightarrow$ **Sir**ϕ), located at the end of the beamline (see fig. 3.1). Actually, two setups were used for the experiments: the previous version Sirϕ, which is thoroughly described in [35, 54, 36], and the completely upgraded version Sirϕ^{++}. This setup will be described in more detail below. In both setups, Auger Electron Spectroscopy (AES), Ion Scattering Spectroscopy (ISS) as well as Time-Of-Flight (TOF) can be used for surface analysis and

characterization. Future experiments on magnetic surfaces and/or thin magnetic films will require the use of Electron Capture Spectroscopy (ECS) and AES. These techniques might probe short-range (AES) as well as long-range (ECS) magnetic ordering effects on surfaces.

3.2 ECRIS

Figure 3.2 schematically shows the main parts of the ECRIS. Starting from the left, the gas enters the (cylindrical) vacuum chamber via a long small tube which is also used to couple in the Radio Frequency (RF) power. The vacuum chamber is placed inside a strong hexapole magnet which creates a strong (permanent) radially increasing magnetic field. Two powerful solenoids (injection and extraction) provide the axial fields, completing the *magnetic trap*. An RF field, amplified by a Klystron tube, is coupled into the same region. The kinetic energy of the HCI's is determined by the source potential V_S (max 25 kV), applied to the vacuum chamber and gas/RF tube, and the plasma potential V_P. The plasma potential comes from the repulsive potential of the remaining plasma ions and is typically in the range of 10-25 V. The kinetic energy of the HCI's with charge state q leaving the ECRIS is then $E_{kin} = q(V_S + V_P)$ eV. The HCI's are extracted through a diaphragm and a puller, see figure 3.2 on the right. Sometimes a negative potential is applied to the puller to increase the extraction field and thus the output current of the source.

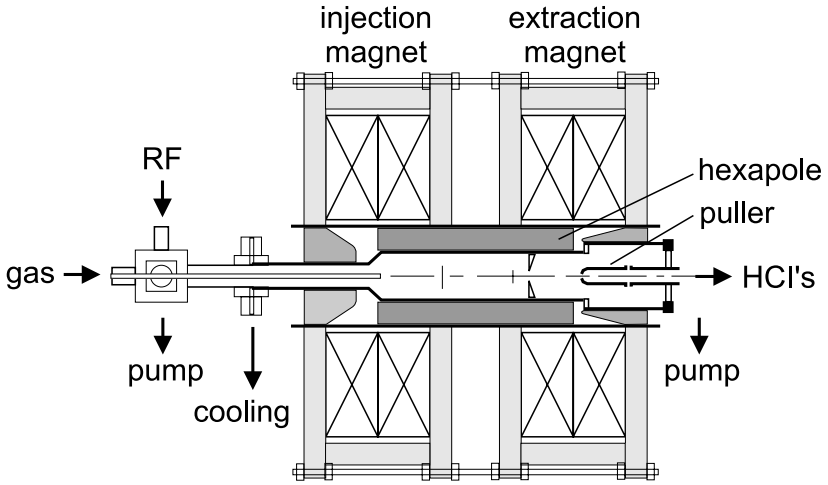

Figure 3.2: Schematic drawing of the Electron Cyclotron Resonance Ion Source (ECRIS).

The charge states of HCI's extracted from the plasma span a broad range. To select (only) the correct projectiles, the extracted HCI's are analyzed according to their mass A over charge state q ratio (A/q) by the 110° analysis magnet. The magnetic field B of the analysis magnet is proportional to $\sqrt{V_S A/q}$. The A/q-resolution of the analysis magnet is 0.5%.

The beam output is measured by a movable Faraday cup, placed after the analysis magnet. Before injection into the beam line, the beam diameter is collimated by a 10 mm diaphragm. Typical ion beam currents range from a few tens of nA (*e.g.* O^{7+}) up to a few hundred μA (*e.g.* He^{+}), depending on element and charge state.

In an ECRIS, highly charged ions are produced stepwise by electron impact ionization. The electrons inside the *plasma* are gyrating around the magnetic field $\vec{B}$ with frequency $\omega = e|\vec{B}|/m_e$, thus ionizing the atoms/ions. Moreover, electrons gyrating in the direction $\hat{x}$ of an increasing magnetic field experience a repulsive magnetic force perpendicular to $\hat{x}$. Depending on the gradient $\partial B_x/\partial x$ of the field and on the electron velocity v_x, the movement can be reversed, effectively reflecting the electrons. This way electrons are confined inside the trap and a sufficient electron density can be obtained. High energy electrons are produced by applying the RF field. When the RF frequency equals the revolution frequency ω *electron cyclotron resonance* occurs: the electrons are resonantly accelerated by the RF field. By choosing a proper combination of magnetic strength (about 0.5 T) and RF frequency (14 GHz, a few hundred Watt), a closed ECR surface, along which the resonance condition is fulfilled, can be obtained [55, 56].

The (maximum) charge state of the HCI's (produced inside the ECRIS) is limited by: neutralization by electron capture, the energy distribution of the electrons and the confinement time of the HCI's inside the trap. Electron capture mainly stems from ion-neutral collisions and can be minimized by a low background pressure inside the source. Typical ECRIS background pressures are of the order of 10^{-5} Pa. The ionization potential of hydrogen-like ions scales with Z^2 and the cross section for electron impact ionization peaks at about twice this value. Therefore, achieving high charge states implies the electrons to span a wide kinetic energy range. For example, for the sequential ionization of oxygen up to fully stripped O^{8+}, one needs electrons with energies in the range of 25 eV - 1800 eV.

3.3 Surface physics setup

The new experimental setup Sirϕ^{++} basically consists of a cylindrical (300 mm diameter) collision chamber with a big manipulator placed on top[1]. A powerful

[1] All manufactured by Thermo Vacuum Generators, Hastings, United Kingdom.

getter ion pump is placed underneath the UHV collision chamber. This chamber is made out of 5 mm thick μ-metal and top and bottom parts of the chamber are magnetically shielded by custom-made 3 mm thick μ-metal shields, mounted inside the vacuum chamber. The μ-metal prevents stray magnetic fields from penetrating into the chamber and thus into the electron detection volume. Residual magnetic fields are of the order of a few μT. The chamber is permanently pumped down by the 400 l/s getter ion pump to a base pressure in the 10^{-8} Pa range. During sample preparation cycles and after a venting procedure, the setup is pumped down by a roughing system consisting of a turbo pump and a forepump. Figure 3.3 shows a photograph of the new Sirϕ^{++} setup.

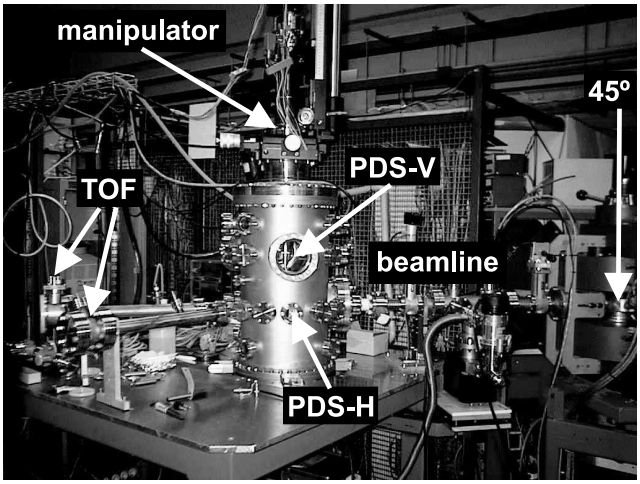

Figure 3.3: Photograph of the new Sirϕ^{++} setup. (The HCI's are coming from the right.)

The vacuum chamber was originally designed as a three level system: one level for experiments and two levels for surface preparation and analysis. The lowest level (level A) is the experiment level, located at the height of the beamline which is 1400 mm above ground level. This level is currently also used for surface preparation and ECS. Level B is located 180 mm above level A and is also used for ECS. Level C is located 100 mm above level B. The level structure of the collision chamber requires vertical translation of the sample which is realized by the manipulator.

The manipulator has three translational degrees of freedom: $\Delta X = \Delta Y = \pm 12.5$ mm and $\Delta Z = 0 - 400$ mm, and two rotational degrees of freedom: $\Delta\psi = \pm 180°$ and $\Delta\phi = \pm 110°$. A disadvantage of such a big manipulator is the diameter of the manipulator axis, which increases in thickness from

bottom (sample) to top (also see section 3.3.3). The manipulator is equipped with 3 stepper motors (Z, ψ and ϕ) and a low-magnetic sample holder. The sample holder facilitates LN_2-cooling (-170°C), electron bombardment heating (+1200°C) and is equipped with two low-magnetic N-type thermocouples and molybdenum base plate and clamps. The manipulator is placed on top of the setup and the manipulator axis points down vertically, resulting in a vertical position of the sample[2].

Inside the collision chamber, a four-element electrostatic lens system and a high resolution semi-hemispherical ElectroStatic Analyzer (ESA) are mounted. Connected to the chamber are: electron gun, ion gun, TOF tube and chopper-sweeper plates[3]. All these devices are positioned at the height of experimental level *A*. For gas analysis and base pressure information, a (quadrupole) Residual Gas Analyzer (RGA) and an ionization gauge are mounted at level *C*.

In the near future, the sample analysis and preparation techniques will be even more advanced by adding the following units: an evaporator for the evaporation of thin (magnetic) films, a Kelvin probe for determination of the work function, an X-ray source for Photoemission Spectroscopy (XPS), and a small laser setup with polarization optics for *in situ* Magneto-Optical Kerr Effect (MOKE) measurements of magnetic samples.

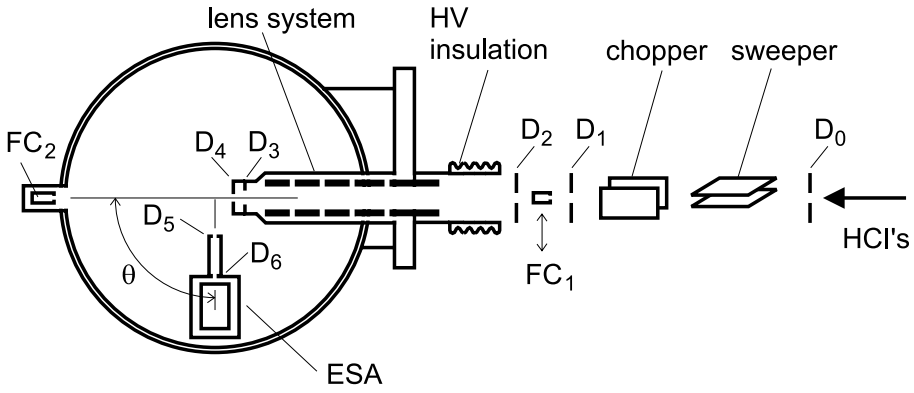

Figure 3.4: Schematic drawing of the setup showing the diaphragms, the chopper sweeper section, the lens system and the ESA.

The setup is connected to the third 45° magnet via the beam line section that accommodates the chopper sweeper plates used for TOF measurements, see figures 3.3 and 3.4. This beam line section is differentially pumped down by a small getter ion pump to a base pressure of a few 10^{-7} Pa. The primary ion

[2]The normal to the sample surface $\hat{n}$ lies in the horizontal XY-plane.
[3]For a complete description of the TOF system see [36, 57].

beam first enters the beam line section (diaphragms $D_0 = 2$ and $D_1 = 1$ mm), then passes through the lens system (diaphragms $D_2 = 2$ and $D_3 = 2$ mm) and the collimation diaphragm $D_4 = 1.5$ mm and finally reaches the sample. Figure 3.4 schematically shows an overview of the diaphragms.

The overall transmission (from analysis magnet to sample) is of the order of 1% and depends somewhat on the A/q ratio of the HCI's. For large A/q, the transmission tends to be a little worse. The beam intensity can be determined by monitoring either the current measured by a movable Faraday cup, positioned just in front of the lens system, and/or the sample current[4]. The latter is monitored during the measurements to correct for beam fluctuations. Typical sample currents range between a few tens and a few hundred nA, but can also be up to a few μA in case of singly charged helium ions.

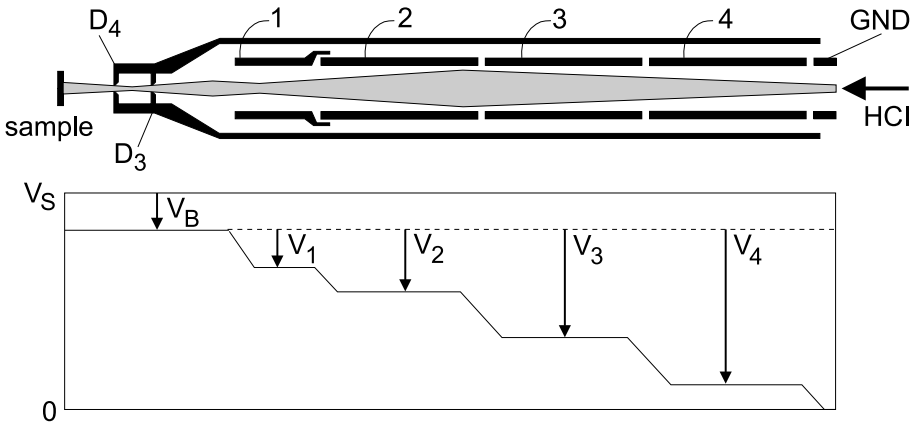

Figure 3.5: Beam deceleration. In the upper part the outcome of a SIMION simulation is shown. The lower part indicates the lens voltages along the trajectory.

3.3.1 Beam deceleration

Up to diaphragm D_2, the beam line is on ground potential. In between diaphragms D_2 and D_3 the ion beam can be decelerated. This is achieved by floating the complete setup, including the pumps and the electronics, on a potential which is defined by the source potential V_S and a bias potential V_B, *i.e.* $V_{setup} = V_S - V_B$. The actual deceleration takes place in a four-element electrostatic lens system [35], mounted between diaphragms D_2 and D_3. The lens system induces no extra beam loss for deceleration factors up to 100, while

[4]The sample current is the sum of the impinging ion current and the secondary particles (electrons/ions) leaving the target.

the beam spots on the target are only slightly larger than for the undecelerated beams. For even larger deceleration factors the beam diverges more strongly and therefore the collimation diaphragm D_4 is mounted.

The kinetic energy of the HCI's leaving the ECRIS is determined by $E_{kin} = q(V_S+V_P)$, where V_P is the plasma potential. HCI's with charge state q entering the Sirϕ^{++} collision chamber have to overcome the applied setup potential V_{setup}. The final kinetic energy of the projectiles is then $E_{kin} = q(V_S + V_P) - q(V_S - V_B) = q(V_B + V_P)$. This way the beam energy is determined by V_B and possible fluctuations in V_S are cancelled. Figure 3.5 shows a SIMION simulation of the transport of an ion beam through the lens system. In this case, a beam of He^{2+} ions with a primary kinetic energy of 14 keV ($V_S = 7.0$ kV) is decelerated to an energy of 500 eV ($V_B = 250$ V, V_P was not included).

3.3.2 Electrostatic analyzer

All electron and ion energy spectra presented in this thesis are measured using a 180° semi-hemispherical high resolution ElectroStatic Analyzer (ESA). In an ideal hemispherical ESA, electrostatic potentials are applied on both (concentric) hemispheres causing an electrostatic field in between. For a projectile with charge state q and mass m to pass the ESA, the radial equation of motion $m\ddot{\vec{r}} = \vec{F}_{cp} + \vec{F}_r = 0$ needs to be satisfied. Here, $\vec{F}_{cp}$ is the (outward) centripetal force and $\vec{F}_r$ is the (inward) radial force from the electrostatic field $\vec{E}_r$. After calculating the electrostatic field between the hemispheres, one obtains the radial equation[5]

$$\frac{m\dot{r}^2}{r} = \frac{q(V_2 - V_1)R_1R_2}{(R_2 - R_1)r^2} \tag{3.1}$$

A charged particle with kinetic energy $E_k = m\dot{r}^2/2$ will pass the ESA on the central trajectory $r = (R_1 + R_2)/2$ if it satisfies the condition

$$E_k = q(V_2 - V_1)F \tag{3.2}$$

Here, F is the proportionality factor of the ESA

$$F = \frac{1}{R_2/R_1 - R_1/R_2} \tag{3.3}$$

The electrostatic potentials (V_1 and V_2), applied to the inner and outer hemisphere ($R_1 = 48$ and $R_2 = 52$ mm, respectively), are chosen such that the electrostatic potential V_r on the central trajectory ($r = 50$ mm) is zero[6]. For an ideal hemispherical ESA, this situation is reached when $V_2/V_1 = -R_1/R_2$. Inserting the radii gives $V_2/V_1 = -0.923$ and $F = 6.24$. Since our ESA consists

[5] All radii are measured from the ESA center.

[6] Then the particle is not slowed down by the electrostatic field inside the ESA.

of two central slices of hemispheres, it is only semi-hemispherical and therefore the factors deviate slightly from the ideal values. Calibration of our ESA gave $V_2/V_1 = -0.935$ and $F = 6.42$ [54].

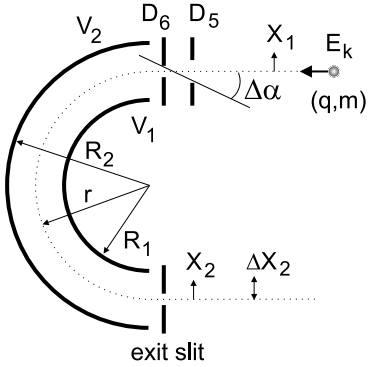

Figure 3.6: Schematic representation of the ESA.

Figure 3.6 schematically shows the components of the ESA. The uncertainty in the (vertical) position x_2 of a charged particle entering the ESA at x_1 under an angle $\Delta\alpha$, can be described by the Taylor expansion [58]

$$\Delta x_2 = \frac{\partial x_2}{\partial \alpha}\Delta\alpha + \frac{\partial x_2}{\partial E_k}\Delta E_k + \frac{\partial^2}{\partial \alpha^2}(\Delta\alpha)^2 + \text{ higher order terms} \tag{3.4}$$

After rearrangement of this Taylor expansion, one arrives at an approximate expression for the base energy resolution:

$$\frac{\Delta E_k}{E_k} = \frac{1}{2}\left[\left(\frac{D}{r}\right) + (\Delta\alpha)^2\right] = \text{ constant} \tag{3.5}$$

The first term represents the linear resolution, which depends on the effective diaphragm D and on the central trajectory radius r. The effective diaphragm is the average of the entrance diaphragm D_6 and the exit slit height h, *i.e.* $D = (D_6 + h)/2$. The second term is the apparent energy spread for a mono-energetic beam with angular divergence $\Delta\alpha$. It is a general feature of deflection type analyzers that the energy resolution $\Delta E_k/E_k$ is a constant. Therefore, in all energy spectra presented in this thesis, the number of detected particles (intensity) always represents the raw *counts* divided by the energy, thus correcting for the energy resolution.

Particles entering the ESA first pass diaphragms $D_5 = 1.9$ mm and 41 mm later they pass $D_6 = 0.4$ mm. Diaphragm D_6 is positioned 75 mm from the sample, thus allowing for a solid angle of $\Delta\Omega = \pi(0.2)^2/(75)^2 = 2.23 \cdot 10^{-5}$ sr at the target center. The exit slit measures $h \times w = 0.5 \times 1.9$ mm^2. The

uncertainty in the acceptance is estimated to be 15%. From equation 3.5 the calculated energy resolution for our ESA is about 0.5% FWHM. The total acceptance of the analyzer is: $\Delta\Omega(\Delta E_k/E_k) = 1.12E_k \cdot 10^{-7}$ sr·eV. Electrons with kinetic energies higher than 20 eV entering the ESA can be detected with nearly 100% efficiency. For kinetic energies below 20 eV, the residual magnetic field (a few μT) inside the electron detection area distorts the transmission leading to a loss of detection efficiency.

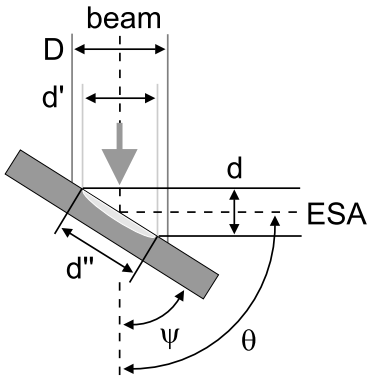

Figure 3.7: Illustration of the ESA geometry correction parameters.

The small acceptance angle and the good energy resolution also make the ESA perfectly suitable for polar scans around the target surface normal $\hat{n}$. The ESA observation angle θ can be varied between 0 and 135° with respect to the HCI beam. However, for polar scans a geometry correction $f(\psi, \theta)$ for the beam spot on the target seen by the ESA has to be applied. In figure 3.7 the scattering geometry is indicated: the HCI beam comes from the top and scatters off the target under an incidence angle ψ. Emitted or scattered particles from the light-gray area are detected by the ESA under an angle θ . The effective diameter d', which is the projection of the ESA spot on the target onto the beam, is compared to the beam diameter D. From figure 3.7 it can be seen that $d'' \sin(\theta - \psi) = d$ and that $d'' \sin(\psi) = d'$. The ESA geometry correction factor $f(\psi, \theta)$ is now defined as D/d', *i.e.*

$$f(\psi,\theta) = \begin{cases} \left(\frac{D}{d}\right)\left(\frac{\sin(\theta-\psi)}{\sin(\psi)}\right) & \text{if } d' \leq D \\ 1 & \text{if } d' > D \end{cases} \tag{3.6}$$

The true intensity $I_0(\theta)$, which should only depend on θ, is then given by the product of $f(\psi, \theta)$ and the measured intensity $I_m(\psi, \theta)$. Since most Auger spectra are taken at $\theta = 90°$ (no Doppler-shift), we use in our experiments a correction factor normalized with respect to the intensity measured at 90°, *i.e.*

$f(\psi, 90) = 1$. In figure 3.8 the normalized correction factor $f(\psi, \theta)$ is plotted as a function of θ for three values of ψ. It can be seen that the correction factor becomes constant for very small values of θ, *i.e.* values close to ψ. At these extreme angles $D/d' < 1$ and the ESA sees the complete beam spot on the target. Obviously, values for $\theta < \psi$ do not exist since this would imply that the ESA looks behind the target surface.

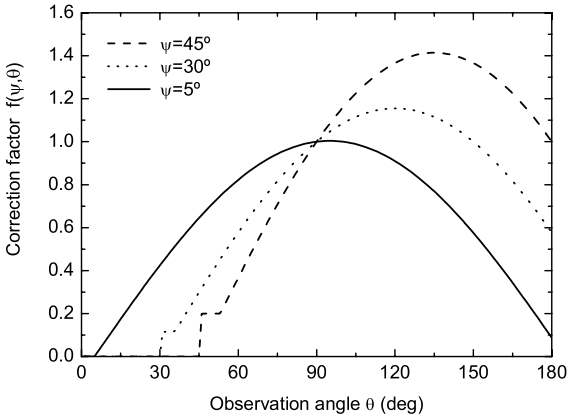

Figure 3.8: The ESA geometry correction effect.

Particles passing the ESA hit a microchannel plate placed directly after the exit slit. The thus generated pulses are amplified, analyzed by a single channel analyzer and counted by a data acquisition card inside the PC that controls the experiment. The electrostatic potentials applied to the ESA, are generated by a computer controlled power supply. The energy accuracy (not the resolution) of the ESA, the data acquisition time and the scanned energy range are all adjustable by the software (LABVIEW) running the experiment. To obtain maximum energy accuracy a voltage division box, which divides the output voltage by a factor 20 or 200, is placed between power supply and ESA. This way, the digitally controlled (discrete) power supply output is divided by the same factor.

3.3.3 Photon detection system

In Electron Capture Spectroscopy (ECS), $He^+(1s)$ ions with keV energy are scattered grazingly off a (magnetized) surface. The ions are neutralized into excited $He^*(1snl)$ states and decay by fluorescence. For the detection of the emitted light and the analysis of the degree of polarization, the Sirϕ^{++} setup

houses two identical photon detection systems with optics for polarization analysis.

Photon Detection System Vertical (PDS-V) is set up to measure light emitted parallel to the sample surface, *i.e.* in the vertical direction (Z-axis). Photon Detection System Horizontal (PDS-H) measures light emitted perpendicular to the surface, *i.e.* in the horizontal direction (XY plane). Part of the optics is placed inside the vacuum chamber in order to focus the light into the PDS. For wavelength-dependent polarization analysis of the emitted light, each PDS is equipped with a rotating quarter waveplate ($\lambda/4$), a linear polarizer and an appropriate interference filter (see table 3.1). The quarter waveplates are rotated by computer controlled stepper motors. For the detection of the (low) light intensities a Photo Multiplier Tube (PMT), type EMI-9789QA (UV sensitive), is chosen. Both photon detection systems are mounted horizontally in front of the setup viewports (quartz). PDS-H is mounted at level A and PDS-V is mounted at level B, 180 mm above level A.

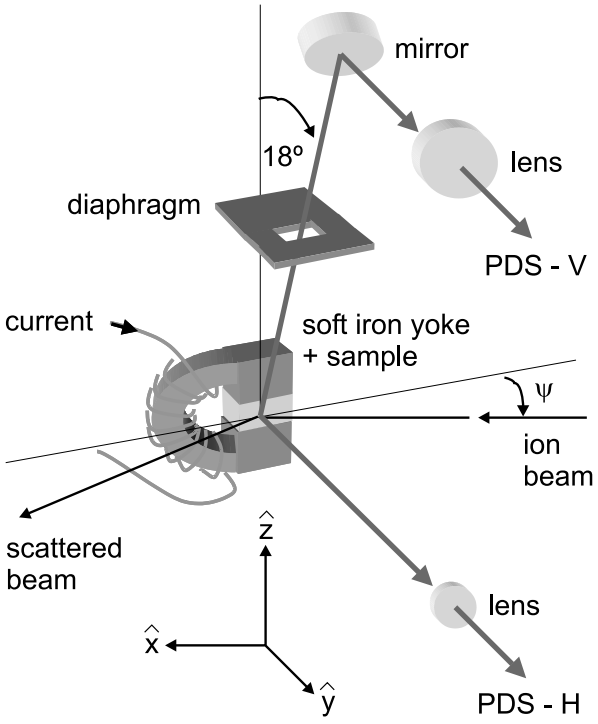

Figure 3.9: The ECS experiment (schematically).

The light emitted parallel to the surface is oriented in the vertical direction. Therefore a 2" mirror, mounted on the manipulator axis, is used to reflect the

light via a 2" bi-convex lens ($f = 100$ mm) into PDS-V. Due to the thickness of the manipulator axis and the dimensions of the mirror, the mirror has an axis offset of 58.5 mm. This puts a lower limit on the surface parallel emission angle of $\arctan(58.5/180) = 18°$. A diaphragm ($4{\times}9$ mm^2) is placed 30 mm above the sample with an axis offset of 10 mm. The diaphragm selects only the important part of the light emission, and thus excludes unwanted emission/reflection from regions close to the sample. The light emitted perpendicular to the sample surface is focussed by a 1" bi-convex lens ($f = 75$ mm) into PDS-H.

Figure 3.9 shows an artist impression of the ECS experimental setup. The undecelerated primary $He^+(1s)$ beam comes from the right and scatters off the sample under an incidence angle ψ. The sample can be (de-)magnetized by sending a current through the soft iron yoke (see 3.3.5). The light rays emitted perpendicular (PDS-H) and parallel (PDS-V) to the surface are indicated by the arrows. The mirror (offset) and the diaphragm (offset) are also schematically shown.

The radiative transitions which we can study are, in order of increasing wavelength, listed in table 3.1.

initial state	$\rightarrow$	final state	λ (nm)
$He^*(1s3p)\ ^3P$	$\rightarrow$	$He^*(1s2s)\ ^3S$	388.86
$He^*(1s4s)\ ^3S$	$\rightarrow$	$He^*(1s2p)\ ^3P$	471.31
$He^*(1s3p)\ ^1P$	$\rightarrow$	$He^*(1s2s)\ ^1S$	501.57
$He^*(1s3d)\ ^3D$	$\rightarrow$	$He^*(1s2p)\ ^3P$	587.56
$He^*(1s3d)\ ^1D$	$\rightarrow$	$He^*(1s2p)\ ^1P$	667.82

Table 3.1: Radiative transitions of excited He I ($1snl$) [59].

The polarization optics, mounted in front of the PMT's, is constructed in such a way that all optical elements can easily be exchanged. This is necessary since the optics used for wavelengths exceeding 400 nm is not applicable for shorter wavelengths (UV).

3.3.4 Polarization analysis

Light properties are usually described in terms of electric fields. The electric field vector $\vec{E}$ of a plane ElectroMagnetic (EM) wave propagating along the z-direction and oscillating in the XY-plane is given by

$$\vec{E} = E_x\hat{x} + E_y\hat{y} \tag{3.7}$$

with harmonic $\hat{x}$ and $\hat{y}$ components

$$E_x = E_{x0}\cos(\omega t - kz + \delta_x) \tag{3.8}$$
$$E_y = E_{y0}\cos(\omega t - kz + \delta_y) \tag{3.9}$$

The polarization of a wave depends on the phase difference between these two components, *i.e.* $\Delta = \delta_y - \delta_x$. The polarization of an EM-wave with fixed frequency $\omega = 2\pi\nu$ and wavenumber $k = 2\pi/\lambda$, is completely described by four parameters: E_{x0}, E_{y0}, δ_x and δ_y. It can be shown that equations (3.8) and (3.9) lead to the description of the polarization in terms of a *polarization ellipse*, given by

$$\left(\frac{E_x}{E_{x0}}\right)^2 + \left(\frac{E_y}{E_{y0}}\right)^2 - 2\frac{E_x E_y}{E_{x0}E_{y0}}\cos(\Delta) = \sin^2(\Delta) \tag{3.10}$$

In 1852, Sir G.G. Stokes introduced four parameters that fully specify the polarization of light. The four Stokes parameters are I, M, C and S. Here, $I = I_p + I_u$ is the total light intensity, with I_p and I_u as the polarized and un-polarized light intensities, respectively. The polarized light intensities M, C and S sum up vectorially as the total intensity of all polarized light, *i.e.* $M^2 + C^2 + S^2 = I_p^2$.

Usually, the time-averages of the intensities are taken and the Stokes parameters are then defined as

$$I = \langle E_{x0}^2 \rangle + \langle E_{y0}^2 \rangle \tag{3.11}$$

$$M = \langle E_{x0}^2 \rangle - \langle E_{y0}^2 \rangle \tag{3.12}$$

$$C = 2\langle E_{x0}E_{y0}\cos(\Delta) \rangle \tag{3.13}$$

$$S = 2\langle E_{x0}E_{y0}\sin(\Delta) \rangle \tag{3.14}$$

The quantities M and C represent linearly polarized light or π light, S represents circularly polarized light or σ light. The magnitudes and signs of the three Stokes parameters depend on E_{x0}, E_{y0} and Δ. For $\Delta = 0°$ pure π light is obtained. For $\Delta = \pm 90°$ and $E_{x0} = E_{y0}$, pure σ light is obtained. When $0° < \Delta < \pm 90°$ and/or $E_{x0} \neq E_{y0}$, which is most common, the light is elliptically polarized.

The polarization of light can experimentally be determined by measuring the light intensity $I \sim |\vec{E}|^2$ with a PMT, after the light passed through a rotating $\lambda/4$-plate and a linear polarizer. The $\lambda/4$-plate introduces a phase shift of 90° between the two components E_x and E_y of the initial electric field vector E, forming a new vector E' with new intensity I'. The linear polarizer then only transmits the projection of E' on its optical axis, the vector E^* with intensity I^*.

To calculate the effects of the polarization optics on the transmitted light, it is most convenient to describe the light in terms of the four Stokes parameters I, M, C and S. The final light intensity $I^*(\beta, \Delta)$ is related to the Stokes parameters as follows [60]

$$
\begin{aligned}
I^*(\beta,\Delta) = \quad & +\tfrac{1}{2} \quad I \\
& +\tfrac{1}{2} \quad M\left[\cos^2(2\beta)+\sin^2(2\beta)\cos(\Delta)\right] \\
& +\tfrac{1}{4} \quad C\left[1-\cos(\Delta)\right]\sin(4\beta) \\
& -\tfrac{1}{2} \quad S\sin(2\beta)\sin(\Delta)
\end{aligned} \tag{3.15}
$$

Where β is the rotation angle of the $\lambda/4$-plate and Δ is the phase difference. By changing β and fitting equation (3.15) to the experimental data, the relative Stokes parameters $M/I, C/I$ and S/I are obtained. In the experiment, there is a mirror placed before PDS-V which changes the polarization by 180°. The sense of rotation of the quarter waveplate is also important for the sign of the polarization.

3.3.5 Sample holders

For the AES measurements on the Pt(110) sample, the original sample holder was used. The disc-like Pt(110) sample, with a circumferential cut, was fixed by means of two molybdenum clamps and a fixating wire wrapped around the cut. The thermocouples were placed close to the sample. Figure 3.10 shows a photograph of the sample holder with the Pt(110) sample.

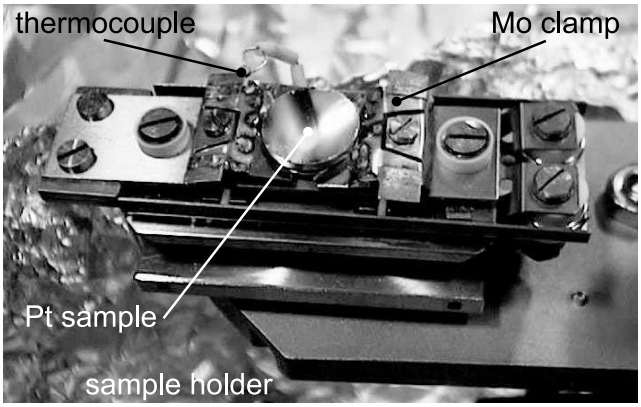

Figure 3.10: Original sample holder with the Pt(110) sample.

The ECS and AES measurements on (de)magnetized Fe(110) and Ni(110) samples were performed on a modified sample holder. In order to effectively magnetize the samples, they are clamped in a semi-toroid, which consists of Kapton wire wrapped around a soft iron yoke (0.02% carbon)[7]. The yoke

[7]Werkspoor NV, Amsterdam, The Netherlands.

(with sample) is mounted on the standard sample holder. Sample heating now takes place via conduction through the yoke. The non-magnetic thermocouples are placed close to the sample. A sheet of copper is mounted on top of the Kapton wire to prevent the assembly from charging up by the impinging ion beam. Figure 3.11 shows the modified sample holder, the (shielded) yoke and the Fe(110) sample. The magnetization is done along the horizontal direction (between the poles) in figure 3.11, which is the vertical direction Z in figure 3.9. The samples used in the experiments were always magnetized along their easy axis of magnetization in order to ensure magnetic saturation of the samples. For the Fe(110) sample, the easy axis of magnetization is along the [001] direction. The Ni(110) sample has its easy axis along the $[1\bar{1}1]$ direction.

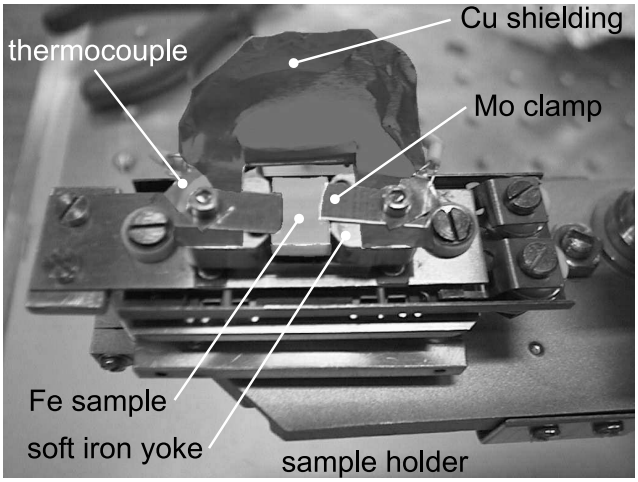

Figure 3.11: The sample holder used for sample magnetization. The Fe(110) sample is clamped in the soft iron yoke.

Chapter 4

Sputtering of hollow carbon atoms

4.1 Introduction

We investigated the emission of Auger electrons from collisions of hydrogen-like ions C^{5+}, N^{6+} and O^{7+} with graphite as well as C_{60} (fullerene or 'Buckyball') covered gold surfaces. Besides the quite well understood Auger electrons emitted from the projectile, an extremely high yield of Auger electrons originating from carbon surface atoms is observed. Remarkably, the target Auger distribution shows discrete (atomic) KLL lines superimposed on the broad KVV distribution originating from bulk carbon. This indicates high sputtering yields of highly excited carbon ions/atoms with K-shell vacancies.

4.2 Sample preparation

The Highly Oriented Pyrolitic Graphite HOPG(0001) target was prepared *ex situ* by means of the standard 'scotch tape' method. The final preparation was done by series of grazing incidence ($\psi = 5° - 10°$) 800 eV Ar sputtering/annealing cycles. C_{60} monolayers on Au(111) were produced following the recipe suggested by Tjeng *et al.* [61]: A large amount of C_{60} is deposited at room temperature on the thoroughly sputtered Au(111). Desorption of bulk C_{60} starts at 180°C, whereas the much stronger C_{60}-Au(111) bond only breaks at temperatures higher than 360°C. Thus, a monolayer coverage of the complete Au(111) surface can be produced by heating the sample to 300°C for a few minutes. Removal of the fullerene layer is accomplished by heating up to 400°C.

4.3 Results

A set of high-resolution Auger spectra from N^{6+} collisions with HOPG is displayed in figure 4.1. The detection angle θ was 90° with respect to the beam and the projectiles were scattered under a glancing angle $\psi = 10°$. The measurements were done at projectile velocities between $v = 0.04$ a.u. and $v = 0.35$ a.u., varied in steps of 0.025 a.u., corresponding to kinetic energies ranging from 0.44 keV to 42 keV. An offset proportional to the velocity has been added to the spectra. All spectra have been normalized to an equal integral over the projectile KLL distribution between 320 eV and 450 eV.

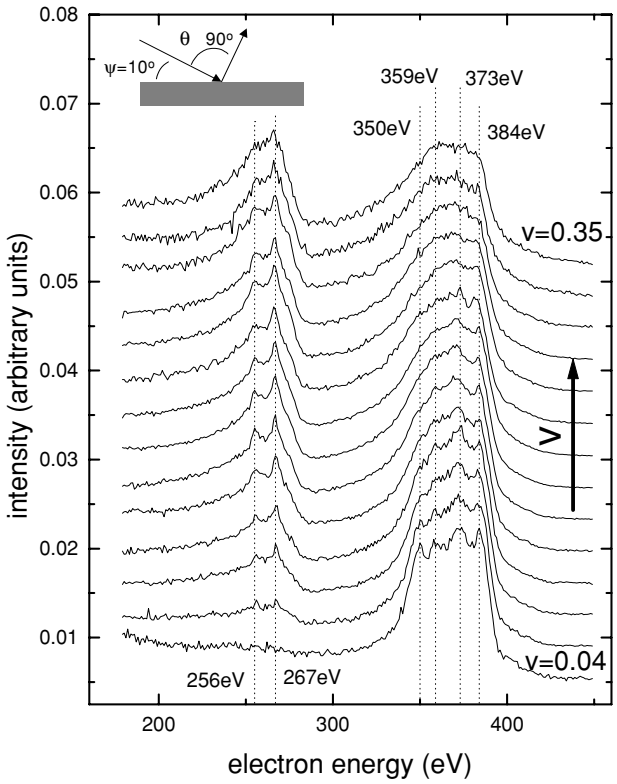

Figure 4.1: Auger spectra from N^{6+} scattered off HOPG plotted for different projectile velocities v.

At the lowest velocities, the broad nitrogen KLL distribution shows discrete structures which can be attributed to Auger electron emission from projectiles with a filled L-shell ($E = 384$ eV), projectiles with a highly inverted population, i.e. only 2 electrons in the L-shell ($E = 350$ eV), or from projectiles with L-shell

fillings in between these extreme cases. The relative intensity of the discrete peaks changes with the projectile velocity v [62]. However, the most striking feature of the spectra is the structure between 200 eV and 280 eV which we attribute to target Auger electron emission from sputtered C atoms. The ratio between target and projectile Auger electrons in fig. 4.1 changes dramatically with increasing v. For $v = 0.04$ a.u. no target Auger emission is observed, whereas at $v = 0.35$ a.u. comparable numbers of target and projectile Auger electrons are found. A closer look at the target Auger structure at intermediate velocities reveals discrete peaks on top of a broad background.

This finding is very remarkable, since the target Auger electrons are expected to originate from bulk graphite. The Auger line shape should then be given by a self-convolution of the target Density Of States (DOS). Even though the graphite DOS has three broad maxima due to the π_p, σ_p and σ_s bands, in the resulting KVV (V denoting the valence band) Auger spectrum all structures are washed out [63] (see also fig. 4.5).

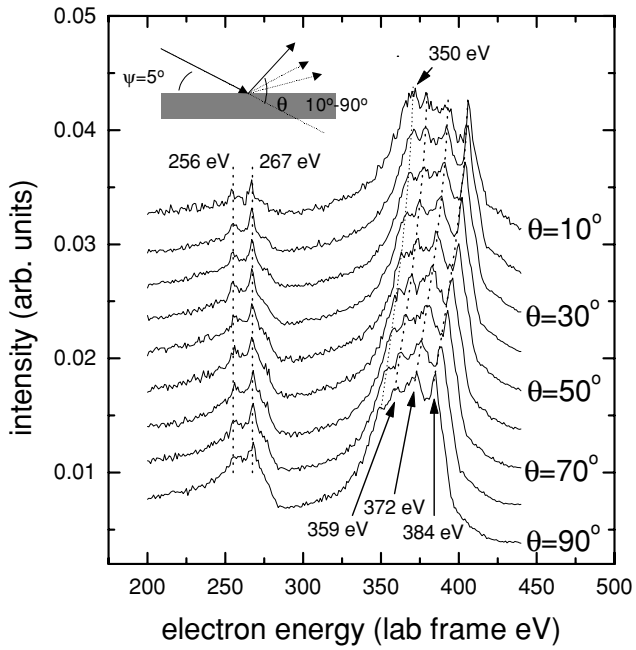

Figure 4.2: Auger spectra from N^{6+} scattered off HOPG at $v = 0.15$ a.u. plotted for different observation angles θ.

To pinpoint the origin of the C Auger electrons we exploit the Doppler-shift of electrons emitted from the projectile when θ differs from the perpendicular

observation angle used in fig. 4.1. In figure 4.2 Auger spectra for constant velocity $v = 0.15$ a.u. measured at different observation angles are displayed. The incidence angle ψ is always 5°. An offset proportional to the observation angle θ has been added to the spectra. As in fig. 4.1, projectile as well as target Auger peaks are observed. As expected, the complete N KLL distribution Doppler-shifts to higher energies when θ is decreasing. The calculated energetic positions for the peaks at 359 eV, 373 eV, and 384 eV are indicated by the dotted lines [65] (also see Appendix 2). It is obvious, that the 384 eV peak is becoming more pronounced for small θ, partly because the corresponding electrons can be emitted on the outgoing part of the trajectory and still be detected. Furthermore, the peak at 350 eV, which is known to result largely from decay processes above the surface [64], becomes more prominent with decreasing θ. This is due to the fact, that the other contributions partly originate from below surface emission processes. For very small observation angles, the corresponding electrons suffer a strong attenuation due to the increasing path length through the HOPG bulk [66].

The target Auger structure between 200 eV and 280 eV shows no Doppler-shift at all. In particular, the peaks at 256 eV and 267 eV are unchanged upon projectile velocity variation (see fig. 4.1). With decreasing observation angle, their relative intensity with respect to the broad background increases strongly. This indicates, that these peaks originate from the topmost layer (or above), whereas the broad structure exhibits the typical angular distribution expected for KVV emission processes in bulk HOPG.

As outlined before, the KVV emission is probably initiated by K-shell vacancy transfer from the projectile to the target [67]. It is therefore a logic test to investigate the interaction of different projectiles with the HOPG target. The results for O^{7+} projectiles are displayed in figure 4.3. The detection angle θ was 90° and the incidence angle ψ was 5°. The measurements were done at projectile velocities between $v = 0.02$ a.u. and $v = 0.325$ a.u., varied in steps of 0.04 a.u., i.e. the experimental parameters are very similar to those for the N^{6+} case (fig. 4.1). Again, the spectra consist of a distribution due to projectile KLL Auger electrons (around 500 eV) as well as the target K Auger electrons between 200 eV and 280 eV. Obviously, relatively much less target Auger electrons are produced with O^{7+} as compared to N^{6+}. Also the discrete peaks superimposed on the broad KVV background are weaker.

On the other hand, the strongest effects can be expected for collision of C^{5+} with HOPG. This system is difficult to study, since projectile and target Auger electrons are expected at the same energies. However, we can avoid this problem by using fast projectiles and separate both contributions by exploiting the Doppler shift of the electrons emitted from the projectile.

Figure 4.4 shows results for $v = 0.31$ a.u. C^{5+} impact on HOPG scattered under $\psi = 5°$. The detection angle θ varies between 15° and 60°. The difference

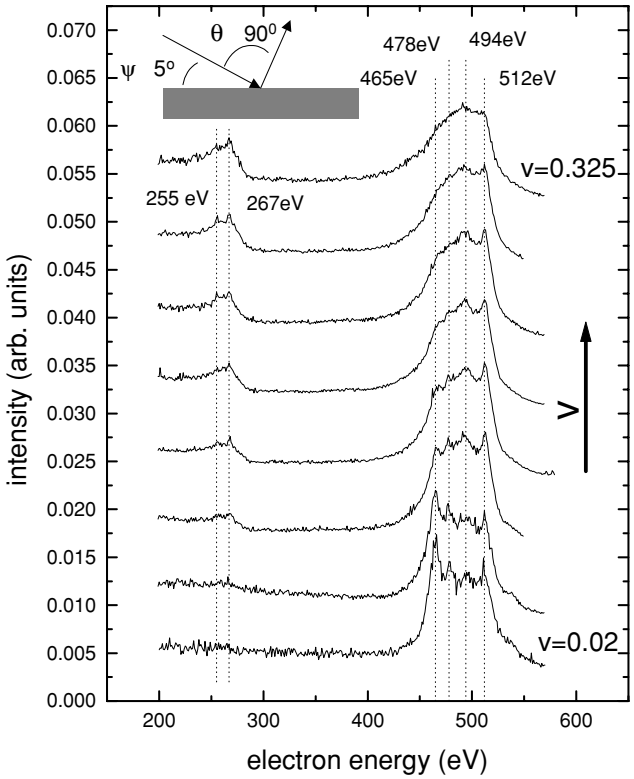

Figure 4.3: Auger spectra from O^{7+} scattered off HOPG plotted for different projectile velocities v.

in the ratio between target-Auger peak and projectile-Auger peak when going from N^{6+} and O^{7+} to C^{5+} projectiles is dramatic. For large values of θ it is hard to separate projectile and target Auger distributions, but for $\theta = 15°$ the two structures can be clearly distinguished. Even for this small detection angle, the integral over the target Auger distribution exceeds the one originating from the projectile.

This is even more surprising since we know from fig. 4.2, that at small observation angles θ the relative intensity of the target KVV Auger electrons originating from the bulk (broad structure) is strongly suppressed. Furthermore, the projectile Auger distribution clearly shows a prominent peak at 275 eV originating from the C $1s(2s^2 2p^3)$ configuration. For target Auger emission following a vacancy transfer to the C K-shell this is the expected configuration. On the other hand, it seems that the 275 eV peak is barely present in the target Auger spectra for N^{6+}, O^{7+} and C^{5+} (see figs. 4.1 to 4.4).

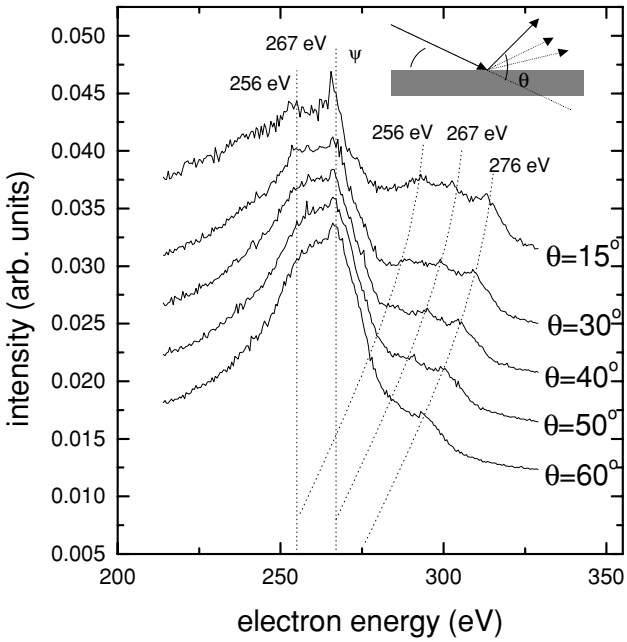

Figure 4.4: Auger spectra from C^{5+} scattered off HOPG at $v = 0.31$ a.u. plotted for different observation angles θ.

4.4 Discussion

As pointed out in the previous section, the target Auger electron distribution consists of discrete peaks superimposed on a broad background. To clarify the origin of both components, two different approaches are applicable: i) the Auger spectra can be compared to results obtained using another excitation mechanism, e.g. electrons; ii) a different carbon allotrope can be used as a target, in order to provide a different electronic structure.

Figure 4.5a displays an electron spectrum obtained by impact of 825 eV electrons on HOPG. The elastic scattering peak can be found slightly below 825 eV. About 25 eV below the elastic peak a second maximum is observed which can be attributed to electron energy loss due to excitation of a bulk plasmon. We are mainly interested in the weaker feature around 260 eV: The C KVV Auger electrons from the bulk HOPG are superimposed on a strong background of inelastically scattered electrons. The background substracted C KVV peak obtained from a 3 keV electron impact induced electron spectrum is shown in fig. 4.5b (open symbols). It is compared to the background substracted C-

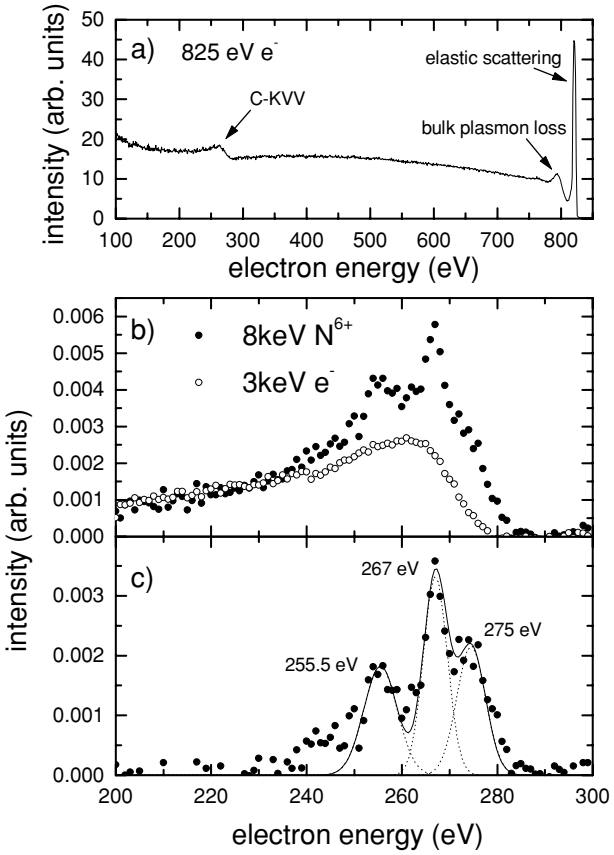

Figure 4.5: a) Raw electron spectrum from 825 eV electron impact on HOPG ($\psi = 20°, \theta = 70°$). b) Background substracted C Auger peak from 3 keV electron and 8 keV N^{6+} impact on HOPG. In c) the difference spectrum of the data in b) is displayed.

Auger peak from 8 keV N^{6+} scattered off HOPG. The difference spectrum of both distributions (fig. 4.5c) should give an idea of the electron spectrum due to above surface target Auger emission. By and large it can be described by three peaks centered at about 256 eV, 267 eV and 275 eV. The exact energetic position of the C Auger lines are compiled together with projectile C KLL Auger data from [68] in Appendix 2. The energetically highest peak at 275 eV, which is due to KLL emission from a C $1s(2s^2 2p^3)$ configuration, has not been observed in the C projectile KLL Auger spectra of the earlier study

on Si, W and Ni [68]. The appearance of the 275 eV peak here fits perfectly into the K-shell vacancy transfer picture: A K-shell electron is removed from a ground state atom within the surface, and the resulting C atom with $1s(2s^2 2p^3)$ configuration is sputtered from the surface.

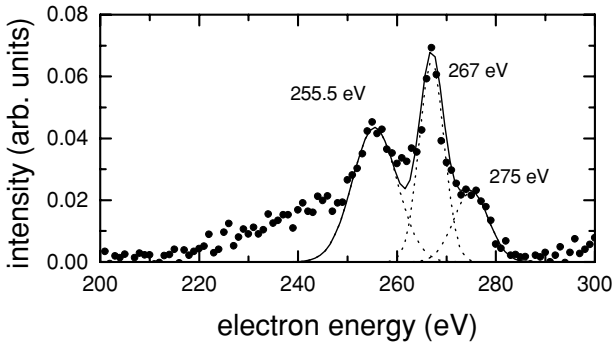

Figure 4.6: C Auger electron distribution of the $\theta = 20°$ spectrum from fig. 4.2. (N^{6+} scattering off HOPG.)

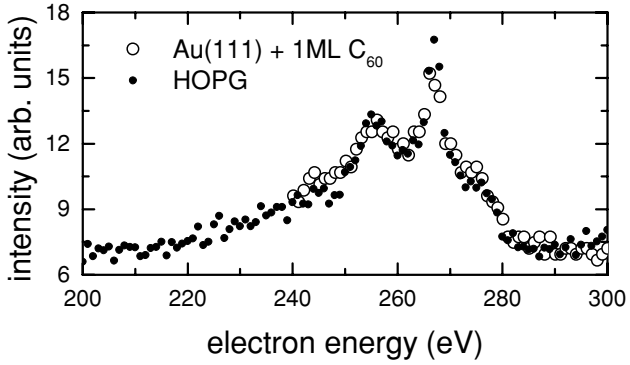

Figure 4.7: Target Auger electron spectra from N^{6+} scattered off HOPG ($\psi = 5°$, $\theta = 90°$) and a monolayer C_{60} film on Au(111) ($\psi = 5°$, $\theta = 50°$) at $v = 0.13$ a.u.

As mentioned earlier, the electrons emitted from bulk HOPG, i.e. the C KVV fraction, are suppressed for small observation angles θ. Figure 4.6 shows a zoom into the region of interest of the $\theta = 20°$ spectrum from fig. 4.2. The spectrum also mainly consists of three peaks centered at 256 eV, 267 eV and 275 eV. The peak ratios and the background differ from fig. 4.5c because of the persistence of a small fraction of KVV electrons originating from the bulk.

However, at about the same energies three C Auger peaks are also found in the (Doppler-shifted) projectile C KLL spectra (fig. 4.4). This similarity seems to indicate, that the discrete components of the target Auger distribution are due to the decay of hollow atoms above the surface moving at low velocity (negligible Doppler-shift).

In that case, the discrete components should not depend on the target electronic structure, i.e. the same results are expected for interaction of hydrogen-like ions with different carbon allotropes. In figure 4.7 target Auger spectra for $v = 0.13$ a.u. N^{6+} impact on HOPG and C_{60} covered Au(111) are shown. Obviously both spectra are basically identical. In particular, the locations of the discrete peaks are the same.

Due to the strong velocity dependence of the C KLL Auger yield, apparent from figs. 4.1, 4.2 a C K-shell ionization due to KLL electrons from the projectile can be ruled out as a dominant process: for such secondary processes, only a weak velocity dependence is expected [69].

Thus, for collisions of hydrogen-like ions with carbon targets a certain class of trajectories exists, in which a K-shell vacancy is transferred from the projectile to a surface atom which is sputtered from the surface - probably in the same collision process. Such a process is only possible under three conditions: (A) The interaction time between projectiles and surface is short in order to sustain K-shell vacancies until the collision occurs. (B) The collision energy has to be high enough to allow direct sputtering of surface atoms. (C) A vacancy transfer has to be possible.

A. Projectile-surface interaction times

The first condition is necessary for the occurrence of target Auger electron emission in general and deserves a thorough discussion. According to the classical over-the-barrier model a current of electrons starts to flow from the solid to the projectile as soon as the saddle point of their joint potential is energetically lower than the surface work function. Capture sets in at a critical distance z_0 (see eq. (2.4)) with the work function $\phi = 4.7$ eV [70] and the projectile charge state q. For $q = 5$, 6 and 7 (the hydrogen-like projectiles C^{5+}, N^{6+} and O^{7+}) the respective distances are $z_0 = 18.8$, 20.5, and 22.0 atomic units.

Below a distance z_0 the projectile is neutralized by electron capture from the surface valence band into Rydberg states. Subsequent Auger transitions then fill the L-shell. Thomaschewski *et al.* [71] found that the key parameter for the above-surface L-shell filling of N^{6+} in front of an Au(111) surface is the perpendicular component of the velocity. At closer distances two-center LVV processes take over, in which both involved electrons stem from the surface valence band. For this class of trajectories it has been shown by Limburg *et al.* [62] that the neutralization and subsequent de-excitation of hydrogen-like ions in front of various surfaces strongly depends on the frequency of close

collisions between projectile and surface atoms, i.e. on the parallel projectile velocity. The transition rates for the L Auger processes themselves are velocity independent and depend weakly on the number of L-shell electrons already present. For an LVV Auger process into the L-shell of an N-ion for instance, the transition rate is $\approx 1 \cdot 10^{15}$ s^{-1} for electron densities comparable to the graphite case ($r_s = 1.5$ a.u.) [72]. This is only one order of magnitude faster than typical KLL-Auger transition times which lie in the 10^{14}-10^{13} s^{-1} range and therefore KLL decay sets in as soon as two electrons are present in the L-shell, at a time when the projectile is still above the surface. The corresponding peak in the electron spectra for N^{6+} impact is due to a $1s(2s^2\ ^1S)\ ^2S$ configuration and can be found at 350 eV (fig. 4.1). The fact that this peak is only present for very low collision velocities already indicates, that a second velocity dependent L-shell filling process is active. Most probably for closer distances the L-shell is filled quasi resonantly in a Landau-Zener type electron transfer during close binary collisions [67]. The frequency of such collisions scales with the projectile velocity v. With increasing projectile velocity, the fast direct filling of the projectile L-shell becomes more important and KLL emission from more completely filled L-shell systems sets in. From fig. 4.1 it is obvious, that for N^{6+} scattering from HOPG even for low v emission from the filled L-shell takes place and the low energy peak never becomes as prominent as observed in collisions with metal and semiconductor targets. Above $v = 0.1$ a.u. it even completely vanishes. From this we conclude, that projectile KLL Auger emission at higher v takes place at or below the surface.

Therefore for $v > 0.1$ a.u. condition A) is clearly fulfilled. At lower v only a fraction of K-shell vacancies survives, giving rise to a drop in target Auger emission. In conclusion, the presence of the low energy projectile KLL peak might serve as a fingerprint for a situation in which no or little target Auger emission is expected.

B. Surface penetration and sputtering

To answer the second question, namely from which velocity on the projectiles penetrate the surface and/or sputter C atoms, we performed simulations based on the Binary Collision Approximation (BCA) using the MARLOWE code and time ordered cascades [37, 38]. Sputter yields as well as the surface reflectivity for scattering of N from HOPG ($\psi = 10°$ and $v = 0.02 - 0.3$ a.u.) can be found in figure 4.8.

A strong threshold effect is visible for both quantities: At about 0.05 a.u. the projectiles start to penetrate the surface and the sputtering yield increases dramatically. To compare this directly to the experimental data, we extracted the target K Auger to projectile KLL Auger ratios as a function of v for N^{6+} and O^{7+} projectiles (fig. 4.10).

Both data sets show an increase with v. In the case of N^{6+} the ratio rises

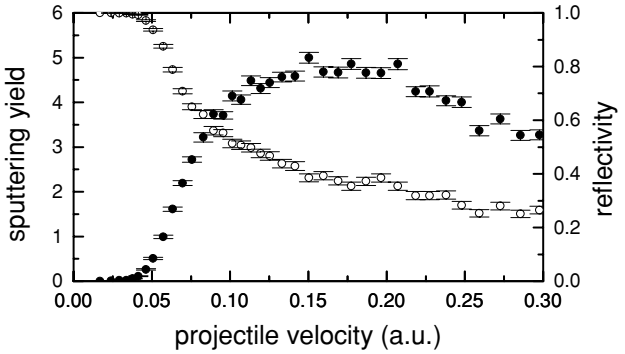

Figure 4.8: Sputtering yield (solid circles) and reflectivity (open circles) of a HOPG surface upon N impact as a function of the projectile velocity v ($\psi = 10°$).

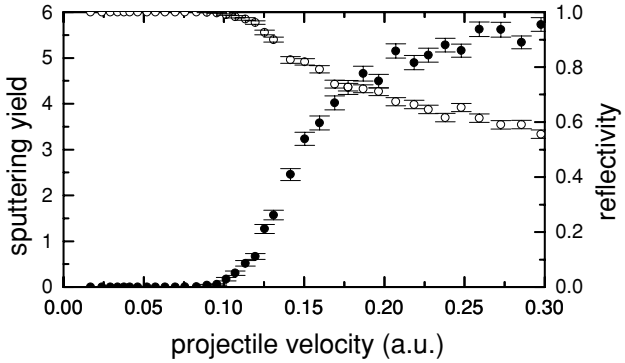

Figure 4.9: Sputtering yield (solid circles) and reflectivity (open circles) of a HOPG surface upon O impact as a function of the projectile velocity v ($\psi = 5°$).

strongly around $v = 0.05$ a.u., as expected from the simulation as well as from the experimentally observed survival probability of the K-shell vacancy, i.e. the absence of a high energy peak in the projectile KLL Auger distribution for small projectile velocities. From this data it is unclear, which one is the limiting factor for target Auger emission. The O^{7+} data in figure 4.10 have been measured with an incidence angle $\psi = 5°$, i.e. in a less destructive mode.

The results of the simulation of sputtering yield and reflectivity for O impinging on HOPG can be found in figure 4.9. Sputtering and penetration set in at $v = 0.1$ a.u. which is much higher than in the N^{6+} case. However, in the K Auger ratios from fig. 4.10 no threshold is visible at all. In particular

target Auger emission is observed well below the $v = 0.1$ a.u. threshold. On the other hand, the appearance of the low energy peak ($E = 465$ eV) in the projectile KLL Auger distribution in fig. 4.3 coincides with the vanishing of the target Auger peak thus indicating that the survival of the K-shell vacancy is the limiting factor for target Auger emission. Apparently, even for velocities lower than the threshold from fig. 4.9 imperfections of the surface may still give rise to some surface penetration and sputtering. However, the fact that the sputtering is less effective than for the N^{6+} case manifests itself in the relatively weak discrete peaks within the target Auger distribution (which we assign to KLL Auger emission from sputtered carbon).

C. K-shell vacancy transfer

From figure 4.10 it is also obvious, that the (total) relative target Auger yield is significantly higher for N^{6+} than for O^{7+}. Part of the reason is the larger ψ for the N^{6+} data, therefore fig. 4.10 also contains an N^{6+} data point measured under the same scattering geometry as the O^{7+} data ($\psi = 5°$). The relative values at $v = 0.15$ a.u. are 0.215 (N^{6+}) and 0.085 (O^{7+}) i.e. at this velocity with oxygen projectiles 60% less target Auger electrons are observed.

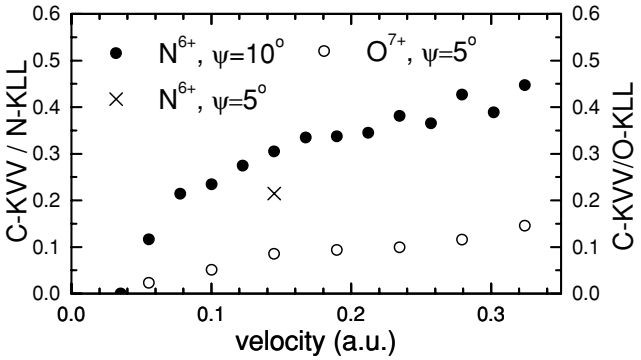

Figure 4.10: Target KVV to projectile KLL ratios versus v for N^{6+} (left axis, full circles, $\psi = 10°$) and O^{7+} (right axis, open circles, $\psi = 5°$) scattered off HOPG. The data are taken from figs. 4.1 and 4.3 and have been background substracted. The additional data point (x) at $v = 0.15$ a.u. belongs to the N^{6+} but has been measured under the same geometry as the O^{7+} ($\psi = 5°$).

The reason has to lie in the projectile dependence of the vacancy exchange mechanism. In the past, a variety of inner-shell vacancy exchange mechanisms have been proposed and used successfully. We applied the model of Schippers

et al. [67] which assumes Landau-Zener like vacancy exchange in close binary collisions. However, in that work collisions of N^{6+}, O^{7+} and Ne^{9+} ($v \approx 0.4$ a.u.) with Pt(110) were studied, where vacancy transfer between projectile K-shell and target N-shells is dominating. The level crossings occur at internuclear distances between 0.5 a.u. and 1 a.u., which can easily be reached at such high velocities. In our study the C K-shell is involved and vacancy transfer from the projectile K-shell or L-shell takes place at even smaller internuclear distances. In particular in the low projectile velocity regime these distances can hardly be reached and the resulting vacancy exchange probabilities are negligible. Only for the symmetric case of a C projectile at high v, considerable exchange probability from the projectile L-shell to the target K-shell is obtained. At $v = 0.3$ a.u. on average 5 C atoms are sputtered by each projectile, i.e. several close collisions take place, each with a considerable vacancy exchange probability. This could lead to an increased vacancy transfer probability, which could explain the experimental results obtained with C^{5+} projectiles, but not the O^{7+} and N^{6+} case. The reason for the non-applicability of the Landau-Zener approach from Schippers *et al.* [67] might lie in the semi-metallic structure of the HOPG which gives rise to a screening which differs from the metal case.

4.5 Summary

The interaction of slow ($v < 0.4$ a.u.) hydrogen-like ions with carbon surfaces leads to strong target K Auger emission. These Auger electrons partly originate from bulk or surface carbon (KVV Auger electrons). A second fraction of the carbon K Auger electrons exhibits distinct peaks, which can be identified as being due to atomic KLL transitions. Such strong target Auger emission has not been observed yet. We presented strong indications that the target KLL electrons are fingerprints of a yet undiscovered process, namely sputtering of hollow atoms from the surface.

Chapter 5

Spin-polarized surfaces

5.1 Introduction

Auger Electron Spectroscopy (AES) and Electron Capture Spectroscopy (ECS) are used to investigate whether ion-surface scattering is sensitive to spin polarization effects in surfaces. For these studies we used helium ion beams, which can be produced rather easily with high intensity. In AES, Auger spectra of doubly excited He^{2*}, formed by the He^{2+}-surface interaction, may reveal information on spin polarization effects by changes in the population balance between triplet and singlet He^{2*} states. In ECS, the degree of circular polarization of light emitted in the decay of He^{*} triplet states is used to study spin polarization effects. In this chapter our results from spin-polarized surfaces, obtained with both spectroscopy methods, are presented. Firstly, AES was used to study a Cs-covered GaAs(001) surface, for which it is known that it can be spin-polarized relatively easily by optical pumping with circularly polarized laser light (section 5.2). Secondly, a ferromagnetic Ni(110) surface was studied below and above the Curie temperature by means of AES (section 5.3). Finally, magnetically induced spin polarization of the Ni(110) surface was studied with ECS (section 5.4).

5.2 Spin polarization by optical pumping

Auger electrons of excited He^{2*} are of relatively low energy ($\sim$ 35 eV) and thus sensitive to (stray) magnetic fields. Therefore a non-magnetic, spin-polarized target is preferred. To produce such a target we used the ideas underlying spin-polarized electron sources [73, 74].

GaAs band structure

The concept is best explained via the band structure of GaAs, shown on the left side of figure 5.1. In the figure, the binding energy is plotted versus the wave number k within the first Brillouin zone, near the Γ point. Unlike metals, which have a continuous conduction band, semiconductors have a band gap E_g separating the conduction band E_c from the valence band E_v. At $T = 0$ K, in a pure (un-doped) semiconductor, the Fermi level μ is equal to the Fermi energy E_F. The position of μ can be changed by increasing the temperature and/or by doping of the semiconductor. By n-type doping μ is increased, by p-type decreased. At room temperature the Fermi level normally lies within the band gap and the conduction band is empty.

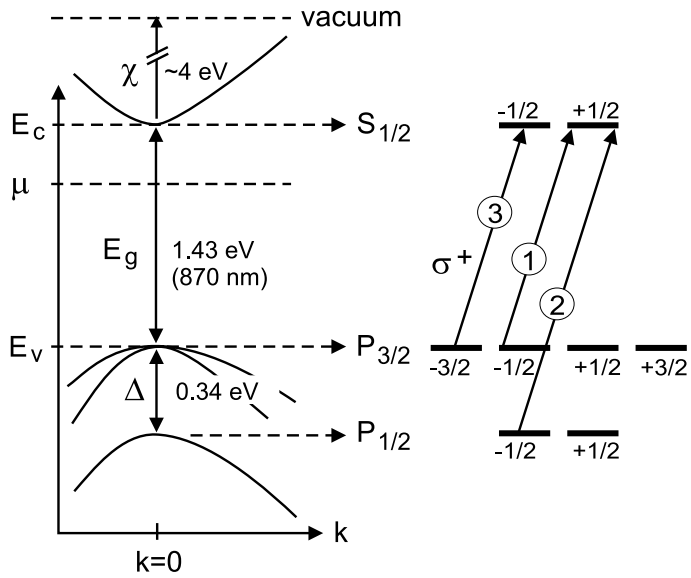

Figure 5.1: Left: GaAs band structure (Γ point). Right: Magnetic substates M_J of the corresponding band states. The encircled numbers indicate the relative transition probabilities [73].

The quantity χ (~ 4 eV) is the electron affinity, *i.e.* the energy difference between the minimum of the conduction band and the vacuum level. In GaAs, the bottom of the conduction band is separated by a band gap $E_g = 1.43$ eV ($\lambda = 870$ nm) from the top of the valence band. For GaAs the wave functions at the valence band maximum and the conduction band minimum, which is at the Γ point, have p and s symmetry, respectively. Due to the spin-orbit interaction the sixfold degenerate p band is split into a fourfold degenerate $P_{3/2}$ state and

a twofold degenerate $P_{1/2}$ state, separated by $\Delta = 0.34$ eV [73].

Optical pumping

Electronic spin polarization can be obtained by optical pumping with circularly polarized light, thereby inducing transitions between the $P_{3/2}$ state (valence band) and the $S_{1/2}$ state (conduction band). In order to selectively pump from only the $P_{3/2}$ state the photon energy $E = hc/\lambda$ should be higher than the band gap E_g, but not so high as to promote electrons from the $P_{1/2}$ state too. In our experiments a 30 mW GaAlAs diode laser, producing 1.58 eV ($\lambda = 788$ nm) photons, was used for the optical pumping. Circularly polarized light was created by a linear polarizer and a quarter wave plate.

Electronic transitions between initial $|\psi_i\rangle$ and final $|\psi_f\rangle$ states have to obey the selection rules for optical dipole transitions, *i.e.* $\Delta L = \pm 1$ and $\Delta M_L = 0, \pm 1$. In these transitions the spin is not affected, thus $\Delta M_J = \Delta M_L$. Transitions with $\Delta M_J = 0$ are induced by linearly polarized light (π light) and transitions with $\Delta M_J = \pm 1$ by circularly polarized light (σ light). The transition probability for a transition from state $|\psi_i\rangle$ to state $|\psi_f\rangle$ is given by $|\langle\psi_f|H_{fi}|\psi_i\rangle|^2$, where H_{fi} represents the interaction Hamiltonian [73]. On the right side of figure 5.1 the magnetic substates M_J of the relevant band states are shown. The arrows indicate the transitions from the valence band substates to the conduction band substates, which can be induced by σ^+ light. The encircled numbers in the arrows are the corresponding relative transition probabilities [73].

Spin-polarized surface electrons

To have the spin-polarized electrons available for capture by the He^{2+} projectile ions, further tricks need to be played in order to prevent the spin-polarized electrons from disappearing into the bulk material. By adsorbing a small amount of Cs atoms onto the clean GaAs surface, the electron affinity χ can be reduced to almost zero. When a Cs atom is adsorbed on the GaAs, it gives up an electron to the GaAs because the ionization potential of Cs is much lower than the work function of GaAs [75]. The adsorbed Cs atom can be thought of as being resonantly ionized. Evaporating a small amount (~ 0.5 ML) of Cs onto the GaAs surface leads to the formation of a dipole layer, which effectively reduces the electron affinity near the surface. Electrons in the conduction band are therefore attracted to the surface and almost set free.

In spin-polarized electron sources, the optically pumped electrons are extracted from the cesiated GaAs surface by an applied electrostatic field. Electrons pumped to the $S_{1/2}$ state are thus effectively removed before they can decay back to the $P_{3/2}$ state. In principle, the spin polarization of the $S_{1/2}$

state is then given by the relative transition probabilities. The spin polarization is defined as the relative difference between the number of spin-up $N_\uparrow$ and spin-down $N_\downarrow$ electrons, *i.e.*

$$P = \frac{N_\uparrow - N_\downarrow}{N_\uparrow + N_\downarrow}$$

The maximum spin polarization of the $S_{1/2}$ state, determined by the corresponding relative transition probabilities from figure 5.1, is then $P = (3 - 1)/(3 + 1) = 50\%$. Electron sources producing a spin polarization of 40-50% have already been reported [73, 74].

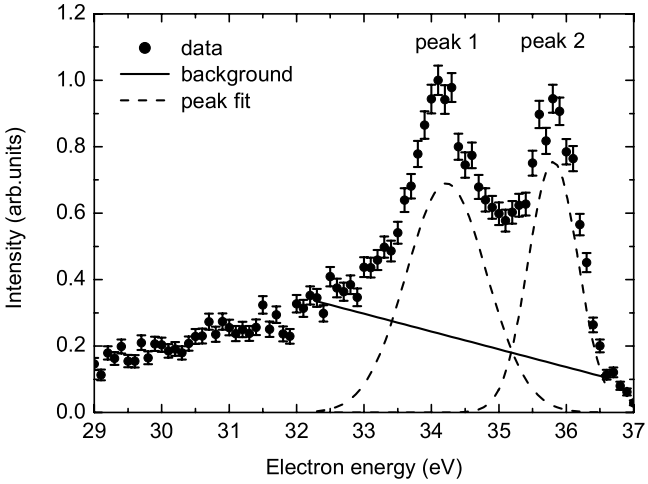

Figure 5.2: Helium Auger spectrum taken from a clean GaAs(001) surface. The background and the fits to the two peaks are also indicated.

Results

To investigate whether spin polarization effects can be studied by means of Auger electron spectroscopy, we used the recipe of Cs adsorption and optical pumping to produce a spin-polarized target. To do so, Auger spectra as a function of Cs coverage were recorded for three cases: (1) laser off, (2) laser on and linearly polarized light (π), and (3) laser on and circularly polarized light (σ^+). The Cs was evaporated from a Cs dispenser placed about 2 cm in front of the GaAs surface.

To see whether the surface can be 'activated' we biased the target. It was found that electron emission started roughly after 2 minutes of Cs evaporation at a dispenser current of 5 A, but only with the laser on. For longer evaporation times the electron emission decayed almost exponentially. This implies that the Cs coverage is ~ 0.5 ML after 2 min of evaporation because at this coverage the work function of the Cs/GaAs system reaches its minimum value [76, 77]. It is thus around this coverage that spin polarization effects may be expected in the Auger spectra. By means of Low Energy Ion Scattering (LEIS) measurements we determined that after about 1.4 hours this initial Cs coverage (~ 0.5 ML) was removed from the surface due to sputtering by the He^{2+} ion beam. The LEIS measurements also indicated that the Cs coverage changed linearly with time. Thus by taking Auger spectra as a function of time after evaporation, we obtained information as a function of decreasing Cs coverage. (See figure 5.4 for these spectra.)

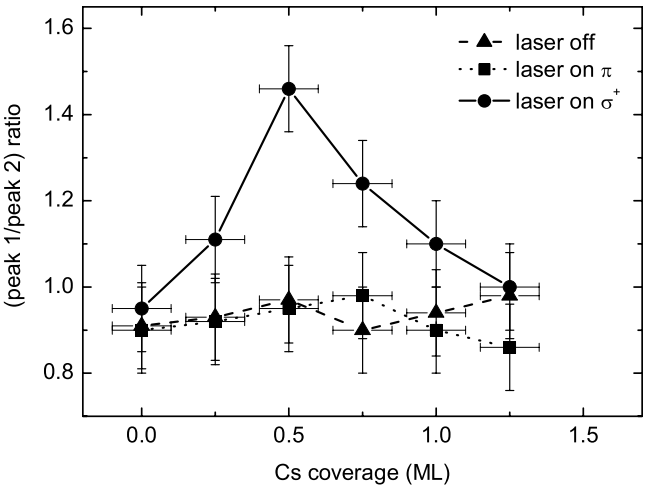

Figure 5.3: The ratio (peak 1/peak 2) is plotted as a function of the Cs coverage on the GaAs surface.

Surface spin polarization effects should be determined from the difference in the Auger spectra between case (2) and (3). Optical pumping with π light leads to equal numbers of spin-up and spin-down electrons in the conduction band. This is most easily understood by realizing that addition of σ^+ and σ^- light leads to π light. Only optical pumping with one type of σ light can lead to a net spin polarization of the conduction band. Spin polarization of the electrons at the surface should increase the probability for neutralization into

He^{2*} triplet states. In turn, this should lead to an enhanced intensity of the corresponding Auger peak.

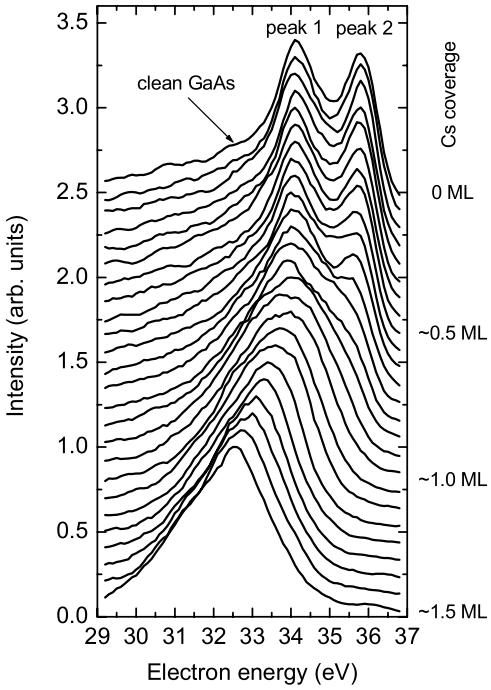

Figure 5.4: Helium Auger spectra from Cs/GaAs plotted for different Cs coverages. (laser off)

Figure 5.2 shows an Auger spectrum obtained from a clean GaAs surface. The energy of the He^{2+} ions was $E_{kin} = 500$ eV, the incidence and detection angles were $\psi = 10°$ and $\theta = 90°$, respectively. The two peaks in the spectrum are known to be due to autoionization (AI) of four doubly excited $He^{2*}(2l2l')$ states, formed by resonant neutralization and decaying above the surface on the incoming trajectory [65]. Peak 1 at 34.3 eV is due to AI from the $(2s^2)$ ^{1}S singlet state and the $(2s2p)$ ^{3}P triplet state. Peak 2 at 35.9 eV originates from the $(2p^2)$ ^{1}D and $(2s2p)$ ^{1}P singlet states. Due to the small differences in their binding energies and due to level broadening close to the surface, the four states emerge as two strong peaks in the Auger spectra.

In figure 5.2 the data analysis procedure is indicated too. From the raw data (dots) a linear background is subtracted (solid line) and the resulting spectrum is fitted by two Gaussian-shaped peaks (dashed lines). The integral of each fitted peak corresponds to the sum of the intensities of the underlying

peaks. Spin polarization should enhance the population of the triplet state with respect to the singlet states. Therefore, the intensity of the $(2s2p)$ ^{3}P component in peak 1 should increase relative to the intensities of the three singlet components. The ratio of peak 1 and peak 2 might then serve as a 'measure' of surface spin polarization effects.

In figure 5.3 the (peak 1/peak 2) ratio is plotted versus the Cs coverage, for the three different cases: (1) laser off (up-triangles), (2) laser on and linearly polarized light (π, squares), and (3) laser on and circularly polarized light (σ^+, circles). The lines connecting the data points serve to guide the eye. From figure 5.3 it can be seen that only when σ^+ light is used, the peak ratio is enhanced and exhibits a maximum value around a Cs coverage of about 0.5 ML. At this coverage the work function is minimum and the optically pumped and polarized conduction band electrons are expected to be located at the surface. For the other two cases the peak ratio is almost constant as a function of Cs coverage. Based on these first results, it seems that AES might indeed be suited for studies on spin-polarized surfaces.

A critical note is still in place here. In figure 5.2 the background subtraction and peak fitting procedure is indicated. In case of a clean GaAs surface, the clear spectrum allows for a reasonable estimate of the background as well as a good fit to the peaks. However, as can be seen in the Auger spectra of figure 5.4, for higher Cs coverage the spectra are more difficult to analyze. For observation of spin polarization effects the Cs coverage is about 0.5 ML and there the analysis procedure is still applicable.

5.3 Temperature dependent spin polarization

Another test system for observing spin effects is a ferromagnetic target such as *e.g.* Ni(110). Although the target exhibits no macroscopic magnetization at room temperature, on the microscopic level and below the Curie tempera-ture T_C the electron spins are magnetically ordered within domains. The ferromagnetic ordering (or spin alignment) can be destroyed by increasing the temperature to the Curie temperature. We have chosen a Ni(110) target for our experiments on temperature dependent spin polarization, because its surface is relatively easy to prepare and because the Curie temperature is relatively low ($T_C = 354°C$) and thus easily reached.

AES was used to observe changes in the spin polarization as a function of the temperature. The results are shown in figure 5.5. All four spectra are taken at the same scattering conditions: $E_{kin} = 100$ eV, $\psi = 15°$ and $\theta = 90°$. The Auger spectrum taken at room temperature ($T = 20°C$) is shown at the bottom. It can be seen that the intensities of peak 1 and peak 2 are about the same. As the temperature is increased, $T = 200°C$ and $T = 300°C$, the intensity of peak 1 becomes slightly less. A loss in ferromagnetic

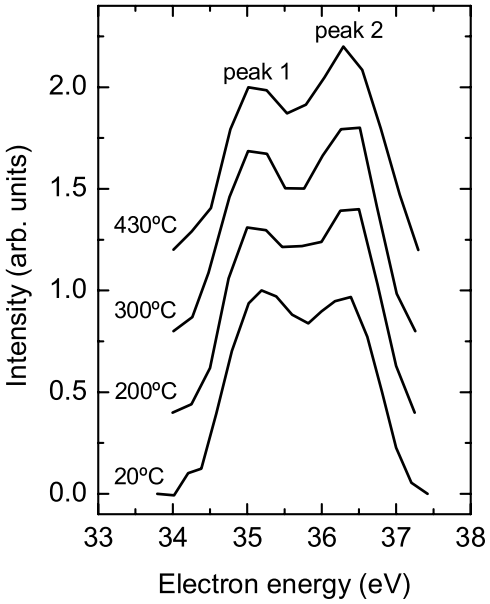

Figure 5.5: Helium Auger spectra from Ni(110) plotted for four different temperatures. The normalized spectra have been given an offset for clarity.

ordering would manifest itself in a reduced probability of neutralization into the $He^{2*}(2s2p)\ ^3P$ triplet state and thus a reduced intensity of peak 1. The upper spectrum, taken at $T = 430°C$ which is well above T_C, shows an even clearer reduction of the triplet peak intensity. This spectrum should represent an Auger spectrum obtained from a surface with a completely random distribution of electron spins. Ergo, the experimental results obtained with AES are at least qualitatively consistent with the temperature induced changes in magnetic ordering of electron spins.

Unfortunately, subsequent attempts of probing spin polarization effects induced by an applied magnetic field were less successful. In these experiments, the sample was clamped in a soft iron yoke (section 3.3.5). However, due to stray magnetic fields, it was no longer possible to detect the helium Auger electrons because of their low kinetic energies ($\sim$ 35 eV). Therefore Electron Capture Spectroscopy (ECS) was applied to observe magnetically induced spin polarization effects.

5.4 Magnetically induced spin polarization

The principle of ECS [19], *i.e.* polarization analysis of the fluorescence from the decaying excited projectiles, was treated in chapter 3. For first explorative experiments on surface magnetism, the $(1s3d)\ ^3\mathrm{D} \rightarrow (1s2p)\ ^3\mathrm{P}$ transition in excited helium was chosen. This line, from now on abbreviated as ^{3}D-line, has a wavelength of $\lambda = 587.56$ nm. The same line has been used in earlier experiments on a non-magnetic Ni(110) surface [78, 79, 80].

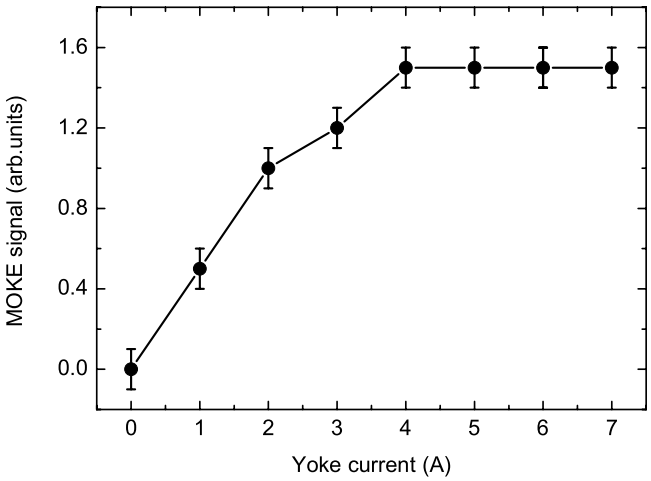

Figure 5.6: MOKE signal versus yoke current. The Ni(110) target reached saturation magnetization at 4A.

In our ECS experiments the magnetic field is applied along the easy axis of magnetization, *i.e.* the $[1\bar{1}1]$ direction, which is perpendicular to the ion beam direction. The ECS geometry is indicated in figure 3.9 and figure 5.8a. The Ni(110) target was demagnetized by an oscillating current with an amplitude exponentially decreasing in time. Zero yoke current (0 A), and thus no magnetic field, corresponds to a demagnetized target. Target magnetization was checked by the Magneto-Optical Kerr Effect (MOKE). In figure 5.6 the MOKE signal is plotted as a function of the yoke current. Saturation magnetization of the Ni(110) target was reached at a yoke current of 4 A.

Before discussing the ECS results, it should be indicated why the degree of circular polarization is linked to the alignment of surface electron spins. This correlation is best explained in three successive steps. Firstly, for the singlet ^{1}D-line, the link between the polarization of light and the distribution over the magnetic substates is made. Secondly, the preferential orientation of the orbital

angular momentum by the scattering conditions is discussed by two models. Finally, the influence of aligning the surface electron spins on the distribution over the magnetic substates is explained for the triplet ^{3}D-line.

The singlet ^{1}D line

The singlet $(1s3d)^1\mathrm{D} \rightarrow (1s2p)^1\mathrm{P}$ transition or ^{1}D-line in helium has a wavelength of $\lambda = 667.82$ nm. The initial $(1s3d)^1$D state is populated during the $\mathrm{He}^+(1s)$-surface interaction by electron capture of a surface electron e_2 and decays via photoemission to the final $(1s2p)^1$P state. The captured surface electron e_2 with spin s_2, will orbit the helium core with orbital angular momentum l_2. The initial helium electron e_1 has s_1 and l_1.

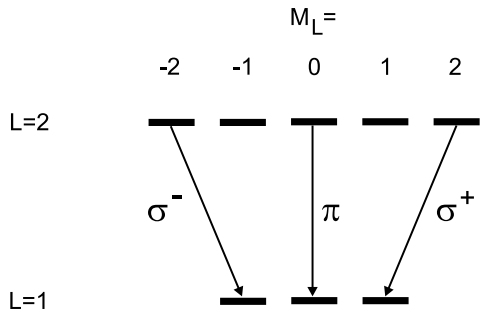

Figure 5.7: The relevant LM_L states for the $(1s3d)$ ^{1}D $\rightarrow$ $(1s2p)$ ^{1}P transition (667.82 nm). The types of polarization are also indicated.

The initial and final state configurations are given by their spectroscopic notation $^{2S+1}L_J$. The initial ^{1}D state has $l_1 = 0$ and $l_2 = 2$, so $L = l_1 + l_2 = 2$ and M_L varies between -2 and $+2$. The selection rules for optical dipole transitions are $\Delta L = \pm 1$ and $\Delta M_L = 0, \pm 1$, thus the final ^{1}P state has $L = 1$ and $M_L = -1, 0$ or $+1$. Final and initial states are both singlet $S = 0$ states thus the spin can be discarded. Therefore, $\vec{J} = \vec{L}$ and $M_J = M_L$, *i.e.* the state can be specified by LM_L. Figure 5.7 shows the relevant LM_L states for the ^{1}D-line. Some examples of optical transitions leading to the emission of linearly polarized light (π light) and circularly polarized light ($\sigma^{\pm}$ light) are also indicated. (For the definition of $\sigma^{\pm}$ see *e.g.* [47]).

If all initial magnetic substates are equally populated, the emitted light is un-polarized. Any distribution non-symmetric around $M_L = 0$ leads to the emission of elliptically polarized light. For example, if only $M_L = -2$ substates are populated, pure circularly polarized light (σ^-) will be emitted. If $I(\sigma^+)$ and $I(\sigma^-)$ are the light intensities of the corresponding optical transitions, the

relative degree of circular polarization S/I is given by

$$S/I = \frac{I(\sigma^-) - I(\sigma^+)}{I(\sigma^-) + I(\sigma^+)} \tag{5.1}$$

The quantity S/I is thus related to an asymmetry in the distribution over the magnetic substates M_L.

Model interpretations

Emission of circularly polarized light with a considerable degree of polarization has been reported for the ^{1}D-line, see *e.g.* [81] and [20]. Thus it is known that the distribution over the ^{1}D magnetic substates is not centered around $M_L = 0$. This implies that there is a net orientation of the total orbital angular momentum $\vec{L}$ induced by the scattering conditions.

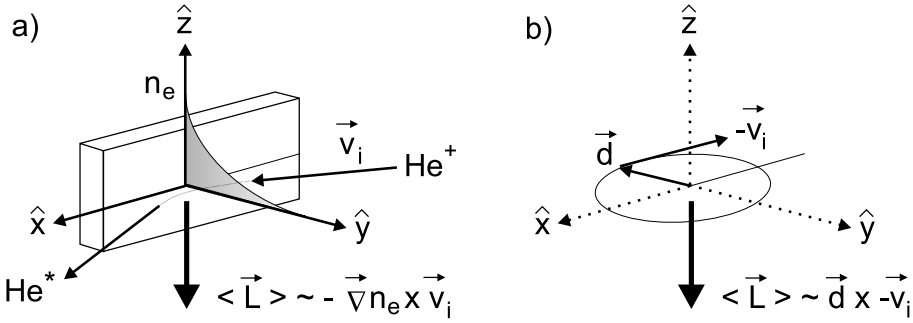

Figure 5.8: a) Preferential orientation of $\vec{L}$ due to friction with the electron gas [82], and b) according to 'classical' capture of an electron [83].

Such a preferential orientation can be explained by the *density gradient model* [82]. In this model, the ion experiences an asymmetry in the friction force due to the gradient of the electron density outside the surface, which causes the ion's electrons to rotate. In figure 5.8a the scattering geometry and the electron density n_e are indicated. The gradient $\vec{\nabla} n_e$ points in the $-\hat{y}$ direction, the ion velocity $\vec{v}_i$ in the $+\hat{x}$ direction. According to the density gradient model, the net angular momentum is then oriented as $< \vec{L} > \sim -\vec{\nabla} n_e \times \vec{v}_i$, *i.e.* along the $-\hat{z}$ direction.

The same preference is found if the neutralization is described as in ion-atom collisions [83]. It can then be argued that if the electron e_2 is transferred to the ion at an internuclear distance $\vec{d}$, its classical orbital angular momentum $\vec{L}$ is proportional to $\vec{d} \times -\vec{v}_i$, with $\vec{v}_i$ the ion velocity. The minus sign occurs because

in the ion reference frame the electron moves in the $-\vec{v}$ direction. Within the scattering geometry of our ECS experiment, the captured electron would have $\vec{l_2}$, and thus $\vec{L}$, oriented in the $-\hat{z}$ direction, as depicted in figure 5.8b.

An orientation of $\vec{L}$ along the $-\hat{z}$ direction implies that $\langle M_L \rangle < 0$, since we have $L_z = \hbar M_L$. If on average mainly substates with $M_L < 0$ are populated, more σ^- light than σ^+ light is emitted. The measured light intensity will have a high degree of circular polarization with $S/I \approx 30\%$. This is in accordance with previous experiments on (de-)magnetized Fe(110) surfaces [19, 81, 20]. It can now be concluded that S/I is related to the distribution over the magnetic substates. The second step is to describe the influence of the surface electron spin s_2 on the M_L distribution. This is best explained via the $(1s3d)$ ^{3}D$\rightarrow$ $(1s2p)$ ^{3}P transition, or ^{3}D-line, which has a wavelength of $\lambda = 587.56$ nm.

The triplet ^{3}D line

Firstly, it is emphasized that the spin s_2 of the surface electron e_2 is conserved during the electron capture and during the decay. The spin s_1 of the initial electron is always randomly distributed and can have either $m_{s1} = -1/2$ or $+1/2$. The alignment of s_2 depends on the ordering of the electron spins in the surface. Ideally, m_{s2} can be chosen to be $-1/2$ or $+1/2$ by magnetizing the surface for example.

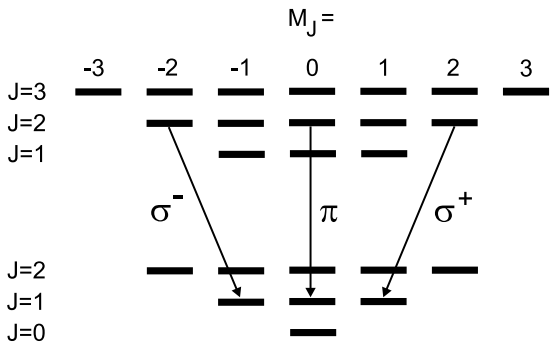

Figure 5.9: The relevant JM_J states for the $(1s3d)$ ^{3}D $\rightarrow$ $(1s2p)$ ^{3}P transition (587.56 nm) and the three types of polarization.

The initial $(1s3d)^3$D state has $L = 2$ and M_L varies between -2 and $+2$. A triplet state has additionally $S = s_1 + s_2 = 1$ and $M_S = -1, 0, +1$. By spin-orbit coupling the total angular momentum is $\vec{J} = \vec{L} + \vec{S}$. In this case J can be 1,2 or 3. The magnetic substate $M_J = M_L + M_S$ can vary between $-J$ and $+J$. The spin is not affected by the decay, *i.e.* $\Delta S = 0$, thus only $\Delta J = \pm 1$ and $\Delta M_J = 0, \pm 1$ transitions are allowed. The final $(1s2p)^3$P state

has therefore $L = 1$ and M_L varies between -1 and $+1$. The total angular momentum J can now be 0,1 or 2 and the M_J can vary between $-J$ and $+J$. It is clear that the states must now be specified by JM_J. Figure 5.9 shows the relevant JM_J states for the ^{3}D-line. The three types of polarized light are also indicated.

The way the distribution is changed by spin polarization of target electrons can be indicated by the following example. If there is a preferential orientation of $\vec{L}$, say $M_L = -2$, then the possible M_J values are given by $M_J = M_L + M_S = -2 + M_S$. For the triplet $S = 1$ state, M_J can then be $-3, -2$ or -1. The total magnetic substate M_S can be described in terms of the individual spin components m_s and is given by $M_S = m_{s1} + m_{s2}$. If the spin of e_2 is fixed at $m_{s2} = +1/2$ and e_1 is random, M_S can be $0, +1$ and M_J can be -2 or -1. But when $m_{s2} = -1/2$, M_S can be $-1, 0$ and M_J can be -3 or -2. Thus by aligning the spin of the surface electron, *e.g.* by an applied magnetic field, the distribution can be shifted towards lower or higher M_J substates. Higher M_J values increase the degree of circular polarization S/I, while lower values decrease S/I.

The interaction energy V between an electron's magnetic moment $\vec{\mu}_s = -g_s \mu_B \vec{s}/\hbar$ and an applied magnetic field $\vec{B}$ is given by $V = -\vec{\mu}_s \cdot \vec{B}$ [47]. For the $\hat{z}$-component of the interaction one obtains $V_z = g_s m_s \mu_B B_z$, with $g_s = 2$, $m_s = \pm 1/2$ and μ_B the Bohr magneton. The spin $\vec{s}$ will thus align anti-parallel to an applied magnetic field $\vec{B}$, since this requires minimum energy.

If B_z is applied in the $+\hat{z}$ direction, m_{s2} will align anti-parallel to B_z and we have $m_{s2} = -1/2$. If we have $M_L = -2$, m_{s2} and M_L are aligned parallel. The possible M_J values are then -3 and -2 and the distribution is shifted to higher negative M_J values. Ergo, a magnetic field in the $+\hat{z}$ direction will shift the M_J distribution to the left, $I(\sigma^-)$ is increased and S/I becomes more positive. Vice versa, a magnetic field applied in the $-\hat{z}$ direction will align m_{s2} anti-parallel to M_L. In that case the M_J distribution is shifted to the right and S/I is reduced.

The net effect of aligning m_{s2} on S/I depends on the magnitude of M_L. The strongest effect is obtained when $M_L = 0$, because then a change from $m_{s2} = -1/2$ to $+1/2$ will ideally change de degree of polarization from $S/I > 0$ to $S/I < 0$. For higher values of M_L, changes in m_{s2} will obviously have a smaller effect on S/I (see *e.g.* [84]). For the ^{3}D-line it can thus be expected that the changes in S/I, induced by a reversal of the applied magnetic field, may not be symmetric with respect to the results for a demagnetized surface with random spins.

ECS results for Ni(110)

Figure 5.10 shows an ECS spectrum obtained for a demagnetized Ni(110) target. The light intensity was measured with PDS-V in the $+\hat{z}$ direction, *i.e.* parallel to the surface and the magnetic field, and perpendicular to the scattering plane XY. This geometry allows for the detection of circularly polarized light. The measured light intensity of the ^{3}D-line is plotted as a function of the rotation angle of the $\lambda/4$-plate, which rotates from 0 to 360°. Since the data is symmetric about 180°, only half the rotation range is shown. The two Stokes parameters I and S are also indicated. The solid line is a fit of equation (3.15) to the data.

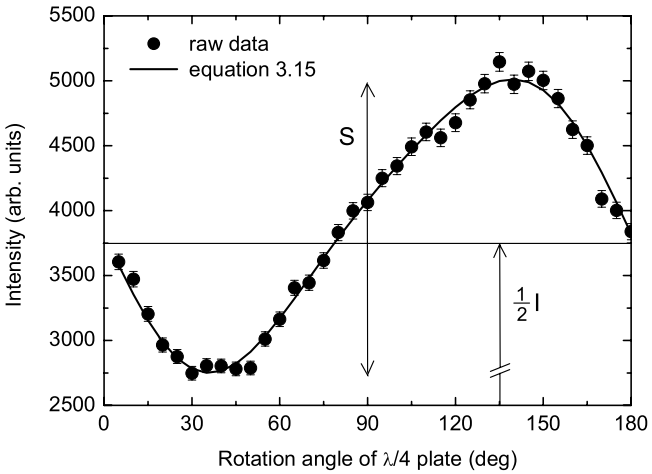

Figure 5.10: ECS spectrum of a demagnetized Ni(110) surface. ($E_{kin} = 20$ keV, $\psi = 5°$, ^{3}D-line)

The use of a perfect $\lambda/4$-wave plate implies $\Delta = 90°$. Substitution of this value for Δ simplifies equation (3.15) to

$$I^*(\beta, 90) = \frac{1}{2}I + \frac{1}{2}M\cos^2(2\beta) + \frac{1}{4}C\sin(4\beta) - \frac{1}{2}S\sin(2\beta) \qquad (5.2)$$

From equation (5.2) it can be seen that S/I can be obtained from a single measurement. At the angles $\beta = 45°$ and 135°, equation (5.2) only depends on the Stokes parameter S, and one obtains respectively

$$I^*(45, 90) = \frac{1}{2}I - \frac{1}{2}S \qquad (5.3)$$

$$I^*(135, 90) = \frac{1}{2}I + \frac{1}{2}S \qquad (5.4)$$

The relative degree of circular polarization S/I is then given by

$$S/I = \frac{I^*(135,90) - I^*(45,90)}{I^*(135,90) + I^*(45,90)} \tag{5.5}$$

Equation (5.5) holds for a perfect $\lambda/4$-wave plate with $\Delta = 90°$. The retardation angle Δ for our waveplate was determined by taking ECS spectra (see fig. 5.10) for highly M-polarized light. For our waveplate a value of $\Delta = 89 \pm 1$ for $\lambda = 587.56$ nm was obtained.

For a more precise value of S/I, equation (3.15) must be fit to the data in figure 5.10. From the fit the following relative Stokes parameters are obtained: $M/I = (2.0 \pm 1.0)\%$, $C/I = (-7.7 \pm 1.0)\%$ and $S/I = (28.3 \pm 0.5)\%$. The value obtained for S/I is consistent with previous measurements on Ni(110) [80]. From the small M and C values it is clear that the light was elliptically polarized, but with a high degree of circular polarization S.

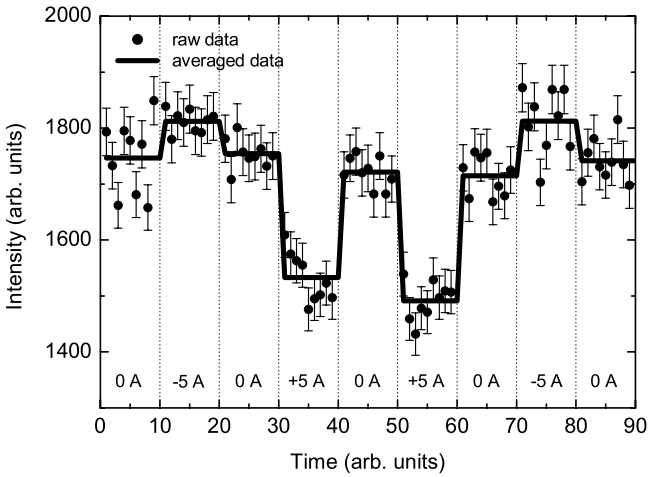

Figure 5.11: Light intensity of the ^{3}D-line plotted versus time for switching of the electron spins. ($E_{kin} = 12$ keV, $\psi = 2.5°$)

According to equation (5.3) and (5.4), changes in S/I due to an applied magnetic field can be directly observed at $\beta = 45, 135°$. Intensity measurements with the $\lambda/4$-plate fixed at 135° were done for three extreme cases: (1) no alignment (0 A), (2) spins aligned in $-\hat{z}$ direction (-5 A), and (3) spins aligned in $+\hat{z}$ direction (+5 A). The results are shown in figure 5.11, were the intensity of the ^{3}D-line is plotted as a function of time. The time axis is divided in

periods of 100 s (dotted lines), *i.e.* 10 s per data point and 10 points in each period. The value of the applied magnetic field, indicated in each period, was kept constant during the period. The dots represent the raw data, the solid line represents the average intensity during each period and serves to guide the eye.

From figure 5.11 it can be seen that the light intensity directly follows the (hard) changes due to the spin reversal. Alignment of the spins in the $-\hat{z}$ direction (-5 A) leads to a small increase in the light intensity. This is consistent with our interpretation, which was discussed above. Aligning the surface electron spins m_{s2} parallel to M_L, *i.e.* in the $-\hat{z}$ direction, leads to an increase in S/I. Vice versa, aligning the spins in the $+\hat{z}$ direction (+5 A) leads to a decrease of the intensity. Furthermore, a clear asymmetry with respect to the (0 A) case between the spin directions can be seen. As mentioned above, the asymmetry is due to the spin-orbit coupling. The effect of aligning m_{s2} is most pronounced when the M_L distribution is centered around $M_L = 0$ [84]. For higher M_L substates the effect of aligning m_{s2} becomes less.

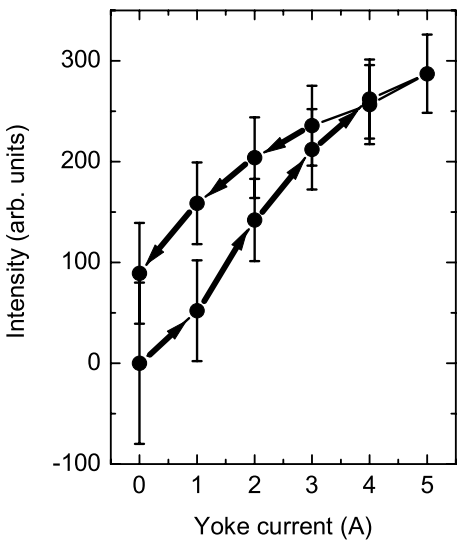

Figure 5.12: Hysteresis plot: light intensity difference versus yoke current (magnetic field).

The same effects were observed when the magnetic field was varied more smoothly. From these results a *hysteresis* plot is produced. As an example, the results for spin alignment in the $+\hat{z}$ direction are shown in figure 5.12. The intensity difference $I^*(+A) - I^*(0)$ is plotted versus the yoke current. The

arrows between the data points indicate how the loop was traversed. Note that the curve does not retrace itself, *i.e.* hysteresis effects occur. At the highest magnetic fields the intensity seems to saturate, which is consistent with our MOKE measurement (fig. 5.6).

It can be concluded that these first results are in accordance with the current interpretation. The sign and magnitude of S/I and the observed asymmetry are in line with our expectations. Ergo, it seems that changes in S/I can be induced by changing the direction of surface electrons spins. ECS may thus have the potential of probing magnetic ordering effects in surfaces or thin films.

Chapter 6

Atomic features of Auger spectra

6.1 Introduction

In chapter 5, Auger spectra from collisions of He^{2+} on spin-polarized surfaces were presented. The spin effects were observed via changes in the ratio of the two prominent peaks in the Auger spectra. These peaks are due to AutoIonization (AI) of doubly excited ($2l2l'$) states in neutral helium. In the following, the two peaks will be referred to as 'peak 1' ($\sim$34.5 eV) and 'peak 2' ($\sim$36.0 eV). Each of these peaks may originate from two doubly excited states, *i.e.* peak 1: ($2s^2$) ^{1}S and ($2s2p$) ^{3}P, and peak 2: ($2p^2$) ^{1}D and ($2s2p$) ^{1}P.

In early discussions of these atomic features the ($2s2p$) ^{3}P and the ($2s2p$) ^{1}P states were neglected because of their much longer life times as compared to the ($2s^2$) ^{1}S and ($2p^2$) ^{1}D states [85]. The fact that we seem to observe changes in the ratio of peak 1 and peak 2, induced by spin polarization of surface electrons, implies that the ($2s2p$) ^{3}P triplet state cannot be neglected.

Although neutralization and decay of the projectiles is qualitatively understood [86, 87, 65], we want to quantify which states contribute most strongly to the atomic features in the Auger spectra, given a certain ion-surface system. Specifically, we want to know how the populations of the states involved are influenced by the projectile velocity, the surface density of states of the target, and above all spin polarization effects.

First the electronic structure of helium is presented (section 6.2). The discussion on the decay processes is started by the introduction of the 'free atom model' in section 6.3, which results are compared with experimental data in section 6.4. In section 6.4 it is also made clear that Resonant Ionization (RI) and the projectile's parallel velocity ($v_\parallel$) have to be included in order to

improve the description of the spectral features. At the end of this chapter the discussion is extended to spin ordering effects.

6.2 Helium electronic structure

In an AI process, a doubly excited helium projectile decays to a lower lying ionic state under the emission of an Auger electron into the vacuum. The relevant doubly excited helium states are listed in table 6.1. Their corresponding properties will be discussed below.

state	$-E_B$ eV	E_i eV	E_k eV	$\Gamma_{AI}\cdot 10^{14}$ Hz	g_i
$(2s^2)\ ^1$S	21.13	7.53	33.29	2.10	1
$(2s2p)\ ^3$P	20.69	7.09	33.73	0.23	9
$(2p^2)\ ^3$P	19.33	5.73	-	0	9
$(2p^2)\ ^1$D	19.12	5.52	35.30	1.10	5
$(2s2p)\ ^1$P	18.88	5.28	35.54	0.64	3
$(2p^2)\ ^1$S	16.86	3.26	37.56	$\ll 0.1$	1

Table 6.1: $He^{2*}(2l2l')$ states, energies [59], AI rates [88] and statistical weights.

The kinetic energy E_k of the Auger electron is given by the difference in binding energy E_B between the initial $He^{2*}(2l2l')$ state and the final $He^+(1s)$ state. Binding energies of the initial states are listed in table 6.1. The final $He^+(1s)$ ionic ground state has a binding energy of -54.42 eV [59].

The ionization energies E_i of the doubly excited states are also listed in table 6.1. The ionization energy E_i is given by the difference in binding energy between the initial $He^{2*}(2l2l')$ state and the final $He^+(2l)$ state, which has a binding energy of -13.60 eV [59].

The AI rates listed in table 6.1 belong to free atoms in the gas phase [88]. The AI rate for the $(2p^2)\ ^3$P state is zero because the decay is forbidden. Also the rate for the $(2p^2)\ ^1$S state is very small. These states will therefore not contribute to the atomic features in the Auger spectra. It can be seen that the rates for the $(2s^2)\ ^1$S and $(2p^2)\ ^1$D states are high as compared to the $(2s2p)\ ^3$P state.

The last column in table 6.1 represents the statistical weight g_i of the corresponding $He^{2*}(2l2l')$ state. The statistical weight is determined by the spin S_i and the orbital angular momentum L_i, *i.e.* $g_i = (2S_i + 1)(2L_i + 1)$.

6.3 The free atom model

The effects of the AI processes on the time-dependent population of the excited states is best illustrated by a simple 'free atom model'. In this simple picture, the $(2l2l')$ states are allowed to decay in time by AI just like excited free atoms. Radiative decay can be neglected because these rates are much slower (chapter 2). It is assumed that the AI rates are not effected by the presence of the surface and that there are no other loss rates.

In general, the population $n_i(t)$ of an initial state i with life time τ_i decays exponentially [65]:

$$n_i(t) = g_i e^{-t/\tau_i} \tag{6.1}$$

Where g_i is the initial population of state i. If there are several decay channels to different final states f, each with its own characteristic decay rate Γ_{if}, then the life time of state i is given by

$$\tau_i = \left(\sum_f \Gamma_{if} \right)^{-1} \tag{6.2}$$

The fraction of the population $n_i(t)$ which has decayed in a specific transition $i \rightarrow f$ within a time interval dt is given by

$$p_{if}(t)dt = \Gamma_{if} n_i(t)dt \tag{6.3}$$

Integration with respect to time then gives the fraction of the initial population g_i, which has decayed by AI in time T, *i.e.*

$$I_{if}(T) = g_i \Gamma_{if} \tau_i \left[1 - e^{-T/\tau_i} \right] \tag{6.4}$$

Where $\Gamma_{if}\tau_i$ is the 'branching ratio' for the specific $i \rightarrow f$ transition. The time T is the 'observation time', *i.e.* the time between neutralization and impact on the surface. For infinite observation times the fraction I_{if} is proportional to the branching ratio, *i.e.* $I_{if} \propto \Gamma_{if}\tau_i$. In case of very short observation times ($T \ll \tau_i$) the fraction is proportional to the AI rate and the time, *i.e.* $I_{if} \propto \Gamma_{if} T$.

In figure 6.1 the decayed fractions I_{if} for AI processes of the four $(2l2l')$ states of our interest are plotted as a function of the observation time T. Every state i has only one decay channel so the branching ratio is 1. For easy comparison all states are assumed to be initially equally populated, *i.e.* $g_i = 1$ for all i. For our experiments, typical observation times vary roughly between 10 and 100 fs, as indicated by the grey area in figure 6.1. It is clear that the values of the fractions differ considerably over this time window. While the ^{1}S and ^{1}D fractions change only slightly between 10 and 100 fs, the ^{3}P fraction changes almost by a factor of 5.

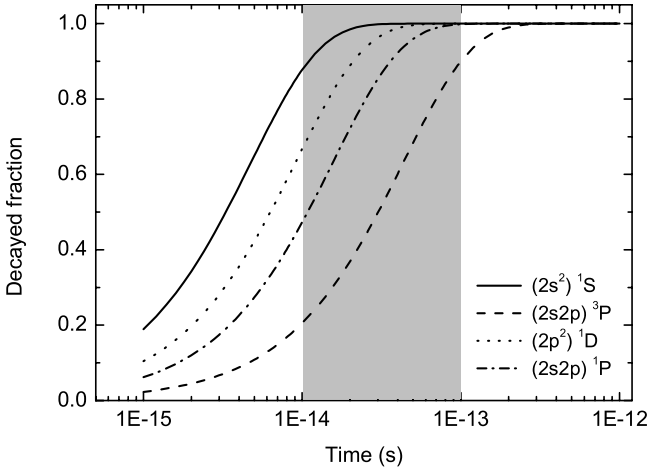

Figure 6.1: Decayed fractions for the four relevant $He^{2*}(2l2l')$ states, plotted versus observation time.

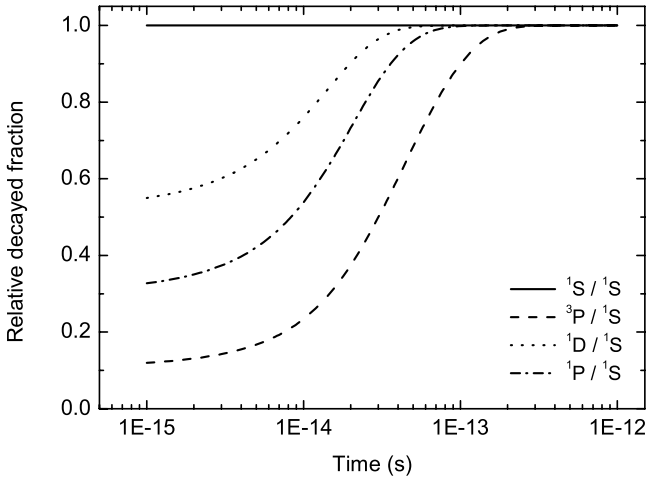

Figure 6.2: Relative decayed fractions, normalized to the ^{1}S state, plotted versus observation time.

It is also illustrative to plot the relative decayed fractions versus time, as shown in figure 6.2. All fractions are normalized to the ^{1}S fraction, since this

state decays fastest. Plotted this way, the relative intensities of the other three fractions as compared to the ^{1}S fraction can be demonstrated even better.

The observation time T (in fs) available for AI above the surface can be estimated by [65]

$$T = \frac{z_0}{v_\perp} \simeq 7.64 \cdot \frac{z_0}{\sqrt{E_\perp}} \tag{6.5}$$

Here, z_0 is the neutralization distance in a.u. and $E_\perp$ is the perpendicular kinetic energy $E_\perp = E_{kin} \sin^2(\psi)$ in eV. The distance z_0 is determined by the COB model (chapter 2) and generally depends on the electronic properties of the target and the projectile as [89]

$$z_0 \simeq \frac{\sqrt{8q\epsilon(7+\epsilon)}}{2\phi(\epsilon+1)} \tag{6.6}$$

Where ϕ and ϵ are the target work function and permittivity, respectively, and q is the projectile charge state. Equation (6.6) ranges from $z_0 \simeq \sqrt{2q}/\phi$ for a perfect conductor ($\epsilon = \infty$) to $z_0 \simeq 2\sqrt{q}/\phi$ for a perfect insulator ($\epsilon = 1$). The image charge energy E_{im} also contributes to $E_\perp$ but is only about 3 eV for a He^{2+} ion above a perfect conductor and even less above a perfect insulator.

Typical observation times T, as obtained from equation (6.5) with $q = 1$, vary roughly between 10 and 100 fs. Unfortunately, these times were found to be too short to explain the experimentally observed changes in Auger spectra for He^{2+} on Si(100) ([65] and section 6.4). Schippers *et al.* [65] tried to overcome this by assuming that decay processes are still observed after projectile penetration into the solid, up to the escape depth for 30-40 eV electrons. For 35 eV electrons in Si this corresponds to a tripling of the observation time. However, this implies that the projectiles penetrate the solid about 12 Å. This is very unlikely for grazing-incidence projectiles with kinetic energies below a few keV, since it is shown that they are reflected from the surface [85, 90].

6.4 Auger spectra: metal versus semiconductor

Our Auger spectra arising from He^{2+} collisions with two metals, Pt(110) and Fe(110), are compared to Auger spectra from a semiconductor, Si(100) [65]. Three values for the perpendicular energy $E_\perp$ were selected: 1, 15 and 35 eV. The raw experimental data is shown in figure 6.3. Column 1 and 2 show the Auger spectra taken from the two metals (Pt and Fe), column 3 shows those from the semiconductor (Si). Already from the raw data shown in figure 6.3, a striking difference between the Auger spectra from the two metals (Pt and Fe) and those from the semiconductor (Si) can be seen. Whereas the Auger spectra for the two metals show only small changes, the Auger spectra from the semiconductor exhibit a strong dependence on $E_\perp$.

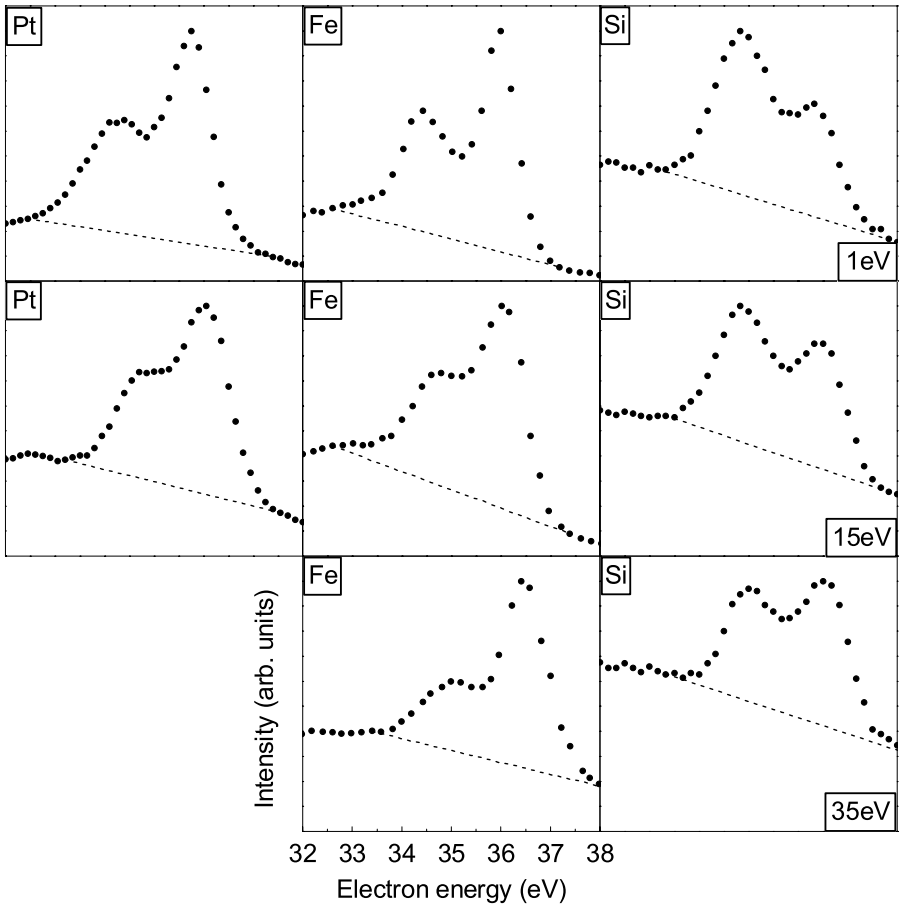

Figure 6.3: Raw helium Auger spectra from Pt(110), Fe(110) and Si(100) plotted for three perpendicular kinetic energies (1, 15 and 35 eV). The estimated background contribution is indicated by the dashed lines.

This is seen even more clearly in figure 6.4, which shows the background subtracted Fe and Si spectra from figure 6.3. For clarity, and because of its strong resemblance with the Fe target, the Pt spectra are left out of this figure. For a detailed analysis of the Auger spectra, the exact shape of the background is of importance. This can clearly be seen in figure 6.3. The raw experimental data show that the double peak structure sits on top of a rather large background. This background mainly stems from Auger neutralization (AN), Auger de-excitation (AD) and (scattered) AI electrons [91, 92]. Unfortunately, the ex-

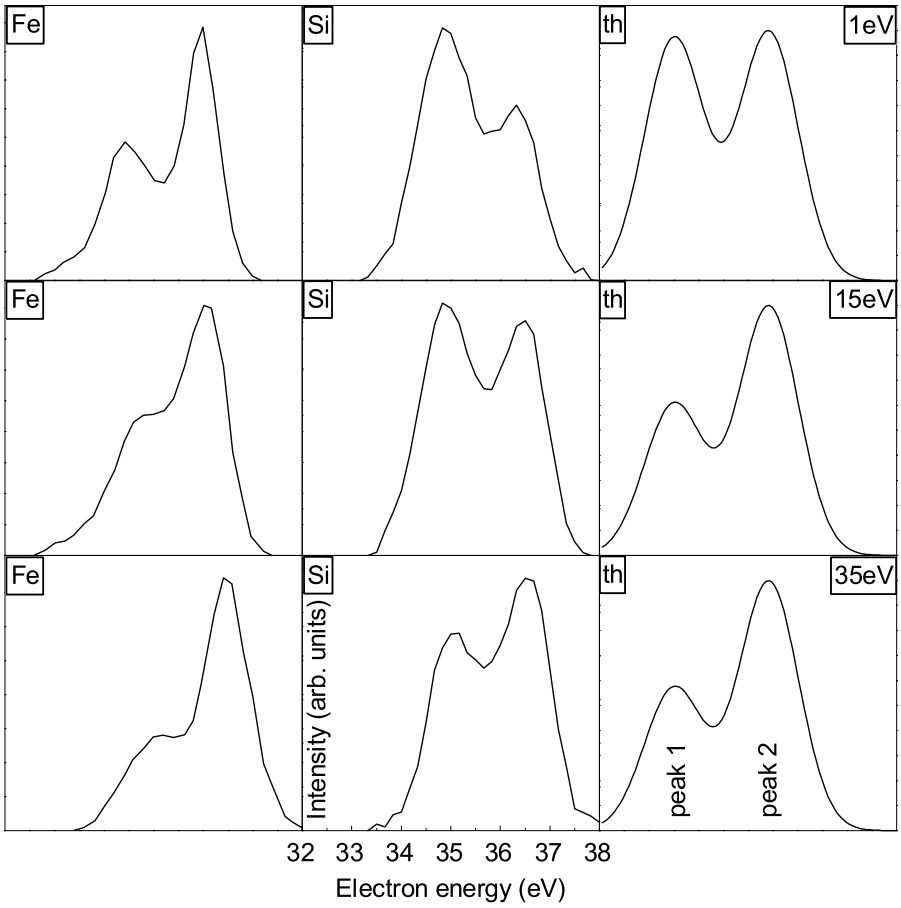

Figure 6.4: Comparison between background subtracted helium Auger spectra from Fe(110) and Si(100) and theoretical results (th) from the free atom model. The subtracted background is shown in fig. 6.3 (dashed lines).

act shape of the background is very difficult to determine. However, the energy window of relevance (32-38 eV) is very small as compared to the range of the background (0-45 eV). Therefore, as a first approximation, a linear background can be applied as is indicated by the dashed lines in figure 6.3.

The third column in figure 6.4 shows the results from the free atom model, which are obtained as follows. From equations (6.5) and (6.6) the vertical kinetic energy $E_\perp$ is transformed into the observation time T. Then, the free

atom model is used to calculate the decayed fractions at this time T. As a first attempt, the initial populations g_i of the four He^{2*} states are assumed to be determined solely by their corresponding statistical weights (see table 6.1). The decayed fractions of the ^1S and ^3P states are added and convoluted with a Gaussian (FWHM=1.2 eV) line profile to form 'peak 1'. Similarly, from the decayed ^1D and ^1P fractions 'peak 2' is constructed. For a perfect conductor ($\epsilon = \infty$) the $E_\perp$ energies of 1, 15 and 35 eV correspond by equation (6.5) to observation times T (for $q = 1$) of 60, 15 and 10 fs, respectively.

The free atom model predicts that for short T (high $E_\perp$) the intensity of peak 2 (^1D+^1P) is higher than the intensity of peak 1 (^1S+^3P). This is mainly due to the low AI rate of the ^3P state, as can be seen from figure 6.1 and 6.2. If the projectile is given more time (lower $E_\perp$), also a considerable fraction of the ^3P state population can decay and the intensity of peak 1 will increase. In figure 6.4 (column 3) the theoretical results (th) of the free atom model clearly show the (relative) increase of peak 1 with decreasing $E_\perp$.

The Auger spectra from the semiconductor (Si), figure 6.4 column 2, seem to follow the behavior predicted by the free atom model. For short observation times (lower panel) the intensity of peak 2 is higher than that of peak 1. For longer times (upper panel) the intensity of peak 1 even exceeds that of peak 2. Apparently, the formation and decay of the He^{2*} states, which is reflected by the peak intensities, seems to change from a peak 2 configuration for short T to a peak 1 configuration for long T. To get a one-to-one correspondence between the Si data and the model, Schippers *et al.* [65] had to triple the observation time. But as stated in section 6.3, there seems no direct justification for this.

The changes in the Auger spectra from the metal (Fe), figure 6.4 column 1, are much smaller than predicted by the free atom model. The intensity of peak 1, as compared to the intensity of peak 2, increases only slightly upon increasing observation time. For the metal it thus seems that, over the investigated range of observation times, the relative dynamic formation and decay of the excited He^{2*} states is nearly constant.

The differences between the Auger spectra from the metal and the semiconductor cannot be explained solely by target work function ϕ and/or permittivity ϵ changes. The targets all have roughly the same work function of about 5 eV [93]. For a perfect insulator the neutralization distance z_0 is a factor $\sqrt{2}$ larger than for a perfect conductor (section 6.3). The image charge acceleration E_{im} above an insulator is also less than for a conductor. Although these effects lead to somewhat longer observation times, the extra time available only has a 5-10% effect on the Auger spectra. From figure 6.4 it is clear that the differences are much larger.

6.4.1 Target electronic structure

In figure 6.5 the electronic structure of a metal (bulk) is depicted. The electrons in the metal are described as a free electron Fermi gas [94]. The maximum kinetic energy of the electrons in the gas, at $T = 0$ K, is the Fermi energy E_F. The Density Of States (DOS) for a 3D gas is proportional to $\sqrt{E}$ [94]. At zero degrees K, up to E_F all states are occupied and states above E_F are empty, as indicated by the grey area in figure 6.5. Temperature induced modifications of the DOS only become of importance at $\sim 10^4$ K and can therefore be neglected.

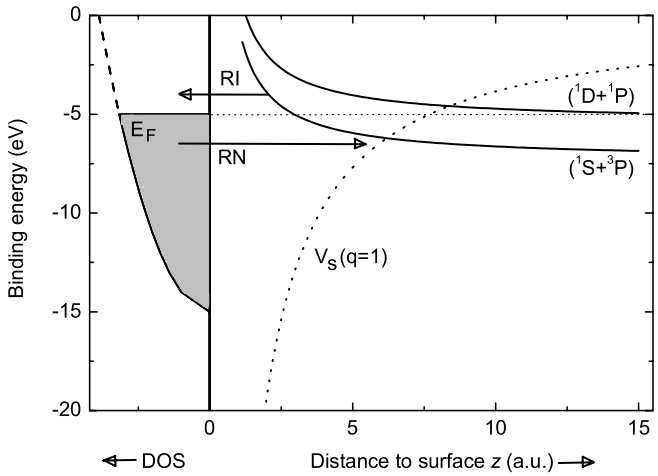

Figure 6.5: Schematic representation of the relevant He^{2*} energy levels (solid), the potential barrier (thick dots) between ion and surface and metal DOS (grey area). The arrows denote the RN and RI processes.

Also indicated in figure 6.5 are the modified projectile states (^{1}S+^{3}P) and (^{1}D+^{1}P), which correspond to peak 1 and peak 2, respectively. Due to the image charge interaction the binding energies E_B of the He^{2*} states are shifted upwards by an amount $\Delta E_B = 1/4z$ (for $q = 0$) [46].

The thick dotted line in figure 6.5 represents the saddle-point potential V_s for $q = 1$, according to the COB model. As soon as V_s drops below the work function ϕ, which is at the level crossing near 7 a.u., resonant transitions between projectile and target can occur. In case of resonant neutralization (RN), a metal electron is transferred over-the-barrier to an empty projectile state. When a projectile state shifts above the Fermi level, resonant ionization (RI) can occur, *i.e.* a projectile electron is transferred to an empty metal state.

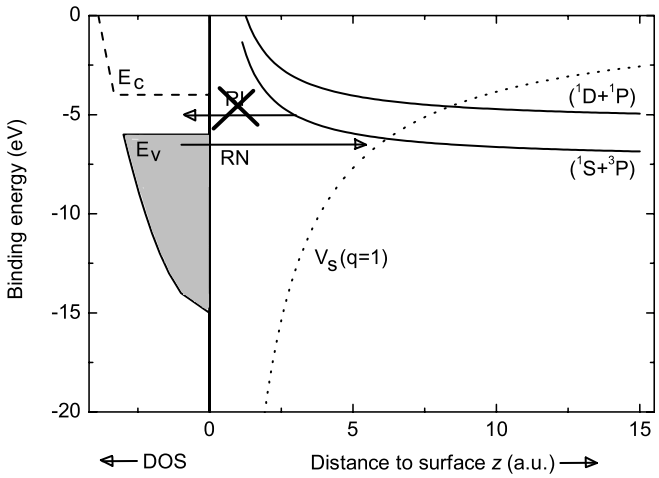

Figure 6.6: Relevant He^{2*} energy levels and semiconductor DOS. Note the change in RI due to the presence of the band gap.

In figure 6.6 an analogous picture is sketched for the semiconductor DOS. In a semiconductor the band gap E_g separates the valence band E_v from the conduction band E_c and the Fermi level is located inside the band gap, for p-type Si *e.g.* slightly above E_v. The difference between the Auger spectra from the metal and the semiconductor may be caused by the presence of the band gap. As can be seen from figures 6.5 and 6.6, after RN the projectile levels shift further upwards as the projectile comes closer to the surface. In the case of the metal, see figure 6.5, at energies above the Fermi level there are empty metal states to which the electrons can be lost (RI). In the semiconductor this decay channel (RI) is blocked by the band gap, as is indicated by the cross in figure 6.6. Therefore the projectile effectively has more time to decay by AI, which may (partly) explain the higher intensity of peak 1 for the semiconductor as compared to the metal.

6.4.2 Resonant ionization

If the projectile levels can be depopulated by AI and RI processes, the RI rate too has to be included in the free atom model. First it is assumed that the RI rate is constant, *i.e.* it does not depend on the ion-surface distance z. Inclusion of the RI rate changes the Auger branching ratio to $\Gamma_{AI}/(\Gamma_{AI}+\Gamma_{RI})$ and the life time τ_i of the state to $1/(\Gamma_{AI}+\Gamma_{RI})$. The initial population of the $He^{2*}(2l2l')$ states is, as a first approximation, given by the statistical weights.

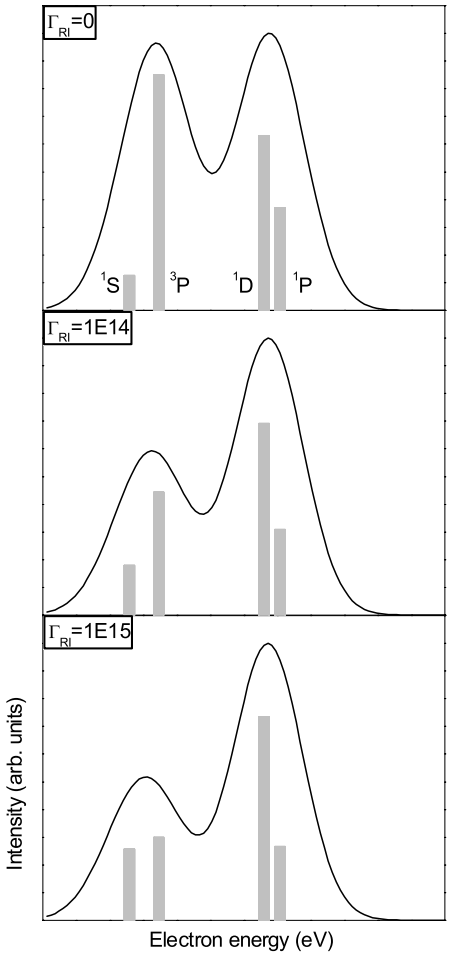

Figure 6.7: Theoretical Auger spectra from the free atom model for a metal target, plotted for three RI rates. The observation time is 60 fs. Also shown are the decayed fractions (grey) of the He^{2*} states.

The effect of variation of the RI rate on the decay of the excited helium states is shown in figure 6.7. The upper panel represents a theoretical Auger spectrum for an observation time of 60 fs, *i.e.* for rather low $E_\perp$, and a RI rate Γ_{RI} of 0. The middle panel in figure 6.7 shows an Auger spectrum for $\Gamma_{RI} = 10^{14}$ Hz and the lower panel has $\Gamma_{RI} = 10^{15}$ Hz. The grey bars in figure 6.7 indicate the decayed fractions of the four relevant states and are labelled in the upper panel. Going from the upper panel to the lower one, *i.e.* for increasing

Γ_{RI}, it can be seen that the extra decay channel (RI) clearly effects the Auger spectra. Although all He^{2*} states are effected by the RI rate, the effect is most pronounced for the ^3P state, which changes by more than a factor 2. Furthermore, states with high AI rates (^1S and ^1D) are effected less by the RI rate, and so they gain in relative intensity. This implies that for projectiles with high perpendicular energies, the Auger spectra will be dominated by AI from states with high AI rates. It also implies that for the slow AI decay of the ^3P state, $E_\perp$ must be rather low in order to have enough time.

The absence or presence of the RI channel may explain the difference between the Auger spectra from the metal (Fe) and the semiconductor (Si). From figure 6.4 (top row) it can be seen that for Fe peak 1 is suppressed as compared to the free atom model result. A similar suppression of peak 1 is seen in figure 6.7, which is due to resonant ionization. From a comparison between theory (fig. 6.7) and experiment (fig. 6.4) it may then be concluded that the RI rate must be of the order of 10^{15} Hz.

The resonant ionization rate Γ_{RI} can also be estimated using classical arguments. In the hydrogenic approximation, the classical orbiting time t_n of an electron in state n is given by

$$t_n = \frac{2\pi n^3}{Z_{eff}^2} \tag{6.7}$$

Where $Z_{eff} = Z - s$ is the effective charge of the helium core and s is the Slater screening constant [95]. For an $n = 2$ electron in $He^{2*}(2l2l')$, we have $s = 0.35$ and $Z_{eff} = 1.65$. Typical RI rates for $n = 2$ electrons, as obtained from equation (6.7), are of the order of 10^{15} Hz. This result is in good agreement with our earlier estimate of the RI rate.

For the observation of spin polarization effects, which were discussed in chapter 5, the ^3P state must be populated and allowed to decay by AI. Therefore the perpendicular energy has to be low enough in order to gain time. The ^3P fraction is also strongly affected by the presence of the RI channel, as was discussed above. The effect of variation of the RI rate can clearly be indicated via the relative decayed fraction $^3P/^1S$, as shown by figure 6.8. The strongest changes again occur in the range of our observation times (10-100 fs). It can be seen that only when the RI rate is not too high the projectile ^3P state has enough time to decay by AI. Otherwise the population of the ^3P state is effectively decreased by the fast RI channel. In the limit of long T, for high RI rates the $^3P/^1S$ ratio becomes equal to $\Gamma_{AI}(^3P)/\Gamma_{AI}(^1S)$, instead of equal to 1.

Now it is of note that the same value for the $^3P/^1S$ ratio is obtained in the limit of extremely short observation times. Ergo, it seems that for high RI rates the available observation time becomes less important and peak ratios become nearly constant, in line with our experiments. This seems to lead to

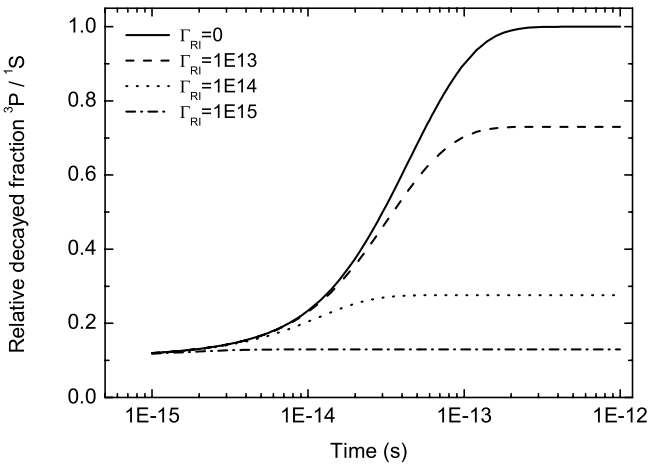

Figure 6.8: Relative decayed fraction ^{3}P/^{1}S plotted as a function of time for four different RI rates.

the important conclusion that peak ratios are directly linked to the initial state population, independent of observation time (projectile velocity).

6.4.3 State population

As a first attempt, it was assumed that the initial populations g_i of the He^{2*} states were given by the statistical weights. The reason for this assumption is based on the resonant exchange of electrons between metal and projectile. If all binding energies of the metal electrons are possible, and if the DOS is constant, then the populations of the projectile states are likely to be statistical. Ideally, the metal DOS varies as $D(E) \simeq \sqrt{E}$ and is therefore approximately constant over a small energy region near E_F, see figure 6.5. Since most electrons stem from a region near the Fermi level, it seems fair to assume a statistical population.

However, as indicated in figure 6.5 (thin dots), over the relevant ion-surface distances the Fermi level lies somewhere between the (^{1}S+^{3}P) and (^{1}D+^{1}P) states. In an early stage of the interaction, around the point (7-8 a.u.) where electrons can transit the barrier, the (^{1}S+^{3}P) states are still well below the barrier. On the other hand, the (^{1}D+^{1}P) states already moved out of resonance before any RN could take place. This scenario might question the validity of assuming an initial state population which is determined by the statistical weights. Furthermore, based on this scenario peak 2 should hardly or not be visible in the Auger spectra.

Because this is not what is experimentally observed, as can be seen in figure 6.3, an additional effect might play a role too. So far, only the perpendicular velocity component $v_\perp$ of the projectile was taken into account. However, as was shown earlier, *e.g.* by Winter *et al.* [96] and Zimny *et al.* [97], also the parallel velocity component $v_\parallel$ has an influence on the neutralization and ionization. In our experiments of He^{2+} on Pt(110), we also observed an influence of $v_\parallel$ on the Auger spectra.

6.4.4 Modified DOS

In the moving-ion frame of reference, the DOS of the metal electrons is different from the DOS in the static laboratory reference frame. This effect is best described from a momentum point of view, or in $\vec{v}$-space. In figure 6.9 the Fermi sphere of the metal electrons is represented by the filled circle with radius v_F. For example, for a Pt(110) surface we have $E_F = 7.50$ eV and $v_F = 0.74$ a.u. [98]. The directions $\hat{v}_\parallel$ and $\hat{v}_\perp$ indicate velocity components parallel and perpendicular to the surface, respectively. The ion velocity is indicated by $\vec{v}_i$. The light-grey ring represents the velocity of a $n = 2$ electron in a $He^{2*}(2l2l')$ state. In the hydrogenic approximation the velocity is given by $v_n = Z_{eff}/n$. For a $n = 2$ helium electron we have $v_2 = 1.65/2 = 0.83$ a.u. and so $v_2 > v_F$.

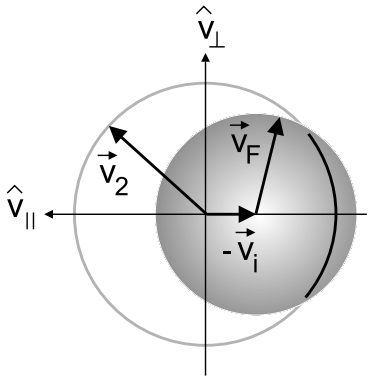

Figure 6.9: Galilean transformation of the metal Fermi sphere into the moving-ion reference frame.

In the ion's frame, the ion is static and the metal electrons are moving with velocity $-\vec{v}_i$. For grazing incidence scattering the Fermi sphere shift due to $v_{i\perp}$ can be neglected, and we have $v_i \approx v_{i\parallel}$. The influence of the ion velocity can be included by a Galilean transformation [99, 100]. In the ion's frame the Fermi velocity is now described by $\vec{v} = \vec{v}_F - \vec{v}_i$. Ergo, the Fermi sphere is shifted by an amount $\vec{v}_i$, as can be seen in figure 6.9. The circle segment (thick

line) indicates the resonance between $\vec{v}_2$ and $\vec{v}$. For $v_i = 0$ a.u. the frames are concentric and no resonance occurs.

The energy $E(\vec{v})$ of the metal electrons is transformed according to

$$E(\vec{v}) = \frac{1}{2}v^2 = E_F - \vec{v}_F \cdot \vec{v}_i + \frac{1}{2}v_i^2 \tag{6.8}$$

As a result of the shift due to (parallel) ion velocity the energy of the Fermi electrons now varies in the range [96] (see fig. 6.10)

$$\frac{1}{2}(v_F - v_i)^2 \leq E_F \leq \frac{1}{2}(v_F + v_i)^2 \tag{6.9}$$

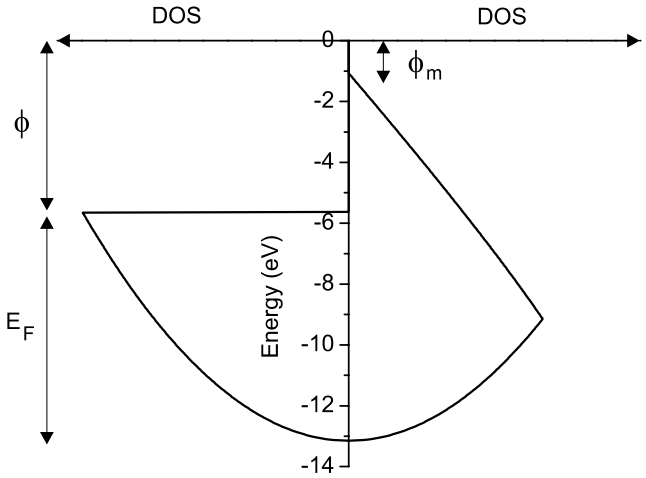

Figure 6.10: Galilean modified DOS for $v_i = 0$ a.u. (left) and $v_i = 0.20$ a.u. (right). Note the work function change ($\phi \rightarrow \phi_m$).

The effect of the parallel velocity component on the shape of the DOS, in the moving-ion frame of reference, is shown in figure 6.10. The normal DOS, *i.e.* when $v_i = 0$ a.u., for the Pt(110) surface ($\phi = 5.65$ eV [101]) is shown on the left side. The right side shows the metal DOS as seen by an ion moving with a velocity $v_i = 0.20$ a.u.. The DOS is already strongly modified although the ion only has about 1/4-th of the Fermi velocity. Also note that the work function ϕ is strongly modified to ϕ_m.

It can be shown that the occupation probability $g(E, v_i)$ of metal states with energy E for ion velocity v_i, in the moving-ion reference frame, is given by [97]

$$\begin{aligned} g(E, v_i) &= 1 && 0 \leq \varepsilon \leq (1-\nu)^2 \\ &= \frac{1}{2} + \frac{1-\nu^2}{4\nu}\varepsilon^{-\frac{1}{2}} - \frac{\varepsilon^{\frac{1}{2}}}{4\nu} && (1-\nu)^2 \leq \varepsilon \leq (1+\nu)^2 \\ &= 0 && \varepsilon \geq (1+\nu)^2 \end{aligned} \tag{6.10}$$

Here, $\nu = v_i/v_F$ and $\varepsilon = E/E_F$ are the relative velocity and energy, respectively. The modified DOS is now given by $g(E, v_i)D(E)$, indicated on the right in figure 6.10.

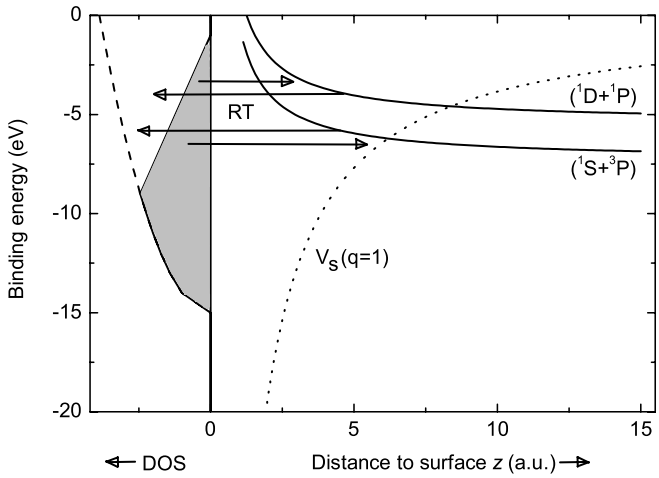

Figure 6.11: Relevant He^{2*} energy levels and modified metal DOS. Note the changes in the RT's, as compared to figure 6.5.

It is clear that a nonzero parallel velocity component of the ion leads to an apparent population of metal electron states with energies above the Fermi level. Therefore electrons can be captured (RN) at larger distances from the surface, thereby extending the time available for AI. In figure 6.11 the He^{2*} levels are depicted together with the modified metal DOS. Note that due to the modified DOS, now all He^{2*} states near the first neutralization distance (~ 7 a.u.) are resonant with occupied metal states. This implies that initially all states can be populated by RN. Furthermore, after the first neutralization step,

RI and RN occur in alternating sequences until the states (finally) decay via autoionization. This multiple electron exchange is likely to lead to a statistical population of the projectile states. These arguments support the assumption of an initial state population for all states which is determined by their statistical weights.

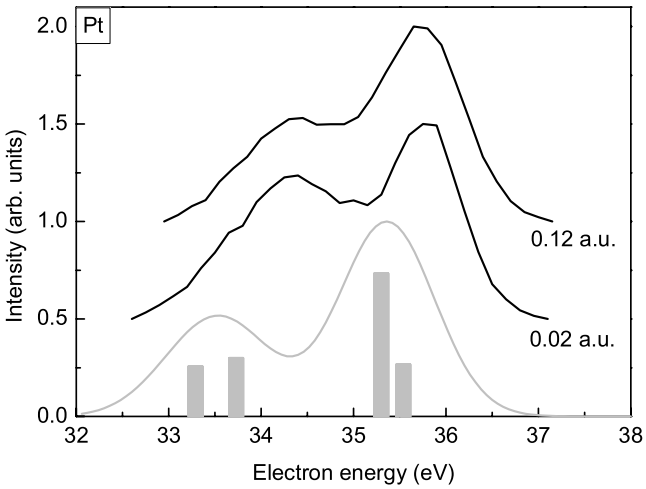

Figure 6.12: Experimental background subtracted helium Auger spectra (black) from Pt(110) for two values of $v_{\|}$. The corresponding theoretical Auger spectrum (grey) is also shown. For clarity the spectra were given a vertical offset.

6.4.5 Parallel velocity

To quantify the effect of the parallel velocity on the spectral features, we measured helium Auger spectra from a Pt(110) surface for $v_{\|}$ ranging from 0.02 to 0.12 a.u. at constant vertical kinetic energy $E_{\perp} \simeq 1$ eV. Figure 6.12 shows the Auger spectra for the two extreme values (black), as well as the theoretical Auger spectra (grey) for $T = 60$ fs and $\Gamma_{RI} = 10^{15}$ Hz. The spectra are normalized on the intensity of peak 2 and plotted with a vertical offset of 0.5 for clarity. Despite the considerable increase in the projectile's parallel velocity, the spectral features hardly changed. The relative intensity of peak 1 is only slightly less for higher $v_{\|}$ (upper spectrum). Apparently even a parallel velocity of only 0.02 a.u., which corresponds to a work function change of about 0.5 eV, is enough to modify the DOS such that all He^{2*} states are populated.

Like for the case of Fe, also for Pt the RI rate of 10^{15} Hz seems to describe the (relative) intensities of the Auger peaks reasonably well. However, due to this high RI rate the effect of longer observation times, due to capture at larger distances from the surface, is washed-out.

From figure 6.12 it can also be seen that the energies of the AI electrons are higher than those of the free atom. This is a manifestation of the image charges: the initial He^{2*} and final He^{+} levels have different shifts, thereby effectively enlarging their energy difference and thus the kinetic energy of the Auger electrons [86]. Also the contact potential between the target and the detector, which can easily be of the order of a few tens of eV, might cause an (additional) energy shift.

6.4.6 Spin ordering

Figure 6.13 shows the density of states for majority ($N_{\downarrow}$) and minority spins ($N_{\uparrow}$) for a Ni target [102]. The difference between the DOS of both spin states is largest near the Fermi level, *i.e.* in the region where RI and RN processes (de-)populate the excited He^{2*} states. Following a statistically determined state population, the formation and decay of the He^{2*} states should be sensitive to the spin density of states. For example, if the DOS for spin-up electrons at the Fermi level is much larger than that of spin-down electrons, the probability for capture of parallel spins (triplet) should also be larger than that for anti-parallel spins (singlet). Therefore changes in the spin density of states are expected to be visible in the Auger spectra.

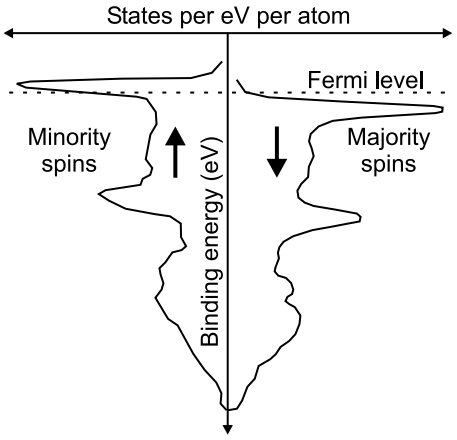

Figure 6.13: Density of states for majority and minority spins for Ni, taken from ref. [102]. Note the difference between the two spin states at the Fermi level.

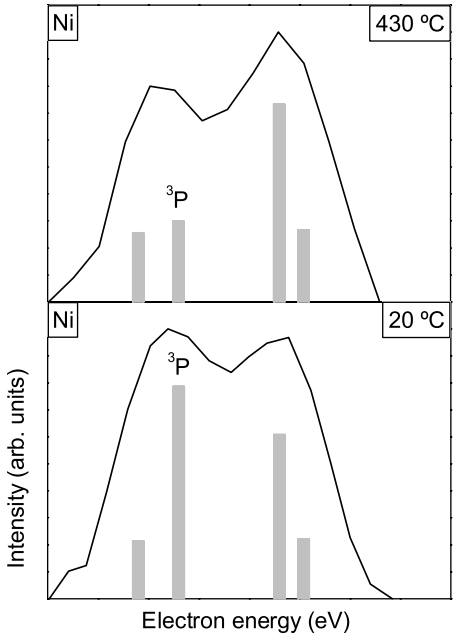

Figure 6.14: Experimental helium Auger spectra for a Ni target below and above the Curie temperature. The theoretical fractions (grey) indicate the corresponding surface spin polarization.

In section 5.3, helium Auger spectra for a Ni(110) target below and above the Curie temperature ($T_C = 354°C$) were presented. At room temperature ($T = 20°C$) the Ni target exhibits ferromagnetic ordering of electron spins. Above the Curie temperature ($T = 430°C$) the ferromagnetic state (spin ordering) is destroyed. Capture of parallel spins into the helium projectiles contributes to the ^{3}P triplet state population, anti-parallel spins are captured into the three singlet states. At room temperature the Auger spectra should reflect the ferromagnetic state and the ^{3}P line is expected to be clearly present. Above T_C the probability for capture into the ^{3}P state is expected to be reduced to its statistical weight. In figure 6.14 the Ni Auger spectra (black) for $20°C$ and $430°C$ from section 5.3 are shown once more. The experimental data indicates a change in the relative intensity of peak 1, induced by temperature, in line with our expectation. The fact that the intensity of peak 1 for $T = 20°C$ is higher than that for $T = 430°C$, indicates the reduced spin ordering at the surface for $T > T_C$.

For Ni, the DOS for minority spins ($N_\uparrow$) at the Fermi level is almost 6.5 times higher than that for the majority spins ($N_\downarrow$), as estimated from figure 6.13. The probability for capture of a spin-up electron, which is given by $P_\uparrow = N_\uparrow/(N_\uparrow + N_\downarrow)$, is 0.86 at the Fermi level. The probability for capture of a spin-down electron $P_\downarrow$ is 0.14. The probability for capture of two spin-up electrons is then given by $P_\uparrow \cdot P_\uparrow = 0.74$, that for two spin-down electrons is 0.02. The probability for the mixed states (up and down) is $P_\uparrow \cdot P_\downarrow = 0.12$. Ergo, the total probability for capture of parallel spins (triplet) is 0.76 and that for anti-parallel spins (singlet) is 0.24.

If the He^{2*} state populations are weighted by their 'spin capture probability', the effect of the spin polarization can be made apparent in the theoretical Auger spectra. This is indicated in figure 6.14, where the decayed fractions (grey) are depicted within the experimental Auger spectra. The theoretical fractions are calculated for $T = 25$ fs and $\Gamma_{RI} = 10^{15}$ Hz. Apparently the calculated fractions describe the (relative) intensity change in peak 1 reasonably well. The difference still existing may be due to the fact that electrons from a certain energy window near the Fermi level contribute.

Conclusions

From the discussion above it can be concluded that inclusion of resonant ionization pushes the simple free atom model into the right direction. The differences between the Auger spectra from the metal and the semiconductor could be explained by an RI rate of about 10^{15} Hz. It was also shown that the parallel velocity of the projectile induces a kinematic shift and justifies an initial state population which is described by the statistical weights. Furthermore, it seems possible to measure and (roughly) estimate spin ordering effects for spin-polarized targets. The description of the dynamics governing the formation and decay of excited helium projectiles above surfaces, as given here, is kept relatively simple. However, despite its simplicity, this approach makes it possible to better than before describe (changes in) the spectral features in helium Auger spectra, arising from the ion-surface interaction.

Chapter 7

Summary and outlook

The work described in this thesis is devoted to the investigation of the possibilities of using ions as probes of the electronic structure of surfaces. One specific topic addressed was whether ion beams can be used to obtain useful information on the electron spin ordering at (polarized) surfaces. The interaction of (highly charged) ions with surfaces is dominated by electron transfer processes. Because electron spin is conserved in the electron capture processes, the polarization of the surface electrons can be transferred to the projectiles. This has has been demonstrated in the chapters 5 and 6 of this thesis. In particular for the case of multiply charged ions, neutralization takes place 'over-the-barrier' into excited projectile states which are (nearly) energetically resonant with states in the target. This leads to the formation of so-called 'hollow atoms', i.e. atoms with populated outer shells and sparsely filled inner shells. These exotic atoms decay efficiently by photon emission or by Auger transitions, which lead to electron emission. Ever since the advent of highly charged ion sources, the formation and decay of the hollow atoms has been studied extensively and by now the main mechanisms are well understood (see e.g. refs. [11] to [14]). On basis of this knowledge it is expected that the interaction of highly charged ions with a magnetic target (spin-polarized) will lead to an enhanced population of higher-spin states, as compared to the case of a non-magnetic target. In Auger Electron Spectroscopy (AES), the electron emission from different spin states can be resolved and thereby it gives access to the spin polarization of the target (chapter 5). Next to this method, Electron Capture Spectroscopy (ECS) with singly charged ions can be used. A fraction of the grazingly incident projectiles is neutralized into an excited state, which subsequently decays under photon emission (fluorescence). After the neutralization, the electron spin is via the spin-orbit coupling (partly) transferred to the orientation of the total angular momentum, and therefore linked to the polarization of the emitted light (chapter 5).

Both methods rely heavily on the knowledge of neutralization processes in ion-surface interactions. Although the electron transfer mechanisms are by and large understood, several aspects of electron transfer between surface and projectile needed further investigation. In particular, the target polarization is carried by the conduction band electrons. Therefore it is important to explore the balance between resonant capture from the conduction band and direct inner-shell capture into projectile states. The latter mechanism can be studied by a variation of the projectiles charge state and/or its velocity (chapter 4).

Therefore, in chapter 4 the interaction of slow ($v < 0.4$ a.u.) hydrogen-like ions with carbon surfaces was studied. AES was used to study the changes in the electron emission induced by the various projectiles. Surprisingly, a strong target K Auger emission was found. These KVV Auger electrons partly originate from carbon atoms at the surface and partly from those of the bulk. A second fraction of the carbon K Auger electrons exhibits distinct spectral features. These peaks can be identified as being due to atomic KLL transitions. Such strong Auger electron emission from the target has not been observed earlier. We presented strong indications that these target KLL Auger electrons originate from hollow carbon atoms sputtered from the surface.

The possibility of using highly charged ions as probes for spin-polarized surfaces is demonstrated in chapter 5. As a first target, a GaAs surface was spin-polarized by optical pumping with polarized laser light. In order to attract the polarized electrons from the bulk to the surface, the surface work function was lowered by adsorption of a small (~ 0.5 ML) amount of cesium atoms onto the surface. Slow He^{2+} ions were scattered off the surface and the projectile KLL Auger emission was used to study the effect of the spin polarization. The changes in the spectral features (peaks) of the Auger spectra were measured as a function of Cs coverage. Maximum change occurred only when σ^+ light was used around a Cs coverage of about 0.5 ML. At this coverage the work function is minimum and the optically pumped and polarized conduction band electrons are expected to be located at the surface. In case the laser was switched off, or in case linearly polarized light was used, no dependence on Cs coverage was found.

As a second target, we used a ferromagnetic nickel surface. This time, the changes in the projectile KLL Auger spectra were studied as a function of target temperature. By increasing the temperature from $T = 20°C$ to $T = 430°C$, *i.e.* through the Curie point of Ni at $354°C$, the relative intensity of the high-spin state decreased. We attributed this change to a loss in the order of the surface electron spins. By destroying the short-range ferromagnetic ordering of the surface, the probability for simultaneous capture of electrons with identical spin orientation decreases and thus the formation of high-spin states is strongly reduced. This is reflected in the Auger spectra, in which decay from low- and high-spin states can be distinguished.

As a third test, spin polarization of surface electrons was induced by an applied magnetic field. Changes in the spin polarization, induced by a switching of the magnetic field, were studied by ECS. We found a good correlation between (changes in) the degree of circular polarization S/I of the fluorescence light and the changes in the magnetic field. Also the sign and magnitude of S/I, as well as the observed asymmetry, are in line with our expectations. From that it can be concluded that these first results are in accordance with the current interpretation.

In chapter 6 a model is introduced which can describe the spectral features in Auger spectra. It is based on a simple 'free atom model' that allows for autoionization (AI rate 10^{14} Hz) of excited projectile states, which are initially populated by their statistic weights. By comparing the model results to experimental data on metallic and semiconductor surfaces, for various scattering conditions, it became clear that the model was incomplete. However, if the excited projectiles are also allowed to decay via resonant ionization (RI rate 10^{15} Hz), the experimental data can be reasonably well described. The difference between the metal and semiconductor Auger spectra were found to be due to the band gap, which blocks the RI process. We also investigated the effects on the projectile velocity component parallel and perpendicular to the surface. Although the parallel component modifies the density of states of the target electrons, almost no effect on the spectral features is observed. This is due to the high RI rate which overwhelms typical AI rates and therefore strongly determines the spectral features. Also effects of 'observation time', determined by the projectiles parallel velocity component, become less pronounced. Furthermore, it seems possible to measure and (roughly) estimate spin ordering effects for spin-polarized targets, as observed via changes in Auger spectra. This was demonstrated by the temperature measurements of the Ni surface, described in chapter 5.

From the results presented in this thesis, it can be concluded that Auger electron spectroscopy and electron capture spectroscopy can be used to probe changes in the spin polarization of surfaces. Since the ion-surface interaction takes place within an area of several tens of nanometers, and lasts only several tens of femtoseconds, the strong electronic interactions take place within a small volume. This enables ions to locally probe the surface electronic structure. Because the interaction area is much smaller than the average magnetic domain size, these methods are also well suited for studies on magnetic surfaces or thin magnetic films.

The description of the complicated interactions, as given in this thesis, is deliberately kept rather simple. However, this more qualitative approach allows a clear and better understanding of the basic phenomena. Of course it is desirable to improve and expand the theoretical and experimental methods. For future experiments with ECS, one can think of using spectral lines of highly

excited projectiles. Then it would be possible to measure at elevated target temperatures with no background from black-body radiation. With the aid of density matrix theory [103], it is possible to calculate the polarization of the light for different scattering geometries and different spectral lines. By comparing these with experimental results, one could *e.g.* study the population of initially excited projectile states. Also the model to describe Auger spectra offers room for improvements. For example, it would be interesting to model distance and time dependent RN and RI rates. Or one could *e.g.* try to implement other (real) densities of states and study their influence on the spectral features of the Auger spectra.

Atomic units

atomic unit	symbol	value	SI unit
length	Bohr radius a_0	$5.29 \cdot 10^{-11}$	m
velocity	αc	$2.19 \cdot 10^{6}$	m/s
time	$a_0/\alpha c$	$2.42 \cdot 10^{-17}$	s
charge	e	$1.60 \cdot 10^{-19}$	C
mass	m_e	$9.11 \cdot 10^{-31}$	kg
energy	$E = m(\alpha c)^2$	$4.36 \cdot 10^{-18}$	J
angular momentum	$\hbar$	$1.05 \cdot 10^{-34}$	Js

Relation between atomic units (a.u.) and SI units. The atomic unit of energy is equal to the potential energy of a $1s$ electron in the hydrogen atom, *i.e.* 1 a.u.=27.2 eV. In atomic physics, equations are written with the conventions $\hbar = 1$, $e = 1$ and $m_e = 1$.

The relation between the ion velocity v_i in a.u. and the non-relativistic kinetic energy E_{kin} in keV of the ion with mass M_i in amu is given by

$$v_i = 0.2\sqrt{\frac{E_{kin}}{M_i}}$$

(1 eV=$1.60 \cdot 10^{-19}$ J and 1 amu=$1.66 \cdot 10^{-27}$ kg)

KLL Auger energies

label	configuration	C^{5+}	N^{6+}	O^{7+}
A	$1s(2s^2\ ^1S)\ ^2S$	248	347	463
B	$1s(2s2p\ ^3P)\ ^2P$	256	358	477
C	$1s(2s2p\ ^1P)\ ^2P$	261	365	484
D	$1s(2p^2\ ^3P)\ ^2P$	262	364	484
E	$1s(2p^2\ ^1D)\ ^2D$	265	369	490
F	$1s(2p^2\ ^1S)\ ^2S$	271	374	498
G	$1s(2s^22p^3)$	274		
	$1s(2s^22p^4)$		384	
	$1s(2s^22p^5)$			510

Calculated kinetic energies (eV) for projectile KLL Auger transitions. The peaks labelled A to F assume a $1s(2l^2)3l^{Z-3}$ initial configuration. The peak labelled G assumes a $1s(2l^{Z-1})$ initial configuration [36].

Experimentally, the KLL Auger electrons would *e.g.* stem from Auger processes occurring after (partial) neutralization of the hydrogen-like ions C^{5+}, N^{6+} and O^{7+} by scattering off a surface. The ions (all with initially 1 K-shell electron) first capture 2 (up to $Z-1$) electrons from the surface valence band into their L-shell. Then, the KLL Auger processes occur and the projectiles emit one of their L-shell electrons into the vacuum.

Bibliography

[1] F.J. Himpsel, J.E. Ortega, G.J. Mankey, R.F. Willis, Adv. in Phys. **47**, 511 (1998).

[2] K. Koike, T. Furukawa, Phys. Rev. Lett. **77**, 3921 (1996).

[3] R. Pfandzelter, G. Steierl, C. Rau, Phys. Rev. Lett. **74**, 3467 (1995).

[4] H.P. Oepen, Y.T. Millev, J. Kirschner, J. Appl. Phys. **81**, 5044 (1997).

[5] S.T. de Zwart, T. Fried, D.O. Boerma, R. Hoekstra, A.G. Drentje, A.L. Boers, Surf. Sci. **177**, L939 (1986).

[6] S.T. de Zwart, A.G. Drentje, A.L. Boers, R. Morgenstern, Surf. Sci. **217**, 298 (1989).

[7] L. Folkerts, R. Morgenstern, Europhys. Lett. **13**, 377 (1990).

[8] J. Das, L. Folkerts, R. Morgenstern, Phys. Rev. A **45**, 4669 (1992).

[9] J. Limburg, J. Das, S. Schippers, R. Hoekstra, R. Morgenstern, Phys. Rev. Lett. **73**, 786 (1994).

[10] J. Limburg, S. Schippers, R. Hoekstra, R. Morgenstern, H. Kurz, F. Aumayr, HP. Winter, Phys. Rev. Lett. **75**, 217 (1995).

[11] H. Winter, J. Phys. Cond. Mat. **8**, 10149 (1996).

[12] HP. Winter, F. Aumayr, J. Phys. B: At. Mol. Opt. Phys. **32**, R39 (1999).

[13] A. Arnau, F. Aumayr, P. Echenique, M. Grether, W. Heiland, J. Limburg, R. Morgenstern, P. Roncin, S. Schippers, R. Schuch, N. Stolterfoht, P. Varga, T.J.M. Zouros, HP. Winter, Surf. Sci. Rep. **27**, 113 (1997).

[14] H. Winter, Phys. Rep. **367**, 387 (2002).

[15] C. Rau, S. Eichner, Phys. Rev. Lett. **47**, 939 (1981).

[16] C. Rau, M. Robert, Phys. Rev. Lett. **58**, 2714 (1987).

[17] J. Leuker, H.W. Ortjohann, R. Zimny, H. Winter, Surf. Sci. **388**, 262 (1997).

[18] M. Schleberger, M. Dirska, J. Manske, A. Närmann, Appl. Phys. Lett. **71**, 3156 (1997).

[19] H. Winter, H. Hagedorn, R. Zimny, H. Nienhaus, J. Kirschner, Phys. Rev. Lett. **62**, 296 (1989).

[20] A. Närmann, M. Schleberger, W. Heiland, C. Huber, J. Kirschner, Surf. Sci. **251/252**, 248 (1991).

[21] H. Winter, Z. Phys. D **23**, 41 (1992).

[22] R. Pfandzelter, T. Bernhard, H. Winter, Phys. Rev. Lett. **86**, 4152 (2001).

[23] J. Kirschner, *Polarized Electrons at Surfaces*, Springer-Verlag, Berlin Germany (1985).

[24] H. Niehus, W. Heiland, E. Taglauer, Surf. Sci. Rep. **17**, 213 (1993).

[25] H.H. Brongersma, R.H. Bergmans, L.G.C. Buijs, J.P. Jacobs, A.C. Kruseman, C.A. Severijns, R.G. van Welzenis, Nucl. Instr. Meth. B. **68**, 207-212 (1992).

[26] B.J.J. Koeleman, S.T. de Zwart, A.L. Boers, B. Poelsema, L.K. Verheij, Phys. Rev. Lett. **56**, 1152 (1986).

[27] S.D. Bader, E.R. Moog, P. Grünberg, J. Magn. Magn. Mat. **53**, L295 (1986).

[28] Th. Rasing, M. Groot Koerkamp, B. Koopmans, H. v.d. Berg, J. Appl. Phys. **79**, 6181 (1996).

[29] G. Schütz, W. Wagner, W. Wilhelm, P. Kienle, R. Zeller, R. Frahm, G. Materlik, Phys. Rev. Lett. **58**, 737 (1987).

[30] G.M. Watson, D. Gibbs, G.H. Lander, B.D. Gaulin, L.E. Berman, Hj. Matzke, W. Ellis, Phys. Rev. Lett. **77**, 751 (1996).

[31] S. Ferrer, P. Fajardo, F. de Bergevin, J. Alvarez, X. Torrelles, H.A. van der Vegt, V.H. Etgens, Phys. Rev. Lett. **77**, 747 (1996).

[32] G. Schönhense, C.M. Schneider, Phys. Blätter **53**, 1213 (1997).

[33] C.M. Schneider, R. Frömter, W. Kuch, J. Kirschner, C.H. Ziehten, W. Swiech, G. Schönhense, Omicron Newsletter 1/98 (1998).

[34] M. Speckmann, H.P. Oepen, H. Ibach, Phys. Rev. Lett. **75**, 2035 (1995).

[35] S.T. de Zwart, PhD thesis, R*u*G (1987).

[36] J. Limburg, PhD thesis, R*u*G (1996).

[37] M.T. Robinson, Phys. Rev. B **40**, 10717 (1989).

[38] M.T. Robinson, Nucl. Instr. Meth. B **48**, 408 (1990).

[39] H.D. Hagstrum, Phys. Rev. **96**, 336 (1954).

[40] H. Ryufuku, K. Sasaki, T. Watanabe, Phys. Rev. A **21**, 745 (1980).

[41] A. Bárány, G. Astner, H. Cederquist, H. Danared, S. Huldt, P. Hvelplund, A. Johnson, H. Knudsen, L. Liljeby and K.G. Rensfelt, Nucl. Instr. Meth. B **9**, 397 (1985).

[42] A. Niehaus, J. Phys. B: At. Mol. Opt. Phys. **19**, 2925 (1986).

[43] J. Burgdörfer, P. Lerner, F.W. Meyer, Phys. Rev. A **44**, 5674 (1991).

[44] C. Lemell, H.P. Winter, F. Aumayr, J. Burgdörfer, F. Meyer, Phys. Rev. A **53**, 880 (1996).

[45] N.D. Lang, W. Kohn, Phys. Rev. B **7**, 3541 (1973).

[46] H. Winter, Comm. At. Mol. Phys. **26**, 287 (1991).

[47] H. Haken, C.H. Wolf, *The Physics of Atoms and Quanta*, 5-th edition, Springer-Verlag, Berlin Germany (1996).

[48] P. Apell, J. Phys. B: At. Mol. Opt. Phys. **21**, 2665 (1988).

[49] R.A. Baragiola, C.A. Dukes, Phys. Rev. Lett. **76**, 2547 (1996).

[50] R. Hentschke, K.J. Snowdon, P. Hertel, W. Heiland, Surf. Sci. **173**, 565 (1986).

[51] A.G. Shenstone, Phys. Rev. **38**, 873 (1931).

[52] R.D. Cowan, *The theory of Atomic Structure and Spectra*, University of California Press, Berkeley USA (1981).

[53] H.A. Bethe and E.E. Salpeter, Quantum mechanics of one and two electron systems, in *Handbuch der Physik Band XXXV*, 88, Springer-Verlag, Berlin Germany (1957).

[54] L. Folkerts, PhD thesis, R*u*G (1992).

[55] F. Bourg, R. Geller, B. Jacquot, Nucl. Instr. Meth. A **254**, 13 (1987).

[56] A.G. Drentje, H.R. Kremers, J. Mulder, J. Sijbring, Rev. Sci. Instr. **69**, 728 (1998).

[57] R. Hoekstra, *The chopper-sweeper system*, KVI (unpublished) (1990).

[58] E.H.A. Granneman, M.J. van der Wiel, *Transport, dispersion and detection of electrons, ions and neutrals*, Chapter IV (1979).

[59] S. Bashkin, J.O. Stoner, *Atomic energy levels and Grotrian diagrams* Vol. 1, North Holland, Amsterdam The Netherlands (1975).

[60] D. Clarke, J.F. Grainger, *Polarized Light and Optical Measurement*, Pergamon Press, Oxford UK (1971).

[61] L.H. Tjeng, R. Hesper, A.C.L Heessels, A. Heeres, H.T. Jonkman, G.A. Sawatzky, Solid State Comm. **103**, 31 (1997).

[62] J. Limburg, S. Schippers, I. Hughes, R. Hoekstra, R. Morgenstern, S. Hustedt, N. Hatke, W. Heiland, Phys. Rev. A **51**, 3873 (1995).

[63] J.E. Houston, J.W. Rogers, R.R. Rye, F.L. Hutson, D.E. Ramaker, Phys. Rev. B **34**, 1215 (1986).

[64] J. Das, R. Morgenstern, Phys. Rev. A **47**, R755 (1993).

[65] S. Schippers, J. Limburg, J. Das, R. Hoekstra, R. Morgenstern, Phys. Rev. A **50**, 540 (1994).

[66] F.W. Meyer, S.H. Overbury, C.C. Havener, P.A. Zeijlmans van Emmichoven, D.M. Zehner, Phys. Rev. Lett. **67**, 723 (1991).

[67] S. Schippers, S. Hustedt, W. Heiland, R. Köhrbrück, J. Bleck-Neuhaus, J. Kemmler, D. Lecler, N. Stolterfoht, Phys. Rev. A **46**, 4003 (1992).

[68] J. Limburg, J. Das, S. Schippers, R. Hoekstra, R. Morgenstern, Surf. Sci. **313**, 355 (1994).

[69] U. Lehnert, M.P. Stöckli, C.L. Cocke, J. Phys. B: At. Mol. Opt. Phys. **31**, 5117 (1998).

[70] I. Schäfer, M. Schlüter, M. Skibowski, Phys. Rev. B **35**, 7663 (1987).

[71] J. Thomaschewski, J. Bleck-Neuhaus, M. Grether, A. Spieler, N. Stolterfoht, Phys. Rev. A **57**, 3665 (1998).

[72] R. Díez Muiño, N. Stolterfoht, A. Arnau, A. Salin, P.M. Echenique, Phys. Rev. Lett. **76**, 4636 (1996).

[73] D.T. Pierce, F. Meier, Phys. Rev. B **13**, 5484 (1976).

[74] D.T. Pierce, R.J. Celotta, G.C. Wang, W.N. Unertl, A. Galejs, C.E. Kuyatt, S.R. Mielczarek , Rev. Sci. Instr. **51**, 478 (1980).

[75] H. Lüth, *Surfaces and interfaces of solid materials*, Springer Verlag, Berlin (1995).

[76] K. Yamada, J. Asanari, M. Naitoh, S. Nishigaki, Surf. Sci. **402**, 683 (1998).

[77] D. Heskett, T. Maeda Wong, A.J. Smith, W.R. Graham, N.J. DiNardo, E.W. Plummer, J. Vac. Sci. Tech. B **7**, 915 (1989).

[78] H.J. Andrä, H. Winter, R. Fröhling, N. Kirchner, H.J. Plöhn, W. Wittmann, W. Graser, C. Varelas, Nucl. Instr. Meth. B **170**, 527 (1980).

[79] N.H. Tolk, B. Willerding, H. Steininger, W. Heiland, K.J. Snowdon, Nucl. Instr. Meth. B **2**, 488 (1984).

[80] A. Närmann, PhD thesis, Universität Osnabrück (1989).

[81] R. Zimny, H. Hagedorn, H. Winter, J. Kirschner, Appl. Phys. A **47**, 77 (1988).

[82] H. Schröder and E. Kupfer, Z. Phys. A **279**, 13 (1967).

[83] R. Hoekstra *et al*, Phys. Rev. A **41**, 4800 (1990).

[84] R. Hoekstra, J. Manske, M. Dirska, G. Lubinski, M. Schleberger, A. Närmann, Nucl. Instr. Meth. B **125**, 53 (1997).

[85] P.A. Zeijlmans van Emmichoven, P.A.A.F. Wouters, A. Niehaus, Surf. Sci. **195**, 115 (1988).

[86] H.D. Hagstrum, G.E. Becker, Phys. Rev. B **8**, 107 (1973).

[87] H. Brenten, H. Müller, V. Kempter, Phys. Rev. Lett. **70**, 25 (1993).

[88] P.J. Hicks, J. Comer, J. Phys. B: At. Mol. Opt. Phys. **8**, 1866 (1975).

[89] A. Bárány, C.J. Setterlind, Nucl. Instr. Meth. B **98**, 184 (1995).

[90] A. Robin, N. Hatke, A. Närmann, M. Grether, D. Plachke, J. Jensen, W. Heiland, Nucl. Instr. Meth. B **164-165**, 566 (2000).

[91] D.A. Shirley, Phys. Rev. B **5**, 4709 (1972).

[92] S. Tougaard, P. Sigmund, Phys. Rev. B **25**, 4452 (1982).

[93] H.B. Michaelson, J. Appl. Phys. **48**, 4729 (1977).

[94] C. Kittel, *Introduction to Solid State Physics*, 7-th edition, Wiley, New York USA (1996).

[95] J.C. Slater, Phys. Rev. **36**, 57 (1930).

[96] H. Winter, Nucl. Instr. Meth. B **78**, 38 (1993).

[97] R. Zimny, Z.L. Mišković, Nucl. Instr. Meth. B **58**, 387 (1991).

[98] S.O. Kasap, *Principles of electronic materials and devices*, 2-nd edition, McGraw-Hill, USA (2002).

[99] J.N.M. van Wunnik, J.J.C. Geerlings, J. Los, Surf. Sci. **131** 1 (1983).

[100] J. Los, J.J.C. Geerlings, Phys. Rep. **190**, 133 (1990).

[101] D.E. Eastman, Phys. Rev. B **2**, 1 (1970).

[102] L. Hodges, H. Ehrenreich, N.D. Lang, Phys. Rev. **152**, 505 (1966).

[103] K. Blum, *Density Matrix Theory and Applications*, 2-nd edition, Plenum Press, New York USA (1996).

Nederlandse samenvatting

Wanneer ionen aan een vastestofoppervlak worden verstrooid, is de kans groot dat ze geneutraliseerd worden door één of meerdere elektronen van het oppervlak in te vangen. Deze ingevangen elektronen komen in eerste instantie meestal niet in de grondtoestand van het projectiel terecht, maar in een aangeslagen toestand. Omdat deze elektronen zich relatief ver van de kern bevinden wordt een dergelijk projectiel ook wel een 'hol atoom' genoemd. Vervolgens vinden vervalprocessen plaats waarbij fotonen of elektronen geëmitteerd kunnen worden. Het blijkt dat de details van deze emissieprocessen voor een groot gedeelte bepaald worden door de elektronische structuur van het oppervlak waaruit de elektronen komen. Dit betekent dat een analyse van de emissieprocessen de mogelijkheid biedt om informatie over de elektronische oppervlaktestructuur te verkrijgen. In tegenstelling tot andere methoden voor de bestudering van oppervlaktestructuren, is het hierbij mogelijk om exclusief informatie te verkrijgen over de buitenste, enkele laag van atomen. Door een juiste keuze van de verstrooiingsgeometrie kan namelijk het indringen van ionen in diepere lagen van het oppervlak worden voorkomen. Om informatie over de elektronische structuur van een oppervlak te kunnen extraheren uit de metingen van fotonen en elektronen, moet de wisselwerking tussen ion en oppervlak goed begrepen zijn. In dit proefschrift wordt deze wisselwerking onderzocht door de emissiepatronen van fotonen en elektronen, onstaan door de interactie van ionen met o.a. spin-gepolariseerde oppervlakken, te meten. Vanuit atoomfysische experimenten is namelijk bekend dat de elektronenspin behouden blijft tijdens elektronenoverdracht. De verwachting is dus dat de spinpolarisatie van de elektronen in het oppervlak wordt overgedragen op het projectiel.

Om aan te tonen dat ionenbundels gebruikt kunnen worden om bijvoorbeeld veranderingen in de elektronische oppervlaktestructuur te meten zijn twee spectroscopische methoden toegepast. Elektronenvangstspectroscopie (ECS) maakt gebruik van het feit dat de elektronenspin, na neutralisatie van het ion, via de spin-baaninteractie overgedragen wordt op het baanimpulsmoment van het projectiel. Veranderingen van het baanimpulsmoment leiden vervolgens weer tot veranderingen van de polarisatie van het uitgezonden licht. In

Auger-elektronenspectroscopie (AES) wordt gebruik gemaakt van het feit dat de geëmitteerde Auger-elektronen, afkomstig van verschillende spintoestanden van het projectiel, energetisch te onderscheiden zijn. Informatie over de spinpolarisatie kan dus worden verkregen uit de energieverdeling van de uitgezonden elektronen.

Tijdens de ion-oppervlakinteractie, welke wordt gedomineerd door elektronenoverdracht, wisselen neutralisatie- en ionisatieprocessen elkaar voortdurend af. Bij resonante elektronenoverdracht worden de elektronen overgedragen tussen energetisch vergelijkbare toestanden in het oppervlak en het projectiel. Volgens het succesvolle klassieke 'over-de-barrière'-model, gebeurt dit zodra de potentiaalbarrière tussen ion en oppervlak lager wordt dan het Fermiveau van het oppervlak (hoofdstuk 2). Deze resonante processen verlopen minstens zo snel als Auger-transities (hoofdstuk 6). Een andere mogelijkheid is dat elektronenoverdracht plaatsvindt tussen sterker gebonden toestanden in het oppervlak en het projectiel (hoofdstuk 4). Aangezien de spinpolarisatie wordt gedragen door de geleidingselektronen, is het van belang om te weten of deze twee vormen van elektronenoverdracht onderscheiden kunnen worden. Afhankelijk van de snelheid en inschiethoek van het projectiel, en de elektronische structuur van het projectiel en het oppervlak blijkt dit inderdaad mogelijk (hoofdstukken 4, 5 en 6).

In hoofdstuk 4 worden experimenten besproken waarbij langzame hooggeladen ionen verstrooid worden aan een koolstofoppervlak. Door de elektronische structuur van het projectiel te veranderen kon de interactie tussen sterkgebonden toestanden in projectiel en oppervlak worden bestudeerd. Het opvallendste resultaat was dat er naast de sterke elektronenemissie vanuit het koolstof, ook sterke indicaties zijn gevonden voor het wegbotsen van holle koolstofatomen van het oppervlak.

In hoofdstuk 5 worden spin-gepolariseerde oppervlakken onderzocht, waarbij juist de resonante elektronenoverdracht van belang is. Hierbij werden beide spectroscopische methoden (AES en ECS) toegepast. Allereerst werd een GaAs-oppervlak bestudeerd. Het oppervlak werd gepolariseerd door een laagje cesium op te dampen en te bestralen met gepolariseerd laserlicht. De verhouding van de intensiteiten van spectraallijnen in de Auger-spectra werd gemeten als functie van de Cs-bedekking. De verandering was maximaal wanneer circulair gepolariseerd licht werd gebruikt en het oppervlak bedekt was met ~ 0.5 monolaag cesium. Bij deze bedekkingsgraad is de werkfunctie minimaal en bevinden de optisch gepompte en gepolariseerde elektronen zich aan het oppervlak.

Daarna werd een ferromagnetisch Ni-oppervlak onderzocht. De verandering in de Auger-spectra werd dit keer gemeten als functie van de temperatuur van het oppervlak. Door de temperatuur te verhogen van 20 °C tot 430 °C, d.w.z. tot voorbij het Curie-punt van Ni bij 354 °C, verlaagde de intensiteit van hoge-

spintoestanden. Deze verandering kan worden toegekend aan een vermindering van de ordening van de elektronenspins in het oppervlak.

Tenslotte werd een Ni-oppervlak spin-gepolariseerd door magnetisatie van het oppervlak. Veranderingen in de spinpolarisatie, geïnduceerd door het schakelen van het magneetveld, werden onderzocht met behulp van ECS. Ook hiermee werd een goede correlatie tussen de graad van circulaire polarisatie van de fluorescentie en de magnetisatie van het oppervlak gevonden.

In hoofdstuk 6 wordt een model geïntroduceerd waarmee de spectrale eigenschappen van Auger-spectra kunnen worden beschreven. Het is gebaseerd op een simpel 'vrij-atoommodel' dat autoionisatie (10^{14} Hz) van aangeslagen projectieltoestanden toestaat die worden bevolkt naar gelang hun statistische gewicht. Voor een correcte beschrijving van de experimentele data blijkt het echter essentieel dat de aangeslagen projectielen ook kunnen vervallen via resonante ionisatie (10^{15} Hz). Hiermee kan ook het verschil tussen de Auger-spectra van een metaal- en een halfgeleideroppervlak worden verklaard. Verder blijken invloeden van de horizontale en verticale componenten van de projectielsnelheid t.o.v. het oppervlak slechts een geringe invloed te hebben op de spectrale eigenschappen. Deze worden vooral bepaald door de snelle resonante ionisatieprocessen. Daarnaast was het mogelijk om de gemeten effecten te correleren aan de spinpolarisatie van het oppervlak. Dit werd gedemonstreerd aan de hand van de temperatuurafhankelijke metingen aan Ni.

Deze resultaten samenvattend, kan worden gesteld dat aangetoond is dat (hooggeladen) ionen kunnen worden gebruikt voor de bestudering van elektronische oppervlaktestructuren, zoals bijvoorbeeld spin-gepolariseerde oppervlakken. Hierdoor is de weg vrijgemaakt voor onderzoek naar magnetische oppervlaktestructuren.

Dankwoord

Mijn promotieonderzoek begon in 1999 bij de vakgroep Atoomfysica op het KVI, nadat ik daar net gedurende een jaar mijn afstudeeronderzoek had gedaan. Er werd goed en interessant onderzoek verricht en ik vond zelf dat ik het erg getroffen had met die groep vol leuke, vlotte en goede wetenschappers. Alle fysische experimenten werden gedaan in één experimenteerruimte (bronzaal). Zo ontstond een collegiale sfeer en iedereen in het lab was makkelijk aanspreekbaar en behulpzaam. Ik was dan ook zeer verheugd toen ik hoorde dat ik daar mijn promotieonderzoek mocht doen. Nu is het proefschrift klaar en ik kan terugkijken op een hele mooie tijd.

Daarom wil ik in de eerste plaats mijn (eerste) promotor Reinhard Morgenstern bedanken voor het bieden van deze mogelijkheid. Ik ben hem erg dankbaar voor zijn bijdragen aan mijn promotieonderzoek. Zijn 'open deur'-beleid en bereidheid om me te helpen heb ik altijd erg op prijs gesteld. Ik heb veel kunnen leren van zijn (atoomfysische) kennis en inzicht en kijk terug op een hele fijne samenwerking.

In zeker niet mindere mate, wil ik mijn (tweede) promotor Ronnie Hoekstra bedanken. Hij heeft me altijd uitstekend geholpen, begeleid en gemotiveerd. Ik vond het erg prettig en leerzaam om met hem samen te werken en problemen (uitdagingen), die er altijd zijn, aan te pakken. Menig keer heeft hij met zijn scherp natuurkundig inzicht een belangrijke bijdrage geleverd. Daarnaast was hij ook een geschikte reisgenoot en een goede en gezellige gesprekspartner.

Vervolgens wil ik ook Thomas Schlathölter heel erg bedanken voor zijn bijdragen aan mijn promotie. Ik heb hem o.a. vaak bewonderd om zijn snelle en efficiënte manier van werken. Verder konden we het buiten werktijd ook prima met elkaar vinden.

Daarna wil ik mijn twee paranimfen (en collega's) Steven Hoekstra en Mirko Unipan bedanken. Steven ken ik al sinds het begin van mijn natuurkunde studie en is altijd een goede vriend geweest. Mirko is de promovendus die het onderzoek aan oppervlaktestructuren aan het voortzetten is. Ideale paranimfen dus, en ik ben blij dat ze mij bijstaan tijdens de verdediging van mijn proefschrift. Uiteraard wens ik hen ook veel succes met hun eigen promoties.

En natuurlijk gaat mijn dank ook uit naar de andere Atoomfysica leden: Abel Robin, Steven Knoop, Dennis Bodewits, Zoltán Juhász, Jur de Vries, Stefania Marini, Fresia Alvarado Chacon, Guido Lubinski, Jan Willem Turkstra, Omar Hadjar, Rimco Geels, Albert Mollema, Carolijn van Ditzhuijzen en Annemieke Hendrickx.

Ook wil ik graag de beoordelingscommissie, bestaande uit Werner Heiland, Rob Timmermans en Bert Niesen, bedanken voor het lezen en beoordelen van mijn proefschrift.

Verder wil ik graag de mensen van de technische diensten op het KVI bedanken die door hun goede werk een belangrijke bijdrage geleverd hebben aan de experimenten beschreven in dit proefschrift.

Ook zou ik graag de volgende personen willen bedanken voor de goede en prettige contacten: Marc de Huu, Marcel Volkerts, Elsa van Garderen, Hans Wilschut, Hans Beijers, Jan Mulder, Ivo Formanoy, Jans Sijbring, Henk Gorter, Jan Sa, Tjalling Nijboer, Niek van Wiefferen, Amarins Petitiaux en Andi Närmann.

Hoewel pas vermeld aan het einde, wil ik niet in de laatste plaats mijn ouders, familie en goede vrienden bedanken voor hun hulp, steun, begrip en vriendschap.